UNIVERSITÀ DEGLI STUDI DI MILANO
FACOLTÀ DI SCIENZE MATEMATICHE,
FISICHE E NATURALI
Doctorate School of
Chemical Sciences and Technologies

Department of Physical Chemistry and Electrochemistry

Doctorate Course
in Chemical Sciences, XXIII Cycle

Nitrogen doped carbon catalysts for electrochemical oxygen reduction reaction

Chim/02

Ivano Galbiati
Matr. R07811

Tutor:
Prof. Leonardo Formaro

Coordinator:
Prof. Silvia Ardizzone

A.A.
(2009/2010)

Index

Introduction

Chapter 1: Platinum catalysts

Chapter 2: Platinum-free catalysts

Introduction

Background energy conditions

The energy issues occupy a prominent position in the economy and development at a world level. Reliable and affordable energy is central to world economy and national security. Energy helps drive global economy and has a significant impact on the quality of life and health of people. The rapid economic growth, especially in developing countries, is expected to increase world energy consumption of about 50% by 2025. For that, governments and research are focussed on diversifying energy supply, improving energy efficiency and modernizing the energy infrastructure.

Key results for the future have been pointed out by the major governments, European Union and United States of America, through the competent authority, that are the Directorate General for Energy and Transportation and the Department of Energy. Documents of these agencies were adopted as main source of data in this Introduction given that have been considered the most reliable information sources, also considering the wide range of sometimes contradictory data and elaborations found in literature.

According to the Directorate General for Energy and Transportation: “Europe has agreed a forward-looking political agenda to achieve its energy objectives of sustainability, competitiveness and security of supply, by reducing greenhouse gas emissions by 20%, increasing the share of renewables in the energy consumption to 20% and improving energy efficiency by 20%, all of it by 2020. This agenda means very substantial change in Europe's energy system over the coming years, with public authorities, energy regulators, infrastructure operators, the energy industry and citizens all actively involved. It means choices and investments during a time of much change in global energy markets and international relations. Europe's political leaders need to give clear messages on the energy strategy”.

By the U.S. Department of Energy [1], key recommendations are similar: moderate growth in energy consumption, increased use of renewable, declining reliance on imported liquid fuels, strong growth in shale gas production and projected slow growth in energy-related carbon dioxide emissions in the absence of new policies designed to mitigate greenhouse gas emissions.

Also: ”There are some topics that may affect the energy market in the next future, first of all the continuing updating and renewal of State laws and regulations, end-use energy efficiency -that is, a more efficient use of final energy in industries, services, agriculture, households, transportation and other areas-, the use of shale gas and the retiring (being put out of service, *nda*) or the building of nuclear power plants”. Also other economical considerations related to the state of uncertainty due to the international economical crisis, or the relation between natural gas and oil price in the markets and the world oil price and production trends influence the energy market determining the industrial investments.

At present the majority of the energy comes from fossil fuels, that are not renewable, will eventually end and the largest reserve are in not politically stable areas. For the future it is expected that the annual production of fossil fuels will reach a peak followed by a decrease. DOE "*Annual Energy Outlook*", [9], reports that for the U.S. the production curve is already in the decreasing zone while the world production is increasing. According to British Petroleum the decrease is not yet observed because technological developments allow new deposits to be discovered and greater depths, under the sea and oil of lower quality to be used. Depending on the projection, the world production peak will manifest in 2010 or 2020.

In addition to economical issues there are the environmental issues related to the use of fossil fuels [2]. Globally the direct combustion of fuels for transportation and heating accounts for over half of the greenhouse gas emissions, a significant fraction of the air pollutants and two third of primary fossil energy use.

Even if a continuous progress in reducing emission and increasing energy efficiency is achieved the models project that energy use and emissions of greenhouse gases and pollutants will grow in the next centuries, due to the growing demand, especially in developing countries. For the reasons illustrated above it is clear that a solution to the energy problem must be found. It is more realistic that every country will found the best solution to solve the energy problem inside the national borders, but it is also clear that a worldwide agreement on energy and related greenhouse gas emissions must be found.

According to the *Annual Energy Review* 2008, published in June 2009 [3], the four major economic sectors, industrial, transportation, commercial and residential, recorded a tremendous and continuous growth in the energy consumption, Fig. 1.

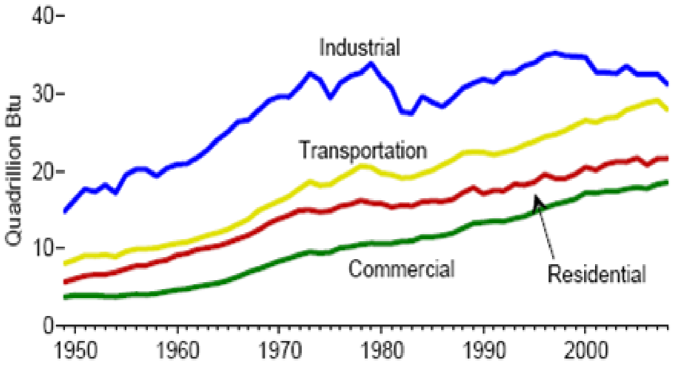

Fig. 1. Total energy consumption by end-use sector for U.S.A. [3].

The industrial sector consumes the highest amount of energy and shows the greatest volatility. In more detail, steep drops occurred in the years where oil price was higher or economic slowdown happened.

As reported in Fig. 2 every economic sector uses fossil energy sources like petroleum, natural gas, coal and biomass, in different way.

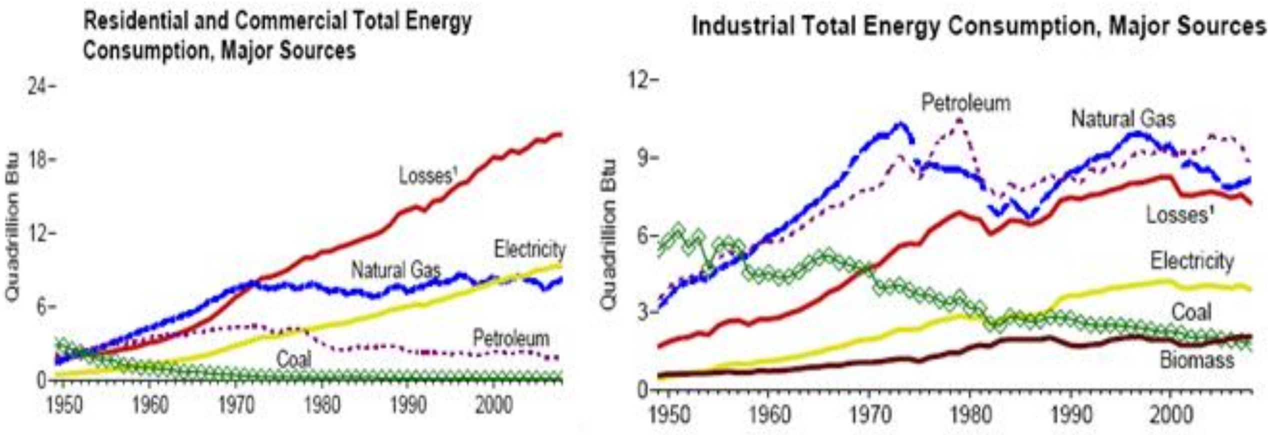

Fig. 2. Use of fossil energy sources for Residential, Commercial and Industrial economic sectors [3].
[1: losses=Energy lost during generation, transmission, and distribution of electricity]

Coal was the major energy sources in the 1950s and 1960s for all the economic sectors, then it was replaced by other forms of energy in residential and commercial consumer and by natural gas and petroleum in the industrial sector. Starting from early 1970s electricity use and related energy losses raised dramatically in all the energetic sectors while the natural gas and petroleum consumption, with mild fluctuations, held fairly steady constant in the following years.

As reported in Fig. 3, energy consumption in the transportation sector is completely different from the other sectors described above: in this sector the use of petroleum as energy source, is dominant.

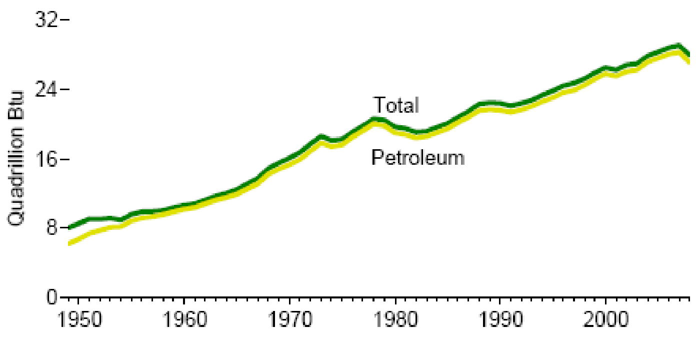

Fig. 3. Total energy consumption for the Transportation sector [3].

The use of energy for transportation tremendously grew overall but registered noticeable pauses in the years 1974, 1979-1982, 1990 and 1991, 2001 and 2008 related to economical or international economical crisis. In 2008, petroleum accounts for 94% of total energy use of transportation sector. Expressed in BTU (1 BTU≡1055.056 J) motor gasoline accounted for 62% of all petroleum used in this sector. Expressed in barrels motor gasoline accounted for 64%.

To related the petroleum use in transportation with other sectors, Fig. 4, reports in more detail the petroleum consumption for the different energetic sectors.

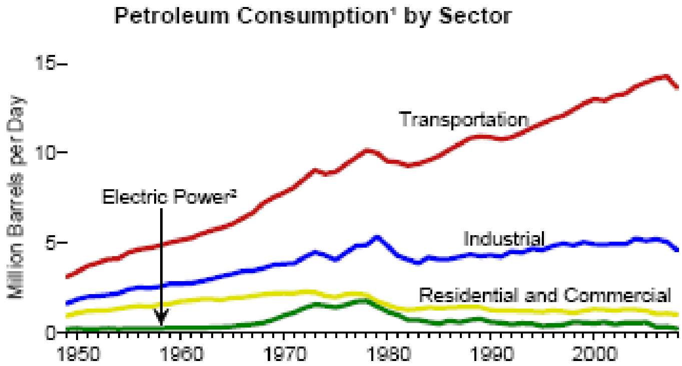

Fig. 4. Consumption of petroleum by sector for U.S.A [3].
1)=Petroleum products supplied is used as an approximation for consumption.
2)= Through 1988, electric utilities only; after 1988, also includes independent power producers].

Transportation is the largest consuming sector of petroleum and the one showing the greatest expansion. In 2008, about 70% of all petroleum used per day was consumed for transportation purposes. Motor gasoline is the single largest petroleum product consumed in the United States. Its consumption was the 46% of petroleum consumption per day in 2008. Other important products are distillate fuel oil, liquefied petroleum gases (GPL) and jet fuel.

The trend of energy consumption for the European Union [4] is similar to the U.S. trend for all the energetic sectors and it is summarized in Fig. 5.

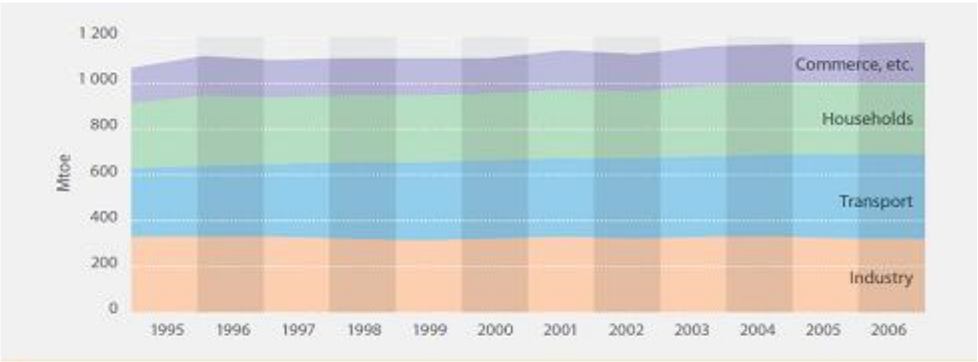

Fig. 5. Total energy consumption by end-use sector for 27 members European Union [4].

It is clear that the transport sector is the biggest final energy consumer: “The amount of final energy used by the transport sector exceeds the amount used by all other industrial sectors taken together. In 2006 transport consumed almost one third of final energy, while the other industries and households respectively accounted for 28 % and 26 %”, [6].

This trend in transport is for European Union associated with two factors: the accession of new EU Member States (Bulgaria, Czech Republic, Hungary, Poland and Baltic countries) with competitive advantages in the road haulage sector and the subsequent expansion of road transport. In addition, some other Member States (Ireland, United Kingdom, Denmark, Greece and Spain) also experienced an increase in their transport sector, resulting in higher energy consumption.

Energy consumption of the commerce and other services remained broadly unchanged. Although the services sector in both added value and employment grew at strongest rate, consumption was kept stable through improved energy efficiency.

Energy consumption in the industry sector, excluding feedstock and petrochemicals, remain fairly stable also because the industry restructuring in Central and Eastern Europe during the 1990s, prevented a rise in energy consumption. The modernizing of these industry also led to a change in the energy mix with a switch from carbon to gas and electricity.

Energy consumption in the household sector increased marginally in the last decade. Two opposite aspects contributed to this trend, a rising number of households and improved living conditions raised up energy consumption but the new appliances usually consume less energy than older and new dwellings are better insulated so the consumes were slowed down.

Overall, energy intensity in the EU economy improved substantially. Progress was mainly achieved through falling energy intensity in the industrial sector, while transport and services contributed to a lesser extent.

Different fuels are used in different way, as reported in Fig. 6.

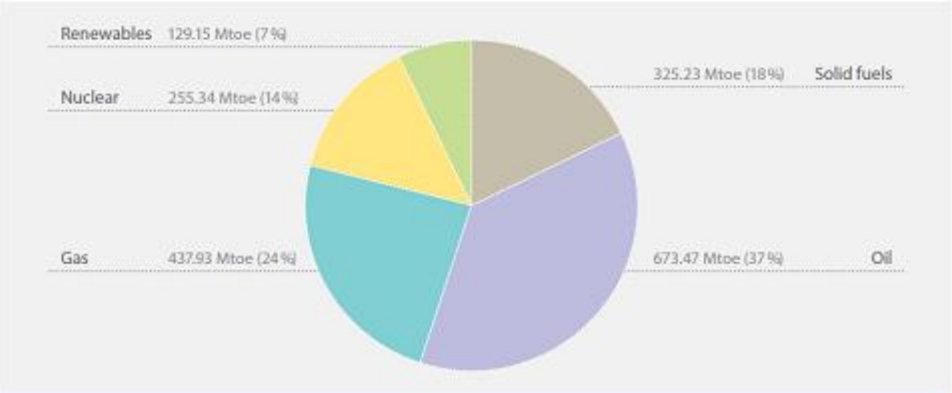

Fig. 6. Use of energy sources in 27 members European Union [4].

Oil is the most intensively used product in the EU's fuel mix and its usage is decreased by 1% from 1990s. During the same period the gas share increased of 6% and the nuclear of 2%. The share of solid fuels shrank considerably of 10% in the same period.

The current fuel mix varies widely in the Member States and it depends on national resources and production pattern. For example the share of nuclear is considerable in the countries that have opted for this energy source like France (42%) or Sweden (35%), oil is widely used in Denmark because indigenous production is dominated by oil.

Renewables

As mentioned at the beginning of this Introduction two of the key topics for the future to diminish the dependence on fossil fuels are moderate energy consumption growth and greater use of renewable. This is due to the fact that U.S. primary energy consumption will increase of 14% from 2008 to 2035. The European primary energy consumption in 2030 will increase of 11% with respect to 2005. The energy growth is not constant but it depend on the economic growth and the population increase.

To overcome the issues related to fossil fuels use it is necessary to shift to renewable sources for energy production. Till now the growth in consumption in renewable fuels is the result of Federal and State program and the rising of fossil fuels prices. As reported, the role of renewable grew in the last years and their role could grow further if current policies that support fuels are extended.

For that reason renewable generation systems must be scaled up to satisfy the increasing world demand of energy. The so called renewable energy sources are: hydropower, biomass, wind, geothermal, solar and ocean power (that is actually marginal to the global scale). Nuclear is not a renewable source of energy but can be considered as carbon-free source of energy that is actually available to satisfy a considerable amount of the energy demand and the cost of fuel is the minimum part of the cost of energy [5].

Every one of the renewable resources has advantages and disadvantages that are briefly reported.

Hydropower is actually the most utilized renewable energy source. Dams in the world currently supply about one/fifth of the electricity consumed worldwide. The reason is that it is a widespread resource and in some countries it is the largest used energy source like in developing countries. One disadvantage is that big rivers are mainly found in industrialized countries like United States, Canada, Brazil, Russia and China so the use of hydropower will not extensively grow up and all the rivers with high flow capacity have been used. One advantage is that cost of electricity generated with hydropower is competitive with coal and gas. Another advantage is that the fuel used is water that is naturally transported to the power generation so no cost is involved in the fuel transport and that dams are instantaneously adaptable to the energy demand that is important to avoid grid collapse.

Dams can also be used as energy reservoir, pumping water in the dams when there is an extra energy production and using this reservoir when it is necessary or for other purposes, like irrigation.

Disadvantages are that dams have effects on the ecosystem because they alter the natural water flow and can modify the water cycle, diminishing precipitation. Sediments, that are biomasses, decompose in reservoirs, releasing greenhouse gases like methane and carbon dioxide in amount even bigger than the one produced using fossil fuels. For the reasons explained hydropower can be considered as cheap and mature technology with non negligible environmental costs, especially for biggest dams.

Biomass refers to all organic materials that stem from green plants as result of the photosynthesis and is generally composed of cellulose, hemicellulose and lignin (that are the three main components), lipids, proteins, simple sugars and starches. Water and inorganic molecules are also contained in the biomass. The elementary composition depends on the source and it can be summarized in carbon (50wt.%), oxygen (40wt.%), hydrogen (5wt.%) and chlorine (0.01-2wt.%).

Biomass can be considered as a stored source of solar energy in form of chemical energy which can be released and used, when the chemical bonds are broken. Biomass is considered to be CO_2 neutral because the carbon dioxide produced during combustion is recaptured by plants regrowth through photosynthesis. Further, biomass combustion produces lower amount of NO_x and SO_2 than fossil fuels.

Biomass and residues can be converted into energy via thermo-chemical and bio-chemical/biological processes but, in comparison with fossil fuels have lower heating values [6]. Further the energy density (bulk density) is 10-40% lower of that of most fossil fuels. The volatile matter content is higher for biomass (80%) than fossil fuel (20%), that means high ignition stability so it is easy to transform it, by a thermochemical method, into other fuels such as hydrogen and methanol. Generally thermochemical processes have higher efficiencies than biochemical/biological processes in terms of time: a thermo process needs few second or minutes to be completed and a bio-process need days or week or even more to be completed. Further, a thermo-process destroys more organic compound than a bio- process; an example is lignin that is not fermentable but can be easily decomposed via a thermo process.

Thermo-chemical conversion of biomass into *bio*energy can be effected via:

1. Direct combustion to provide heat, for steam production and hence electricity generation,
2. Gasification to provide a gaseous fuel for combustion,

3. Pyrolysis to provide charcoal,
4. Fast pyrolysis to provide a liquid fuel.

Thermochemical processes are pyrolysis, liquefaction, gasification and combustion. Via combustion the energy stored in the biomass can be used directly as heat otherwise it can be converted into solid (charcoal), liquid (oil), gas (syngas) to use as fuels.

As estimated by the World Energy Council, the biomass generating capacity expressed in Watt come after wind and hydropower.

The cost of energy produced with biomass depend on availability and type of fuel, that influence the transportation costs. Capital costs are similar to those for fossil fuel plants but it can be reduced by recovery and use of waste, making the process more efficient.

One advantage in the use of biomass is that the overall carbon dioxide production is zero, or less than zero if biomasses are burned in a plant with a carbon dioxide sequestration system. The technology to use this source is well developed and efficient, especially in case of co-generation of energy and heat. Actually this is the only technology that reduce the amount carbon dioxide in the atmosphere, also if additional cost are added.

The main problem is that the energy market cannot compete with the food market so the amount of land useful for biomass cultivation decrease and clearing land for biomasses cultivation can produce more emissions than fossil fuel use. The use of wastes and residues partially solve the problem because it is not a long term sustainable solution.

Biomass can be used to produce liquid fuel for transport purpose, and their use for energy production is desirable in a small scale system near the production area of the biomass.

Wind power generation is expanding faster, for example the United States added 35% of the country's generating capacity in 2007 and they are rapidly increasing. Globally the wind generation capacity is increased of about 25% in each of the past five years, according to the Global Wind Energy Council. Despite this rapid increase the number of installed capacity remain small on a global scale, also because wind farms generate just 20% of their capacity.

Actually wind is competitive with coal as energy production cost.

The main advantage of wind is that it does not need fuel and the only cost is building and repairing the turbines and power lines. The technology is mature and reliable.

The only limitations to wind power are the intermittency and the location of the windiest place, that is usually far away the energy utilization place so new infrastructures must be built up, especially for offshore settings.

Wind power utilization also depends on public opinion that is also determining for building new centrals.

Geothermal centrals use the heat coming from the Earth's interior to produce energy. Actually only few countries (Costa Rica, El Salvador, Iceland, Philippines, Kenya) use geothermal to produce more than 15% of their electricity. Globally the use of geothermal is growing slowly because there are not new sources and the only increase in its use can be obtained using the heat from the earth to directly warm residential and industrial construction.

The cost of a geothermal system depend on the location and geological setting. As mentioned above geothermal can provide to a small amount of the energy demand and projections estimates that it can provide only a small part of the world energy demand, also using the most advanced technology. On the other hand geothermal energy does not require fuel and it is ideally suited to supply base load electricity, because it is regular.

Solar power can be turned into electricity using a solar cells (photovoltaic), devices that use semiconducting materials to convert sunlight directly into electricity, or solar thermal systems that use mirrors to focus the heat from the sun heating up a working fuel that work in a turbine. A standard commercial photovoltaic panel can convert 12-18% of sunlight into electricity and the most advanced panels have an efficiency more than 20%. Globally the solar industry is increased of six times in the past five years but the power generated is lower than the estimate capacity of the installed systems. Of all renewables the solar have, actually, the lowest capacity factor (14%).

Although the low capacity factor, it is meaningful that Earth receives enough energy every hour to supply world energy needs for a year. Theoretically the world's energy requirement can be satisfy by less than one tenth of the Sahara area. The advantage of solar energy is that it is unlimited and leaves no residues. The public opinion accept solar technology more than nuclear, wind or hydro power so the technology can be used to install solar panel above private buildings. The solar panel technology is also suitable for independent generation of energy outside the national grid. It is also clear that solar power technology can improve a lot in the next years to lower the cost and increase efficiency. Examples are the Archimede central in Sicily for the solar thermal and the Grätzel cells [15], that are dye-sensitized solar cell that can overcome the cost of crystalline panels.

There are also some limitations to solar power development first of all the day and night cycle because electricity cannot be generated during the night. Also clouds cause not predictable oscillations in the electricity production, that is why new systems where heat/electricity can be stored when the sun is shining have been developed. Another problem is that big installation in the desert needs a new grid to transport electricity to the end users.

The actual technology use some rare elements whose cost might increase in the future and with geological distribution is not completely known.

The solar energy is the long term most promising renewable source but its massive usage must be followed by a development of storage systems.

Nuclear energy can be included in the renewable sources of energy because the fuel represent only a small part of the value of energy and it is a CO_2-free emission technology. Nuclear fission is used in 438 reactors (at the end of 2008) already in operation with an overall capacity that contributed of 14% of the electricity generated worldwide, according to the International Atomic Energy Agency (IAEA) [7]. In 2008 the construction of ten new centrals will start. Most of them are in Asia, 28 of the 44 reactors under construction at the end of 2008 were in Asia. The IAEA projections for global growth in nuclear power in 2008 were revisited upwards. In the low projection case the global nuclear capacity increase of 5% in 2030 but these projections were done before the financial crisis in the late 2008. At the time of writing no projections had been published that analysed the consequences of the crisis.

Nuclear plants use uranium as fuel that is not a rare element and it is available. By IAEA and the Organisation for Economic Co-operation and Development (OECD) the undiscovered reserves and the use of other fuels, like thorium, can provide enough energy to satisfy the world demand.

Advantages of nuclear power are that the fuel used is relatively low cost and widespread so it is not afflicted by political factors. Another advantage is that nuclear power plants can run constantly at about 90% of capacity so they can be used to provide the basic load for a national grid.

Disadvantages are nuclear wastes. A nuclear power plant produce plutonium as a waste that must be stored for thousands years in a stable environment to avoid radiation leakage and must also be military controlled to avoid terrorist attacks. At the moment there is not technical and political solutions to this problem. Nuclear power is not always public accepted and this is significant because nuclear plant are extremely capital intensive and must be build up by governments, that are usually worried by public opinion.

Another disadvantage is that is not possible to divide the energy generation in nuclear plants by nuclear weapons construction.

Nuclear power generation can provide energy in the terawatt range without technical gaps and the real problem will be waste storage and to overcome the political problem.

For the next future the energy demand relies on fossil fuels. Renewables usage for electricity generation will increase but the main problem is that renewables sources cannot guarantee the minimum load for the electrical grid. For that reason nuclear can satisfy the basic load and wind, geothermal and hydropower can also satisfy a considerable amount of energy request.

Wind is, for the next future the renewable source that meet economical and output power request. Solar must be developed to be considered a powerful energy source.

To increase renewables use it is fundamental to develop an energy storage system because all the renewable are not continuous sources of energy. A good candidate material for energy storage is hydrogen.

The overall use of renewable sources, from 1950s to 2008 for U.S.A. is reported in the Fig. 7, data from [3] and [4]. Actually renewable sources cover 7% of the primary energy consumption, both in European Union (see Fig. 8) and U.S.A.

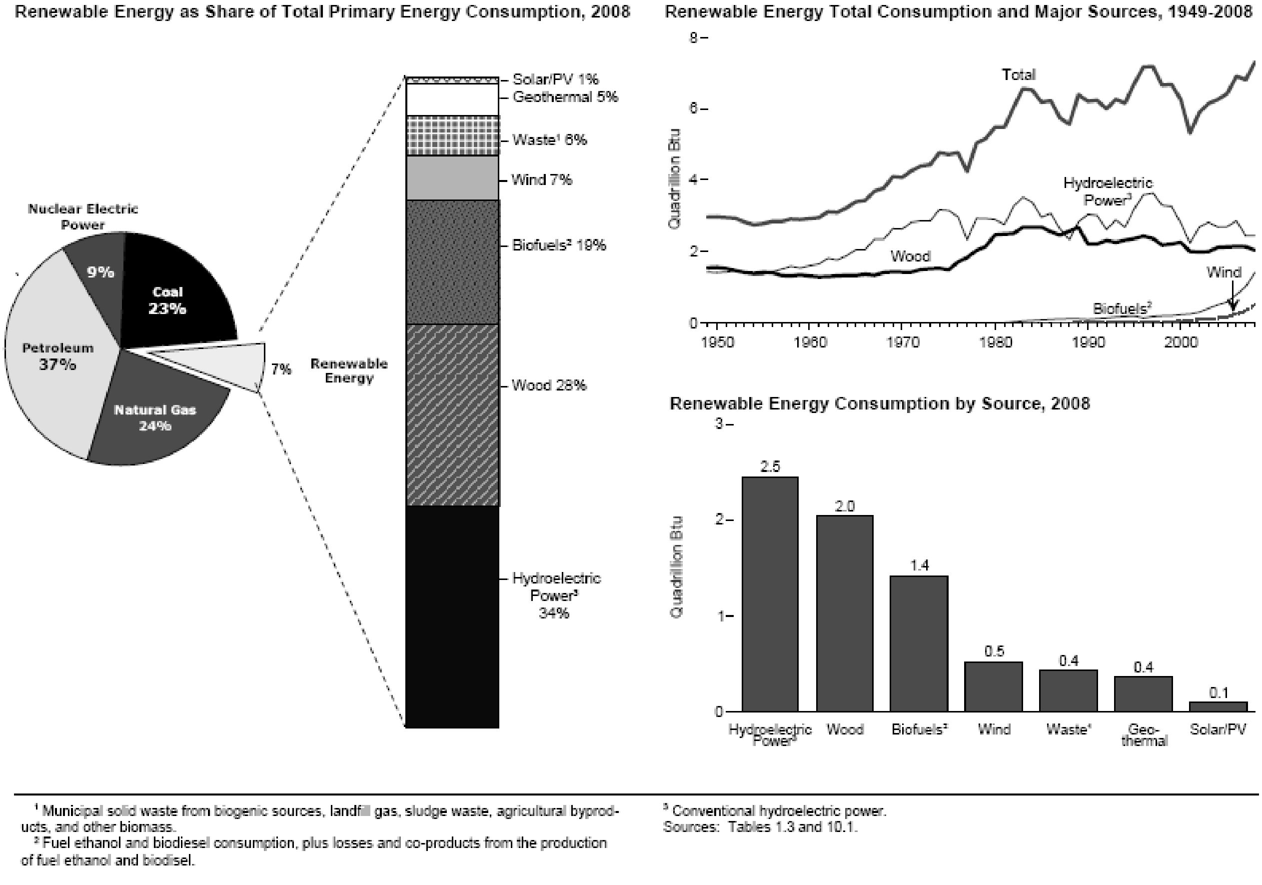

[1] Municipal solid waste from biogenic sources, landfill gas, sludge waste, agricultural byproducts, and other biomass.

[2] Fuel ethanol and biodiesel consumption, plus losses and co-products from the production of fuel ethanol and biodisel.

[3] Conventional hydroelectric power.

Sources: Tables 1.3 and 10.1.

Fig. 7. Overall use of renewable sources in the U.S.A. Detail about the graphs are reported in the figure [3].

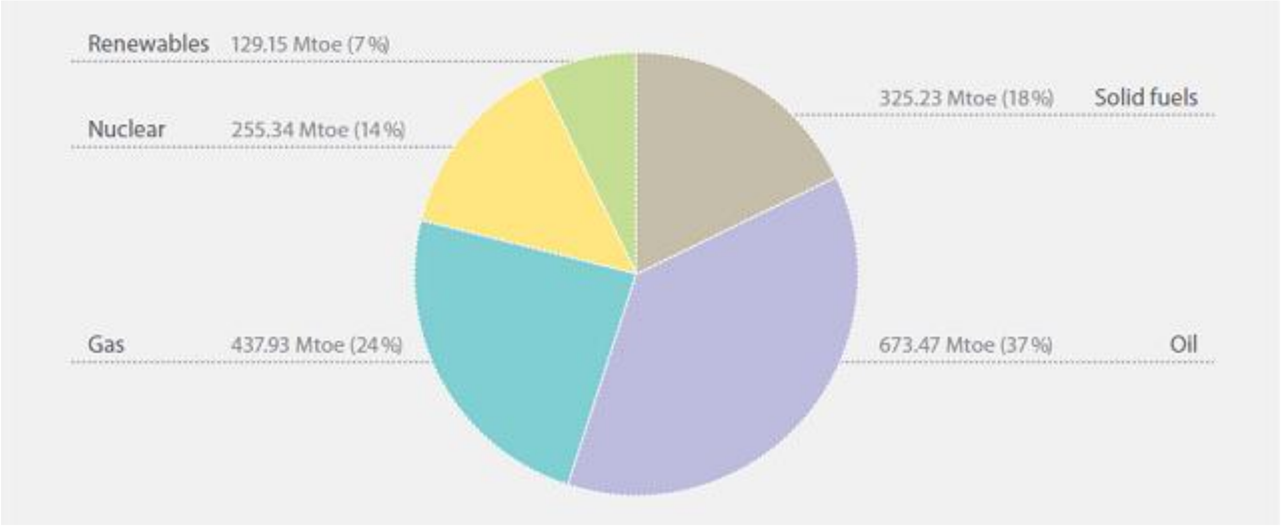

Fig. 8. Overall use of renewable sources in the 27 members European Union in 2006. Detail about the graphs are reported in the figure [4].

In U.S, but this data well defined the situation of developed countries, the main renewable resources used till now are biomasses, wood and biofuels included, and hydropower and their use, excluding biofuels, is constant from 1970s.

The third renewable source is wind power. Differently for hydropower and wood its usage is increasing from 1990s.

The solar energy, photovoltaic and thermal, produce a small part of the overall renewable production that is about 1% in the U.S. production.

A detailed graph, reporting the Renewable Energy Consumption from 1990s excluding the hydroelectric power generation is in Fig. 9.

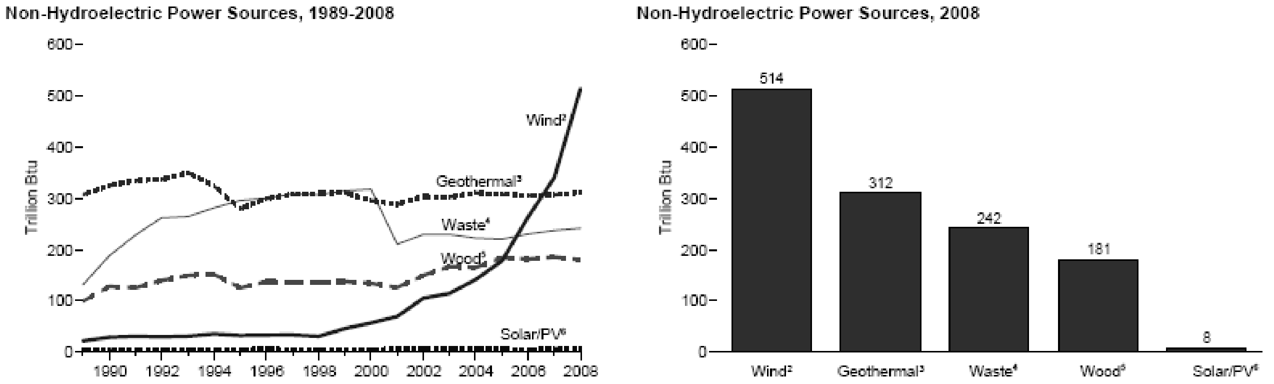

[1] Conventional hydroelectricity net generation.
[2] Wind electricity net generation.
[3] Geothermal electricity net generation.
[4] Municipal solid waste from biogenic sources, landfill gas, sludge waste, agricultural byproducts, and other biomass. Through 2000, also includes non-renewable waste (municipal solid waste from non-biogenic sources, and tire-derived fuels).
[5] Wood and wood-driven fuels.
[6] Solar thermal and photovoltaic electricity net generation.
Note: See related Figures 10.2a and 10.2b on the end-use sectors.
Source: Table 10.2c.

Fig. 9. Renewable energy consumption in U.S.A. Hydroelectric power is excluded [3].

At present no one of the renewable resources can replace fossil fuels in energy production. For that reason it is expected for the next years an increased use of renewable resources. The use till now and the prediction of the U.S. Department of Energy for renewables is reported in Fig. 10, [9].

The trend shown in the last decade for wind power generation will continue in the near, till 2013, and the growth will stop if no further government laws will be applied. Wind is the most promising renewable source and its capacity is expected to double the actual in the next three years.

The near term growth of other renewable capacity is limited. Geothermal capacity is restricted to a relative small amount of new sites and solar capacity is too costly for a widespread implementation. Energy from crops will not become economical before 2015 and other biomass resources will be used to produce biofuell instead of electricity.

As reported in Fig. 10 in the long term prediction renewable generation grows from a 9% share of total electricity production in 2008 to a 17% share in 2035 using a reference case in the predictions (see [3] for more details. The increase is supported by Federal tax, State programs and premium related to carbon free energy production.

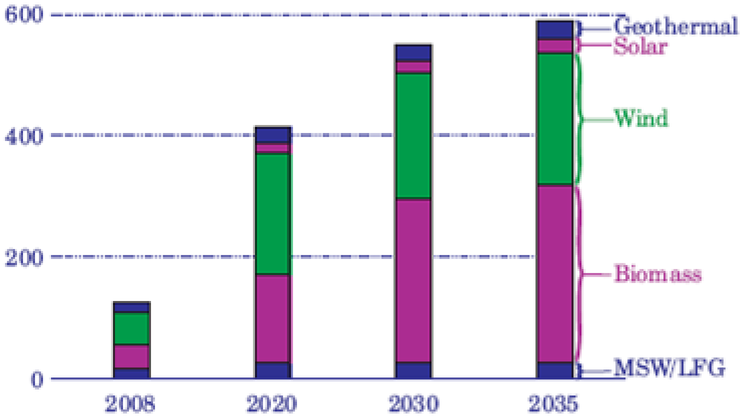

Fig. 10. Projections for non hydroelectric renewable electricity generation by source in U.S. [9].

Use of renewable energy resources in the electric power sector increases sharply in the AEO 2010 Reference case [9]. Non hydroelectric renewable generation accounts for 41% of the growth in total electricity generation from 2008 to 2035, supported by extension of Federal tax credits, State requirements for renewable electricity generation, and the loan guarantee program in EPACT 2005 (Energy Policy Act) and ARRA (American Recovery and Reinvestment Act). Wind power and biomass provide the largest share of the growth. Generation from wind power increases from 1.3% of total generation in 2008 to 4.1% in 2035. Generation from biomass, both in the electric power sector and from end-use cogeneration, grows from 0.9% of total generation in 2008 to 5.5% in 2035. A large portion of the increase in biomass generation comes from increased co-firing, a process in which biomass is mixed with coal in existing coal-fired plants, displacing some of the coal that would otherwise be burned [9].

In the low renewable cost case, costs for renewable generation technologies in 2035 are 25% lower than in reference case, but in the High Renewable cost case they do not change from the levels of 2009.

In the European Union the renewables predictions are similar to the U.S. one.

Renewables in comparison to the 1990s, gained almost three percentage points. Half of this increase was achieved during the years 2000-2006, reflecting the effectiveness of EU policies aimed at reducing CO_2 emissions and dependence on energy imports. However, the share of renewables still remains limited (7 % of primary energy consumption) and measures have been proposed by the European Commission to increase this share to 20 % in final energy consumption. In Fig. 11 is reported the electricity generation capacity, listed by technology.

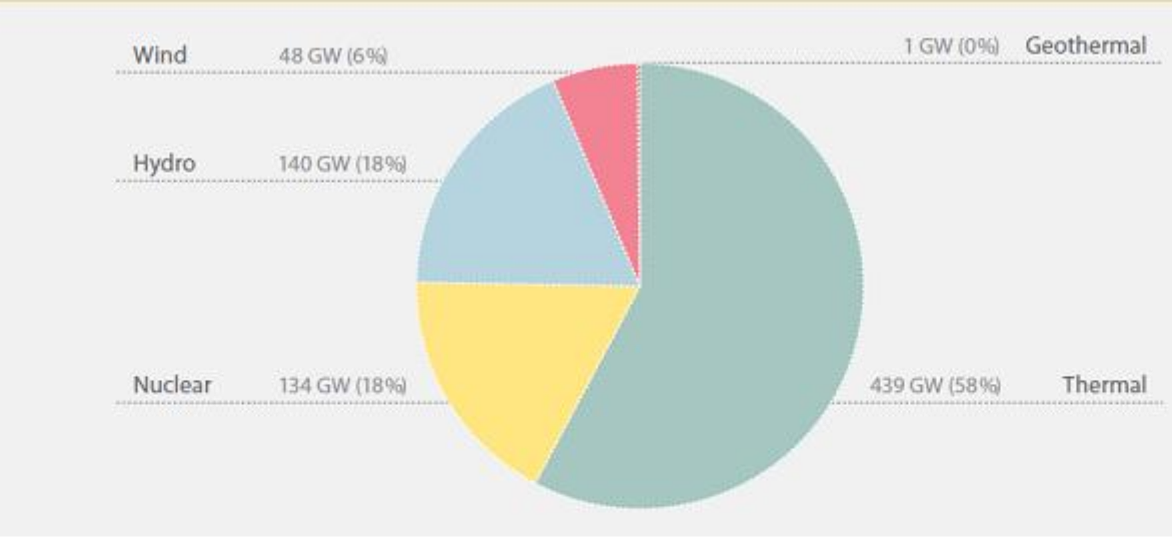

Fig. 11. Electricity generation capacity by technology for renewables sources in 27 members European Union [4].

As shown in the Fig. 11 (or in the Europe's Energy Position, present and future 2008) about 30% of power production is from nuclear.

Renewables have made their way into electricity production while undergoing at the same time a structural modification with an increase of wind and biomass and a relative decrease of hydro .With a view to energy security and to balancing supply and demand in particular in the case of peak of demand, the generation mix needs to offer generation flexibility between technologies. This also makes sense from an economic point of view since the generation costs vary according to technologies and load profiles.

As reported in Fig. 12 long term prediction renewables generation rises to 17.4% in 2010. The structure of power generation changes significantly in favour of renewables, natural gas and solid fuels, whereas nuclear and oil lose market shares. The baseline scenario shows a dynamic development of renewables in generate electricity, as the renewables share in gross generation rises further to 20% in 2020 and 23% in 2030. This development is clearly driven by the high grow rate of wind energy that continue in the next decades. It is expected that in 2030 wind power produce as much electricity as hydropower [10].

Biomasses use for power generation also increases considerably, solar photovoltaic shows high growth rates, while hydropower increase is small as result of limited additional potential and environmental restriction. Nuclear power generation decreases due to political decisions: the nuclear share falls from over 30% today to 20% in 2030 despite considerable investment in new nuclear plants.

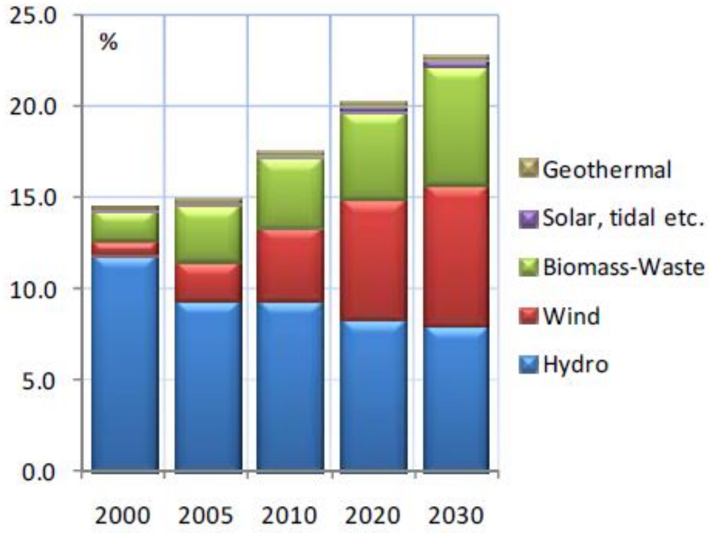

Fig. 12. Prediction in the renewables for energy production for the 27 members European Union [10].

If the trend for the energy market and consumption shows an increase in renewables usage and development, the scenario for automotive market is completely different. As reported in Fig. 3 the transportation energy consumption completely rely on petroleum.

Automotive

In industrialized countries the automotive market is saturated but in the developing countries an increasing demand for transportation services is expected. For example in China the average vehicle population growth is evaluated in about 13% per year in the past 20 year and it is projected to continue for the next decade. For developing countries the growth is expected to be about 4% per year. The global increase in vehicle population will increase the amount of greenhouse gas emissions and the amount of air pollutants emissions. The burning of fossil fuels in a engine produce the direct emissions of carbon monoxide and dioxide, volatile organic compounds and nitrogen oxides. There is also an indirect effect on the environment because secondary nitrate and sulphate particulates formed from NO_x and SO_x direct emission. The reduction of pollutants in the urban area is pushing the research to zero emissions vehicles. For that a variety of alternative transportation technology and fuels have been proposed to solve the future environmental and energy security challenges. The new vehicle technologies include advanced internal combustion energy, technologies based on spark-ignition or compression ignition engines, hybrid electric vehicles, battery powdered and fuel cell vehicles. Lower polluting fuels like reformulate gasoline or diesel, compressed natural gas, methanol, ethanol and hydrogen has been suggested [2]. The use of alternative fuels can reduce the emission of greenhouse gases and pollutants but also it can diversify the primary energy supply leading to a stable fuel market.

Recent studies have identified fuel cell vehicles working with hydrogen as the ones offering the lowest fuel cycle emissions and also the widest range of primary supply options.

Polymer Electrolyte Membrane Fuel Cells

Polymer Electrolyte Membrane (PEM) fuel cells, fuelled with hydrogen and oxygen, are currently the cells that meet the automotive requirements for light-duty vehicles, operating at low temperatures, quick start and adequate output power. Hydrogen can be stored as compressed gas, that is actually simpler to design, or produced onboard with a reformer that convert methanol or ethanol in hydrogen. Hydrogen is the best long term option for automotive systems in terms of vehicle first cost and life cost and also because it meet the environmental requirements for the future.

Fuel cells directly convert chemical energy into electrical energy, without the intermediate formation of mechanical energy as in conventional energy conversion devices based on the Carnot cycle. The direct electrochemical energy conversions of H_2 at the *anode* and O_2 at the *cathode* occur spatially separated on two electrodes connected by electrolyte and, in principle, allow for higher energy conversion efficiencies. The largest efficiency differences between Carnot based and fuel cell-based energy conversion are found in the low power range of <1 MW and especially <100 kW. These efficiency advantages minimize fuel consumption; furthermore, quasi-zero pollutant emission is a great advantage

Basic principles of Fuel Cells

The Gibbs free energy change of a chemical reaction is related to the cell voltage via:

$$\Delta G = -n F \Delta U_0 \qquad (1)$$

where n is the number of electrons involved in the reaction, F is the Faraday constant, and ΔU_0 is the voltage of the cell for thermodynamic equilibrium in the absence of a current flow.

For the case of a hydrogen/oxygen fuel cell the overall reaction is:

$$H_2 + \tfrac{1}{2} O_2 \rightarrow H_2O \qquad \text{with } \Delta G = -237 \text{ kJ mol}^{-1}$$

with an equilibrium cell ΔU_0 voltage for standard conditions at 25 °C of:

$$\Delta U_0 = -\Delta G / nF = 1.23 \text{ V} \qquad (2)$$

The equilibrium cell voltage is the difference of the equilibrium electrode potentials of cathode and anode which are determined by the electrochemical reaction taking place at the respective electrode:

$$\Delta U_0 = U_{0,c} - U_{0,a} \qquad (3)$$

Fuel cells are, from a thermodynamic point of view, galvanic cells that convert the free reaction energy in electrical energy. Energy efficiency of this reaction is higher than the one obtained burning the fuel with oxygen. This is simply demonstrable referring to H_2 combustion with O_2:

$$H_2 + \frac{1}{2} O_2 \rightarrow H_2O$$

Thermodynamic values are reported in Tab. 1 [14]. In electrochemical conditions the maximum energy available in a cell operating at constant temperature and pressure is

$$\Delta G° = \Delta H° - T \Delta S° \qquad (4)$$

Tab. 1. Thermodynamic values for H_2O formation from the elements [14].

	H_2	O_2	H_2O_l	H_2O_g
$\Delta H°_f$ (kJ/mol)	0	0	-285.83	-241.82
ΔG°f (kJ/mol)	0	0	-237.13	-228.53
S° (J/mol K)	130.684	205.138	69.91	188.83

At two different temperatures (T=298.15 K e T=1273.15 K, that refers to room temperature and maximum operating temperature of high temperature cell)

for T=298.15 K

$$\Delta S° = 69.91-130.684-205.138/2= - 163.343\ \mathrm{J\ K^{-1}\ mol^{-1}}$$

and

$$\Delta G^{o}= -237.13\ \mathrm{KJmol^{-1}}$$

similarly, for T=1273.15 K

$$\Delta S^{°} = 188.83-130.684-205.138/2= - 44.423\ \mathrm{J\ K^{-1}\ mol^{-1}}$$

$$\Delta G^{o}= -186.54\ \mathrm{KJ\ mol^{-1}}$$

In thermodynamically reversible conditions these ΔG^{o} values correspond to reversible potential, determinable from

$$\Delta G° = - n\ \mathrm{F}\ \mathrm{E_{rev}} \qquad (5)$$

n = number of electrons exchanged (for the used stoichiometry n =2),
F = Faraday constant(96500 Coulomb/mol),
E_{rev} = reversible cell potential, maximum potential difference for a cell in themodynamic reversibility.

(T=298.15 K)

$$E_{rev} = - \Delta G°/nF = - \Delta G°/2F= 1.229\ \mathrm{V} \qquad \mathrm{(NHE)}$$

(T=1273.15 K)

$$E_{rev} = - \Delta G°/nF = - \Delta G°/2F= 0.966\ \mathrm{V} \qquad \mathrm{(NHE)}$$

Under chemical conditions combustion reaction leads to a variation of the free energy, ΔG°, that correspond to the heat exchanged ΔH°:

$$\Delta G° = \Delta H° = -241.82\ \mathrm{KJ\ mol^{-1}}$$

Considering that, in this case the reaction energy efficiency depends also from the associated Carnot cycle,

$$\eta = 1 - \frac{T_c}{T_h}$$

Where T_h is the hot source temperature and T_c correspond to cold source. Assuming for simplicity $T_c= 0.5\ T_h$ ($\eta \cong 50$), the maximum energy from a chemical H_2 combustion is

$$\Delta G°\times 0.5 = \Delta H°\times 0.5 = -120.91\ (\mathrm{KJ\ mol^{-1}})$$

For comparison with the electrochemical reaction ($\Delta G°=-237.13\ KJmol^{-1}$ a $T_1=298.15$ Ke $\Delta G°=-186.54\ KJmol^{-1}$a $T_2 = 1273.15$ K) it is clear that the energy from a fuel cell is higher than hydrogen chemical combustion.

Despite these conceptual advantages of fuel cells and their long development history since Grove's discovery in 1893 [1], no real fuel cell markets exist as of today. The reason for this is their high costs, caused mainly by the required materials and their relatively short lifetime in relation to competitive technologies. Their future market introduction is expected at first for portable applications, followed by stationary applications and finally for transportation applications. This expectation is based on the strong commitment of the car industry, the development of better and cheaper materials and the use of modeling methods to improve fuel cell and fuel cell system efficiencies. Among the different fuel cell types, the low-temperature proton exchange membrane fuel cell (PEMFC), the direct methanol fuel cell (DMFC), the high-temperature molten carbonate fuel cell (MCFC) and the solid oxide fuel cell (SOFC) play the most important roles; historically, the phosphoric acid fuel cell (PAFC) and alkaline fuel cell (AFC) had significant importance. Caused by the low operating temperature of PEMFCs and DMFCs, electrocatalysis-related issues are more critical than in the case of high-temperature fuel cells. For automotive application PEMFCs are the most attractive fuel cells. A summary of fuel cell systems is reported in Tab.1.

Tab. 1. Fuel cell types and applications.

	AFC Alkaline	**PEMFC** Polymer Electrolyte	**DMFC** Direct Methanol	**PAFC** Phosphoric acid	**MCFC** Molten Carbonate	**SOFC** Solid Oxide
Temperature °C	< 100	60-120	60-120	160-220	600-800	800-1000
Anodic reaction	$H_2+2OH^- \rightarrow 2H_2O + 2\ e^-$	$H_2 \rightarrow 2H^+ +2e^-$	$CH_3OH+H_20 \rightarrow CO_2+6H^+ +6e^-$	$H_2 \rightarrow 2H^+ +2e^-$	$H_2+CO_3^= \rightarrow H_2O+CO_2+2e^-$	$H_2+O^= \rightarrow H_2O+2e^-$
Cathodic reaction	$½O_2+H_2O+2e \rightarrow 2OH^-$	$½O_2+H_2O+2e \rightarrow 2OH^-$	$3/2O_2+6H^+ +6e \rightarrow 3H_2O$	$½O_2+2H^+ +2e \rightarrow H_2O$	$½O_2+CO_2+2e \rightarrow CO_3^=$	$½O_2+2e \rightarrow O^=$
Use	Transports, space applications and Energy storage			Energy-heat produvtion in stationary systems	Energy-heat production in stationary systems; transport (trains, ships)	
Power output	Small modular power unit (5-150 kW)	Small modular power unit (5-250 kW)	Small power unit (5 kW)	Medium small power unit (50kW-11MW)	Small power unit (100kW-2MW)	Small power unit (100-250kW)
Electrolyte charge transport	OH^-	H^+	H^+	H^+	$CO_3^=$	$O^=$

PEMFCs are energy conversion devices that work in a gas streams and liquid solutions that are oxidizing (O_2 or air) or reducing (H_2) and work in the electrochemical potentials window induced by the cell reaction [2]. All the component materials (supply lines, tanks, pumps, sensors, filters etc.) in contact with aqueous phase are subjected to corrosion. In particular the bipolar plate/current collector are subjected to corrosion due to their role in the cell, they electrically connect adjacent cell in the stack and distribute fuel and oxidant to the anode and cathode respectively. For that reason materials used must have good electrical conductivity and good resistance to corrosion across a range of oxidizing potentials. Such materials should also be easy to manufacture, hard to bend, light and not to expensive. Usually the bipolar plate are made of machined graphite but alternatives corrosion resistant materials like alloys (stainless steels, titanium, aluminium), conductive polymers and new graphitic materials are emerging.

The goal for fuel cells in the automotive market is to develop and demonstrate power system technologies for transportation, stationary and portable applications. The objectives are to obtain, by 2010, a 60% peak efficiency, durable, direct hydrogen fuel cell power system for transportation at cost of $45/kW, this being comparable with the cost of an internal combustion engine, and by 2015 a cost of $30/kW.

The technical approach aims to obtaining high efficiency and durability with low material and manufacturing costs. Others related results are better performing balance-of-plant components like air compressors, water and heat management systems and sensors. To meet the requirements of durability and efficiency the research is focussing on finding new materials and new methods to design and fabricate membranes, cathode catalysts and supports, cell hardware like bipolar plates and seals, and accessorises like compressors, radiators humidifiers. The most challenge is to develop durable and low cost membrane and catalysts that can also operate in a wide range of daily use conditions

Another component fundamental to determine the cell efficiency is the proton conducting membrane. An effective membrane electrolyte for PEFCs, besides acting as a physical separator for the fuel and oxidant, must possess high ionic conductivity with little electronic component [11].

It should be possible to cast them as thin and large surface-area membranes. The membranes should be stable in oxidizing and reducing environments prevailing during the operation of the PEFCs. The membrane must be easy to manufacture and able to withstand the stress during electrode processing and attachment, and should be both mechanically and electrically robust to endure the start-up and shutdown schedules of the PEFCs [11].

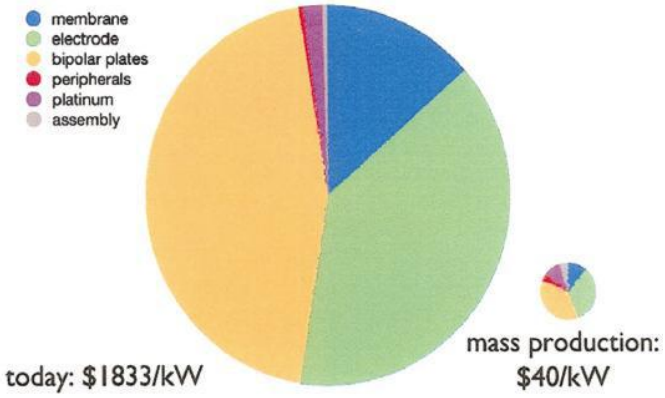

Fig. 13. Estimated cost per kW for PMEFC stack [11].

The membrane is usually a polymer made of tetrafluoroethylene backbone with sulfonated groups covalently bounded to the alkyl chain. The most common commercially available perfluorinated membranes are Nafion (DuPont), Flemion (Asahi Glass) and Aciplex (Asahi Chemicals). The membranes have different properties and thickness that affect the transport properties.

The problem with platinum

In the PEMFC, but also in the Direct Methanol Fuel Cells (DMFCs) and Phosphoric Acid Fuel Cells (PAFCs) the electrode reactions, particularly the reduction of oxygen, are catalyzed by Platinum nanoparticles. As mentioned above the PEMFs are the most promising technology for automotive systems but the high costs limit they commercialization, especially for an application like transport that involve millions of vehicles in the world. Currently the high cost of a fuel cell arises from the Pt necessary to electrocatalyze the oxygen reduction reaction. The hydrogen oxidation is ten time faster than the oxygen reduction so the platinum need is lower. For example the cost of the Pt for a small 100 kW car is higher than the cost of an entire gasoline engine with the same output power. The cost is not the only problem related to Pt because under operating conditions the Pt is oxidized and suffers migration, oxidation, loss of active surface area and corrosion of the carbon support. Another problem is that Pt is subjected to poisoning, i.e. by carbon monoxide, so the activity and efficiency are reduced.

To commercialize PEMFCs in automotive systems it is necessary to overcome the problems related to Pt. The solutions proposed are: more efficient use of noble metals, better Pt recycling and replacing Pt entirely [12].

Platinum cost is high and volatile because deposits are concentrated in a few countries and are definitely finite. Geological studies demonstrate that it is non probable to find new stocks of this precious metal and it is found mainly in the south of Africa and Russia. It is thought that about 80% of the world's Pt resources are located in the south of Africa alone. This situation and the projected increasing request for the large number of utilization means that Pt will be subjected to limitations, like other minerals with industrial interest like copper, nickel and zinc (suggested by Graedel studies). Pt prices have traditionally cycled depending on supply and demand. Increasing demand for fuel cell applications could drive costs prohibitively high.

Concerns about the security of supply as well as the actual amount of Pt available are therefore rife. The high and volatile price of Pt alone could be a potential inhibition to fuel cells mass market application. According to research by Thomas E. Graedel and colleagues [16] at Yale University, who have taken a novel approach to the modeling of metal stocks, the global Pt resources currently known would sustain a fleet of 500 million fuel cell vehicles for just 15 years. It is relevant that this projection does not take into account the Pt use for other uses like stationary fuel cells, industrial catalysts converters and jewellery. This model also does not consider the growth of automotive market in developing countries and the effect of this growing demand on the Pt price. The issue will be similar to fossil fuels, limited supply concentrated in a few countries in the world and prices that depend on the market. That means that Pt will have the same problems that now fossil fuels have.

It is clear that Pt usage is an issue for mass commercialization of fuel cells that is why research is moving on reduce the amount of catalyst, the targeted Pt loading for automotive applications is 0.1 mg cm^{-2} per electrode in 2015, [13] down to its theoretical minimum of a monolayer or using it in alloy.

A long term plan and the massive commercialization of fuel cell cannot rely on platinum catalyst, as explained above. For that reason it is fundamental to search for non-noble metal catalysts for oxygen reduction reaction (ORR) in acidic medium.

In this thesis, nitrogen doped, noble metal-free, carbonaceous material were synthesised and their catalytic activity toward oxygen reduction reaction was studied with electrochemical methods. The synthesised materials were also characterized with chemical and physical methods.

References

[1] U. S. Department of Energy web site, http://www.eia.doe.gov.

[2] "*Hanbook of fuel cel, Foundamentals, Technology and Applicationl*", W. Vielstich, A. Lamm, H. A. Gasteiger, 2003. Vol.3 part. 1.

[3] "*Annual Energy Review 2008*", Energy Information Administration Office of Energy Markets and End Use U.S. Department of Energy Washington, DC 20585June 2009, http://www.eia.doe.gov/emeu/aer/pdf/aer.pdf.

[4] "*European energy and transport, trends to 2030,update 2007*", Directorate General for Energy and Transport, 2008, http://europa.eu.

[5] Q. Schiermeier, J. Tollefson, T. Scully, A. Witze, O. Morton, *Nature*, 454 (2004), 816.

[7] L. Zhang, C- X. Chunbao, P. Champagne, *Energy Conversion and Management*, 51 (2010**)**, 969.

[8] "*Nuclear technology Review – 2009*", International Atomic Energy Agency, 2009.

[9] "*Annual Energy Outlook 2010, With Projections to 2035*", Energy Information Administration Office of Energy Markets and End Use U.S. Department of Energy Washington DC, June 2010, http://www.eia.doe.gov/oiaf/aeo/pdf/0383%282010%29.pdf.

[10] "*Europe's Energy Position, present&future*", Directorate General for Energy and Transport, 2008, http://europa.eu

[11] A. K. Sahu, S. Pitchumani, P. Sridhar, A. K. Shukla, *Bull. Mater. Sci.*, 32 (2009), 285.

[12] C. Sealy, *Materials Today*, 11 (2008), 65.

[13] "*Multi-Year Research, Development and Demonstration plan: Planned Program Activities for 2005-2015*" U.S. Department of Energy, (2007), Section 3.4, p 24. http://www1.eere.energy.gov/hydrogenandfuelcells/mypp/pdfs/fuel_cells.pdf.

[14] Atkins, J. De Paula, "*Physical Chemistry*", (7th edition), Oxford University, pp. 1080-1082.

[15] N. Tétreault, E. Horvàth, T. Moehl, J. Brillet, R. Smajda, S. Bungener, N. Cai, P. Wang, S. M. Zakeeruddin, L. Forrò , A. Magrez, M Greatzel, *ACS Nano*, "High-Efficiency Solid-State Dye-Sensitized Solar Cells: Fast Charge Extraction through Self-Assembled 3D Fibrous Network of Crystalline TiO_2 Nanowires".

[16] M. Gerst, T. E. Graedel, *Environmental Science and Tech.*, 42 (2008), 7038.

Platinum catalysts

1.1 Introduction

Oxygen reduction occurs along a number of consecutive steps, each of them being possibly the rate-determining one. The overall reaction rate is affected by different and specific properties of the electrode material like electronic (work function, *d*-band character), adsorption energy of intermediates, geometrical surface atom arrangements and surface defectivity.

To develop new catalysts and to organize a systematic catalytic study a detailed analysis of the reaction mechanism for a given electrocatalyst is necessary.

A rational approach to the research of better electrocatalysts depends on the intermediated material and the complexity of the reaction itself. A major part of the studies on electrocatalyzed oxygen reduction has been done on noble metals or their alloys, because such materials do not dissolve at the high electrode potentials relevant to oxygen reduction (0.8 to 1.1 V RHE).

At high potentials where the reaction occurs the electrode surface is generally covered by oxide or partially covered by adsorbed oxygen or OH.

Further, a mechanistic analysis of oxygen reduction is made complex by the many reaction steps and intermediates, these latter involving adsorption energy that varies with varying electrode potential and intermediate coverage. Also impurity traces may affect the reduction, especially at low current densities where impurities may enter in potential controlling reactions.

1.2 Mechanism for ORR

The oxygen reaction mechanism has been the subject of many studies over the past century. The very strong irreversibility of the anodic and cathodic processes in aqueous solutions has limited the information which can be obtained from electrochemical kinetic studies about the pathway, the reaction order etc. Moreover, in aqueous solutions the surfaces of metal electrodes are covered with oxygen species, either physically adsorbed or chemically bonded, e.g. oxides, which modify the electrode surface state and, finally, the overall mechanism of the oxygen reduction [25]. Damjanovic et al. [26] showed that the presence and the quantity of platinum oxides or oxygen adsorbed species onto Pt surface, immersed in an oxygen-rich solution, are a function of the applied potential and time. They suggested that in the potential region below 0.78 V vs AgCl/Ag oxygen or oxygen containing species are adsorbed at the surface, but, in the region above this potential, platinum oxides are prevailing.

Proposed mechanisms for ORR on Pt are based on these considerations and they are reported in [2]. To discriminate between these pathways and to identify the path for investigated catalysts it is important to have available diagnostic criteria for each mechanism. The most often determined “kinetic” parameters in mechanism studies are the Tafel slope, $\left(\frac{\partial \Delta\Phi}{\partial \ln i}\right)$, the symmetry factor, β, the reaction order, $\left(\frac{\partial \ln i}{\partial \ln p_{O_2}}\right)$, and the dependence of ln *i* from pH, $\left(\frac{\partial \ln i}{\partial (2.3pH)}\right)$.

These parameters are obtained from mechanistic considerations applied on each single step of a specific mechanism. Since in these pathways adsorbed species are involved, it is necessary to consider different types of adsorption isotherms in the derivation of diagnostic parameters. Usually, either Langmuir, for low or very high coverage, or Temkin-type isotherm, for intermediate, are taken in account.

In the following it is reported an example of the determination of kinetic parameters applied to Damjanovich’s path, which is the most credited mechanism for oxygen reduction onto platinum:

1) $O_2 \rightarrow 2O_{ads}$

2) $O_{ads} + H_2O \rightarrow (O-H-OH)_{ads}$

3) $(O-H-OH)_{ads} + e^- \rightarrow (O-H-OH)^-_{ads}$

4) $(O-H-OH)^-_{ads} + H^+ \rightarrow OH_{ads} + H_2O$

5) $OH_{ads} + e^- + H^+ \rightarrow H_2O$

Langmuir adsorption conditions

The rate of a generic reaction $A^+ + e^- \rightarrow A$ under the influence of an electrical field can be written as:

$$\vec{v}_e = \frac{kT}{h} c_{A^+} e^{-\frac{\Delta\vec{G}^{\circ\neq}}{RT}} = \vec{k}_c c_{A^+} e^{-\frac{(1-\beta)F\Delta\Phi}{RT}}$$

where k, T, h, R, T have the usual meaning, β is the charge transfer symmetry factor, $\Delta G^{\circ\neq}$ is the total standard free energy of activation for this reaction and it is equal to the chemical free energy, $\Delta G_c^{\circ\neq}$, plus the electrical contribution, $(1-\beta)F\Delta\Phi$:

$$\Delta G^{\circ\neq} = \Delta G_c^{\circ\neq} + (1-\beta)F\Delta\Phi$$

$$\vec{k}_c = \frac{kT}{h} e^{-\frac{\Delta \vec{G}_c^{\circ\neq}}{RT}}$$

Current, *i*, is equal to $i = F\vec{v}_e$.

In the presence of an “ideal” adsorption, either low or high coverage, a Langmuir type isotherm is used and a variation of $\Delta G_c^{\circ\neq}$ due to the apparent standard free energy of activation for adsorption $\Delta G_0^{0\neq}$ is considered. This term is independent from the surface coverage and it is proportional to ΔG_0^0, the adsorption standard free energy.

Kinetic equations for Damjanovich’s mechanism become:

$$\vec{v}_1 = \vec{k}_1 \times p_{O_2}$$
$$\overleftarrow{v}_1 = \overleftarrow{k}_1 \times \theta_O^2$$
$$\vec{v}_2 = \vec{k}_2 \times \theta_O$$
$$\overleftarrow{v}_2 = \overleftarrow{k}_2 \times \theta_{O-H-OH}$$
$$\vec{v}_3 = \vec{k}_3 \times \theta_{O-H-OH} \times e^{\left(\frac{-(1-\beta)F\Delta\Phi}{RT}\right)}$$
$$\overleftarrow{v}_3 = \overleftarrow{k}_3 \times \theta_{O-H-OH^-} \times e^{\left(\frac{\beta F\Delta\Phi}{RT}\right)}$$
$$\vec{v}_4 = \vec{k}_4 \times \theta_{O-H-OH^-} \times c_{H^+}$$
$$\overleftarrow{v}_4 = \overleftarrow{k}_4 \times \theta_{OH}$$
$$\vec{v}_5 = \vec{k}_5 \times \theta_{OH} \times c_{H^+} \times e^{\left(\frac{-(1-\gamma)F\Delta\Phi}{RT}\right)}$$

where *k* is the kinetic constant, θ_x the surface coverage of the x species, β and γ the symmetry factors for the charge transfer step 3) and 5).

If the Rate Determining Step (RDS) is the 1st one

$$i = F \times \vec{k}_1 \times p_{O_2}$$

for low coverage, $\theta \to 0$

$$\ln(i) = C + \ln(p_{O_2})$$

$$\left(\frac{\partial \Delta\Phi}{\partial \ln i}\right)_{p_{O_2}} = \infty\,; \left(\frac{\partial \ln i}{\partial \ln p_{O_2}}\right) = 1; \left(\frac{\partial \ln i}{\partial(2.3pH)}\right) = 0$$

If the Rate Determining Step (RDS) is the 2nd one

$$i = F \times \vec{k}_2 \times \theta_O$$

for low coverage, $\theta \to 0$, and on the quasi-equilibrium hypothesis of step 1):

$$\vec{k}_1 \times p_{O_2} = \overleftarrow{k}_1 \times \theta_O^2$$

$$\theta_O = C \times p_{O_2}^{0.5}$$

$$\ln(i) = C + 0.5 \times \ln(p_{O_2})$$

$$\left(\frac{\partial \Delta\Phi}{\partial \ln i}\right)_{p_{O_2}} = \infty\, ; \left(\frac{\partial \ln i}{\partial \ln p_{O_2}}\right) = 0.5\, ; \left(\frac{\partial \ln i}{\partial(2.3pH)}\right) = 0$$

for high coverage, $\theta \to 1$,

$$\ln(i) = C$$

$$\left(\frac{\partial \Delta\Phi}{\partial \ln i}\right)_{p_{O_2}} = \infty\, ; \left(\frac{\partial \ln i}{\partial \ln p_{O_2}}\right) = 0\, ; \left(\frac{\partial \ln i}{\partial(2.3pH)}\right) = 0$$

If the Rate Determining Step (RDS) is the 3rd one

$$i = F \times \vec{k}_3 \times \theta_{O-H-OH} \times e^{\left(\frac{-(1-\beta)F\Delta\Phi}{RT}\right)}$$

for low coverage, $\theta \to 0$, and on the quasi-equilibrium hypothesis of step 2) and 1):

$$\vec{k}_2 \times \theta_O = \overleftarrow{k}_2 \times \theta_{O-H-OH}$$

$$\theta_{O-H-OH} = C \times \theta_O = C \times p_{O_2}^{0.5}$$

$$i = C \times p_{O_2}^{0.5} \times e^{\left(\frac{-(1-\beta)F\Delta\Phi}{RT}\right)}$$

$$\ln(i) = C + 0.5 \times \ln(p_{O_2}) - \frac{(1-\beta)F\Delta\Phi}{RT}$$

$$\left(\frac{\partial\Delta\Phi}{\partial\ln i}\right)_{p_{O_2}} = -\frac{RT}{(1-\beta)F}\,;\ \left(\frac{\partial\ln i}{\partial\ln p_{O_2}}\right) = 0.5\,;\ \left(\frac{\partial\ln i}{\partial(2.3pH)}\right)=0$$

for high coverage, $\theta \to 1$,

$$i = F \times \vec{k}_3 \times e^{\left(\frac{-(1-\beta)F\Delta\Phi}{RT}\right)}$$

$$\ln(i) = C - \frac{(1-\beta)F\Delta\Phi}{RT}$$

$$\left(\frac{\partial\Delta\Phi}{\partial\ln i}\right)_{p_{O_2}} = -\frac{RT}{(1-\beta)F}\,;\ \left(\frac{\partial\ln i}{\partial\ln p_{O_2}}\right) = 0\,;\ \left(\frac{\partial\ln i}{\partial(2.3pH)}\right)=0$$

If the Rate Determining Step (RDS) is the 4th one

$$i = \vec{k}_4 \times \theta_{O-H-OH^-} \times c_{H^+}$$

for low coverage, $\theta \to 0$, and on the quasi-equilibrium hypothesis of step 3), 2), 1):

$$\vec{k}_3 \times \theta_{O-H-OH} \times e^{\left(\frac{-(1-\beta)F\Delta\Phi}{RT}\right)} = \overleftarrow{k}_3 \times \theta_{O-H-OH^-} \times e^{\left(\frac{\beta F\Delta\Phi}{RT}\right)}$$

$$\theta_{O-H-OH^-} = C \times p_{O_2}^{0.5} \times e^{\left(-\frac{F\Delta\Phi}{RT}\right)}$$

$$i = C \times c_{H^+} \times p_{O_2}^{0.5} \times e^{\left(-\frac{F\Delta\Phi}{RT}\right)}$$

$$\ln(i) = C + 0.5\ln\left(p_{O_2}\right) + \ln\left(c_{H^+}\right) - \frac{F\Delta\Phi}{RT}$$

$$\left(\frac{\partial\Delta\Phi}{\partial\ln i}\right)_{p_{O_2}} = -\frac{RT}{F}\,;\ \left(\frac{\partial\ln i}{\partial\ln p_{O_2}}\right) = 0.5\,;\ \left(\frac{\partial\ln i}{\partial(2.3pH)}\right)=1$$

for high coverage, $\theta \to 1$,

$$i = C \times c_{H^+}$$

$$\left(\frac{\partial\Delta\Phi}{\partial\ln i}\right)_{p_{O_2}} = \infty\,;\ \left(\frac{\partial\ln i}{\partial\ln p_{O_2}}\right) = 0\,;\ \left(\frac{\partial\ln i}{\partial(2.3pH)}\right)=1$$

If the Rate Determining Step (RDS) is the 5th one

$$i = F \times \vec{k}_5 \times \theta_{OH} \times c_{H^+} \times e^{\left(\frac{-(1-\gamma)F\Delta\Phi}{RT}\right)}$$

for low coverage, $\theta \to 0$, applying the quasi-equilibrium hypothesis

$$\vec{k}_4 \times \theta_{O-H-OH^-} \times c_{H^+} = \overleftarrow{k}_4 \times \theta_{OH}$$

$$\theta_{OH} = C \times p_{O_2}^{0.5} \times c_{H^+} \times e^{\left(-\frac{F\Delta\Phi}{RT}\right)}$$

$$i = C \times p_{O_2}^{0.5} \times c_{H^+}^{2} \times e^{\left(\frac{-(2-\gamma)F\Delta\Phi}{RT}\right)}$$

$$\ln(i) = C + 0.5\ln\left(p_{O_2}\right) + 2\ln\left(c_{H^+}\right) - \frac{(2-\gamma)F\Delta\Phi}{RT}$$

$$\left(\frac{\partial \Delta\Phi}{\partial \ln i}\right)_{p_{O_2}} = -\frac{RT}{(2-\gamma)F};\ \left(\frac{\partial \ln i}{\partial \ln p_{O_2}}\right) = 0.5;\ \left(\frac{\partial \ln i}{\partial (2.3pH)}\right) = 2$$

for high coverage, $\theta \to 1$,

$$i = C \times e^{\left(\frac{-(1-\gamma)F\Delta\Phi}{RT}\right)}$$

$$\ln(i) = C - \frac{(1-\gamma)F\Delta\Phi}{RT}$$

$$\left(\frac{\partial \Delta\Phi}{\partial \ln i}\right)_{p_{O_2}} = -\frac{RT}{(1-\gamma)F};\ \left(\frac{\partial \ln i}{\partial \ln p_{O_2}}\right) = 0;\ \left(\frac{\partial \ln i}{\partial (2.3pH)}\right) = 0$$

Temkin adsorption conditions

For intermediate coverage, $0.2<\theta<0.8$, it is more realistic to consider a dependence of the adsorption free energy from the coverage using a Temkin-like isotherm. In this case the adsorption standard free energy, ΔG_θ^0, proportional to the standard free energy of activation for adsorption, is equal to:

$$\Delta G_\theta^0 = \Delta G_0^0 + g\theta$$

where ΔG_0^0 and ΔG_θ^0 are the standard free energy of the adsorption corresponding to θ=0 and $\theta \neq 0$, respectively. g is an interaction lateral parameter. It has a negative sign when interactions between adsorbed species are attractive and positive in the opposite, repulsive, case. This term is strictly a free-energy parameter.

Kinetic equations for each step of the Damjanovich mechanism then become:

$$\vec{v}_1 = \vec{k}_1 \times p_{O_2}$$

$$\overleftarrow{v}_1 = \overleftarrow{k}_1 \times \theta_O^2 \times e^{\left(2\times(1-\alpha)\frac{g\theta_O}{RT}\right)}$$

$$\vec{v}_2 = \vec{k}_2 \times \theta_O \times e^{\left(-\alpha\frac{g\theta_O}{RT}+(1-\delta)\frac{g\theta_{O-H-OH}}{RT}\right)}$$

$$\overleftarrow{v}_2 = \overleftarrow{k}_2 \times \theta_{O-H-OH} \times e^{\left((1-\alpha)\frac{g\theta_O}{RT}-\delta\frac{g\theta_{O-H-OH}}{RT}\right)}$$

$$\vec{v}_3 = \vec{k}_3 \times \theta_{O-H-OH} \times e^{\left(\frac{-(1-\beta)F\Delta\Phi}{RT}\right)} \times e^{\left(-\delta\frac{g\theta_{O-H-OH}}{RT}+(1-\chi)\frac{g\theta_{O-H-OH^-}}{RT}\right)}$$

$$\overleftarrow{v}_3 = \overleftarrow{k}_3 \times \theta_{O-H-OH^-} \times e^{\left(\frac{\beta F\Delta\Phi}{RT}\right)} \times e^{\left(-\chi\frac{g\theta_{O-H-OH^-}}{RT}+(1-\delta)\frac{g\theta_{O-H-OH}}{RT}\right)}$$

$$\vec{v}_4 = \vec{k}_4 \times \theta_{O-H-OH^-} \times c_{H^+} \times e^{\left(-\chi\frac{g\theta_{O-H-OH^-}}{RT}+(1-\varepsilon)\frac{g\theta_{OH}}{RT}\right)}$$

$$\overleftarrow{v}_4 = \overleftarrow{k}_4 \times \theta_{OH}\, e^{\left((1-\chi)\frac{g\theta_{O-H-OH^-}}{RT}-\varepsilon\frac{g\theta_{OH}}{RT}\right)}$$

$$\vec{v}_5 = \vec{k}_5 \times \theta_{OH} \times c_{H^+} \times e^{\left(\frac{-(1-\gamma)F\Delta\Phi}{RT}\right)} \times e^{\left(-\varepsilon\frac{g\theta_{OH}}{RT}\right)}$$

where k is the kinetic constant, θ_x the surface coverage of the x species, β and γ the symmetry factors for the charge transfer step 3) and 5), α, χ, δ, ε, the symmetry factors for the adsorption, g, an interaction lateral parameter.

If the Rate Determining Step (RDS) is the 1st one

$$i = F \times \vec{k}_1 \times p_{O_2}$$

$$\ln(i) = C + \ln\left(p_{O_2}\right)$$

$$\left(\frac{\partial\Delta\Phi}{\partial\ln i}\right)_{p_{O_2}} = \infty\,;\ \left(\frac{\partial\ln i}{\partial\ln p_{O_2}}\right) = 1;\ \left(\frac{\partial\ln i}{\partial(2.3pH)}\right) = 0$$

If the Rate Determining Step (RDS) is the 2nd one

$$i = F \times \vec{k}_2 \times \theta_O \times e^{\left(-\alpha \frac{g\theta_O}{RT} + (1-\delta)\frac{g\theta_{O-H-OH}}{RT}\right)}$$

$$\ln(i) = C + \ln(\theta_O) - \alpha \frac{g\theta_O}{RT} + (1-\delta)\frac{g\theta_{O-H-OH}}{RT}$$

$$\left(\frac{\partial \Delta\Phi}{\partial \ln i}\right)_{p_{O_2}} = \infty \, ; \left(\frac{\partial \ln i}{\partial \ln p_{O_2}}\right) = 0 \, ; \left(\frac{\partial \ln i}{\partial (2.3pH)}\right) = 0$$

If the Rate Determining Step (RDS) is the 3rd one

$$i = F \times \vec{k}_3 \times \theta_{O-H-OH} \times e^{\left(\frac{-(1-\beta)F\Delta\Phi}{RT}\right)} \times e^{\left(-\delta \frac{g\theta_{O-H-OH}}{RT} + (1-\chi)\frac{g\theta_{O-H-OH^-}}{RT}\right)}$$

$$\ln(i) = C + \ln(\theta_{O-H-OH}) - \frac{(1-\beta)F\Delta\Phi}{RT} - \delta \frac{g\theta_{O-H-OH}}{RT} + (1-\chi)\frac{g\theta_{O-H-OH^-}}{RT}$$

$$\left(\frac{\partial \Delta\Phi}{\partial \ln i}\right)_{p_{O_2}} = -\frac{RT}{(1-\beta)F} \, ; \left(\frac{\partial \ln i}{\partial \ln p_{O_2}}\right) = 0 \, ; \left(\frac{\partial \ln i}{\partial (2.3pH)}\right) = 0$$

If the Rate Determining Step (RDS) is the 4th one

$$i = F \times \vec{k}_4 \times \theta_{O-H-OH^-} \times c_{H^+} \times e^{\left(-\chi \frac{g\theta_{O-H-OH^-}}{RT} + (1-\varepsilon)\frac{g\theta_{OH}}{RT}\right)}$$

$$\ln(i) = C + \ln(\theta_{O-H-OH^-}) + \ln(c_{H^+}) - \chi \frac{g\theta_{O-H-OH^-}}{RT} + (1-\varepsilon)\frac{g\theta_{OH}}{RT}$$

$$\left(\frac{\partial \Delta\Phi}{\partial \ln i}\right)_{p_{O_2}} = \infty \, ; \left(\frac{\partial \ln i}{\partial \ln p_{O_2}}\right) = 1 \, ; \left(\frac{\partial \ln i}{\partial (2.3pH)}\right) = 1$$

If the Rate Determining Step (RDS) is the 5th one

$$i = F \times \vec{k}_5 \times \theta_{OH} \times c_{H^+} \times e^{\left(\frac{-(1-\gamma)F\Delta\Phi}{RT}\right)} \times e^{\left(-\varepsilon \frac{g\theta_{OH}}{RT}\right)}$$

$$\ln(i) = C + \ln(\theta_{OH}) + \ln(c_{H^+}) - \frac{(1-\gamma)F\Delta\Phi}{RT} - \varepsilon \frac{g\theta_{OH}}{RT}$$

$$\left(\frac{\partial \Delta\Phi}{\partial \ln i}\right)_{p_{O_2}} = -\frac{RT}{(1-\gamma)F} \, ; \left(\frac{\partial \ln i}{\partial \ln p_{O_2}}\right) = 0 \, ; \left(\frac{\partial \ln i}{\partial (2.3pH)}\right) = 1$$

Tab. 1.1. Tafel Slopes for Damjanovich path.

	$\left(\frac{\partial \Delta \Phi}{\partial \ln i}\right)_{p_{O_2}}$		$\left(\frac{\partial \Delta \Phi}{\partial \ln i}\right)_{p_{O_2}}$
	Langmuir		Temkin
	$\theta \to 0$	$\theta \to 1$	
1) $O_2 \to 2O_{ads}$	∞	-	∞
2) $O_{ads} + H_2O \to (O - H - OH)_{ads}$	∞	∞	∞
3) $(O - H - OH)_{ads} + e^- \to (O - H - OH)^-_{ads}$	$\frac{RT}{(1-\beta)F}$	$\frac{RT}{(1-\beta)F}$	$\frac{RT}{(1-\beta)F}$
4) $(O - H - OH)^-_{ads} + H^+ \to OH_{ads} + H_2O$	$\frac{RT}{F}$	∞	∞
5) $OH_{ads} + e^- + H^+ \to H_2O$	$\frac{RT}{(2-\gamma)F}$	$\frac{RT}{(1-\gamma)F}$	$\frac{RT}{(1-\gamma)F}$

Experimental Tafel Slopes of polycrystalline platinum and Pt/C (see the following Tab. 1.2 and 1.3) are consistent with the Damjanovich's path, in which, for low overpotential, the rate determining step is the 4th, for low coverage, $\theta \to 0$, Langmuir-type isotherm, $\left(\frac{\partial \Delta \Phi}{\partial \ln i}\right)_{p_{O_2}} = \frac{RT}{F}$. For higher overpotential the rate determining step becomes the 5th step, a desorption-charge transfer step with intermediate coverage and a Temkin-type isotherm, $\left(\frac{\partial \Delta \Phi}{\partial \ln i}\right)_{p_{O_2}} = \frac{RT}{(1-\gamma)F}$.

1.3 Polycrystalline platinum

To set the experimental variables and to have a comparison with the literature, a set of data was recorded onto Pt-based materials: polycrystalline bulk electrode and commercial Pt nanoparticles dispersed onto high surface area carbon (Pt/C, Degussa EC20, 20 wt% Pt and Heraeus 40 wt% Pt).

Pt-H adsorption/desorption

A polycrystalline platinum electrode, i.e a rotating disk electrode (RDE) with a Pt tip embedded in a Teflon matrix, was preliminary characterized by cyclic voltammetry in nitrogen saturated solution. A representative voltammogram is reported in Fig. 1.1.

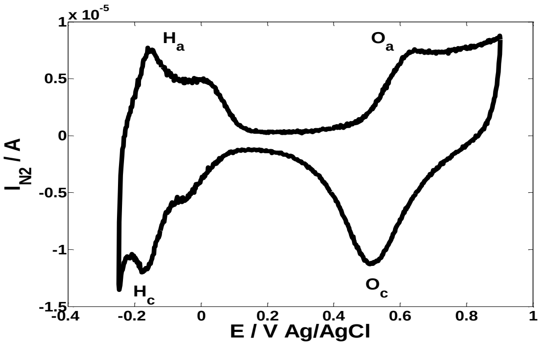

Fig. 1.1. Cyclic voltammogram at a smooth polycrystalline platinum electrode (0.04 cm^2 geometric area, N_2 saturated solution, 0.1 M $HClO_4$, 100 mV s^{-1}, T=25 °C). See text for details.

The shape of the voltammogram well reproduces the redox behavior of Pt in acidic solution reported in literature [1,2]. The potential scan starts at 0.9 V Ag/AgCl lower than oxygen evolution. Going cathodic, the reduction of oxide layer on the platinum surface takes place, with a cathodic peak, O_c, at ~ 0.55V. In the region between 0.13-0.24 V, only very small current is recorded: no Faradic reactions take place, and the current is due to double layer charge. At more negative potentials, the two peaks labelled H_c are due to formation of two types of adsorbed hydrogen at the platinum surface (Pt-H). Before reaching the net hydrogen evolution, the scan is changed to anodic direction, the peaks H_a in this case are due to oxidation of the two types of adsorbed hydrogen. After the double layer region formation of adsorbed oxygen, or platinum oxide layer, takes place, at peak O_a.

The peaks for hydrogen adsorption and desorption are symmetric and the voltammogram shape is independent of electrode rotation speed, indicating that the adsorption-desorption processes do not involve mass transport kinetic limitations.

The voltammograms in nitrogen saturated solution are useful to determine the presence of impurities in solution and the cleanliness of the platinum surface.

The electrochemical active surface area can be determined using the method reported in [3] that is described by reference to results in Fig. 1.1. By integration of experimental I/E curve, (Fig.1), an equivalent to an electric charge is obtained. The Coulumbic charge for hydrogen adsorption/desorption, Q_H, in the potential region between -0.2 and +0.1 V SCE is commonly attributed [3] to reduction/oxidation of Pt-H species requiring a single electron per Pt surface atom. By dimensional control of the relevant parameters one obtains:

$$Q = \frac{I\Delta V}{v} = [A \cdot V \cdot V^{-1} \cdot s] = [A \cdot s] = [C] \qquad (1)$$

Q=charge, [C].
v=scan potential rate, [V s^{-1}].
I=experimental current, [A].
ΔV=potential range, [V].

Therefore, by integrating the I/E profiles in the anodic H desorption and cathodic adsorption regions one obtains the total Q_H charge. Subtracting the capacitive area, in the same potential region and using 210 μC cm^{-2} as the charge related to Pt-H monolayer formation at a unit Pt surface area, the real Pt area is obtained. Due to the asymmetry between anodic and cathodic I/E profiles, which is apparent in Fig. 1.1, an average value is preferably obtained.

$$Q_H = \frac{(Q_0 - Q_{DL})}{2} \qquad (2)$$

Where Q_0 is the total charge (cathodic *and* anodic) in the hydrogen adsorption/desorption region and Q_{DL} is the capacitive charge from Pt double layer charging. The experimental value of Q_H is $1.4 \cdot 10^{-2}$ mC cm^{-2} that corresponds to a Pt surface area of 0.06 cm^2, against a geometrical surface area 0.04 cm^2. This difference can be compounded assuming a roughness factor of 0.06/0.04=1.5.

Oxygen Reduction Reaction (ORR)

Cyclic voltammograms of oxygen reduction onto a polycrystalline platinum rotating disk electrode are presented in Fig. 1.2. A set of curves are reported for increasing RDE rotation rates. The voltammograms can be divided in three parts (Fig. 1.2). In a first potential range (0.9-0.65 V Ag/AgCl) the current is zero and the oxygen reduction does not take place. Going more cathodic the current starts to increase with decreasing potential; this is a mixed control region (0.25<E<0.65 V Ag/AgCl) where electron charge transfer and reactant (O_2) mass transport occur at comparable rates. Decreasing further the potential, currents become potential independent; this is the limiting current region, where the reactant mass transport from the bulk solution to the electrode surface occurs through the Nernst diffusion layer and is the rate limiting step.

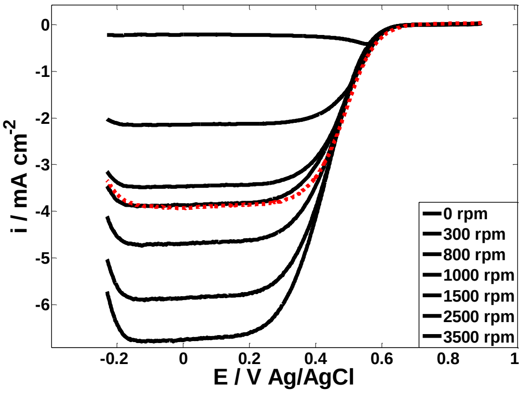

Fig. 1.2. Cathodic going O_2 reduction curves of cyclic voltammograms on smooth platinum electrode, in O_2 saturated solution at different RDE rotation rates. (0.04 cm^2 geometric area, 0.1 M $HClO_4$, 5 mV s^{-1}, T=25 °C). The red Dotted line is the anodic potential scan at 1000 rpm.

Hysteresis appears between the forward and backward potential scans (see Fig. 1.2 red dotted line), and is ascribed to a variable state of Pt surface oxide depending on the previous electrode potential history. Bearing in mind that the reaction rate is faster on oxide-free than oxide covered Pt surfaces, the hysteresis in nearly steady-state voltammograms may be attributed to the slowness of Pt oxide reduction.

The more interesting regions are the mixed control and limiting diffusion currents regions. Kinetic data can be obtained from these parts of the I/E curve (i=current density, i=I/surface area=[A cm^{-2}]), by means of the Koutecky-Levich equation in the mixed control region, and by the Levich equation in the limiting diffusion region, respectively. The equations are reported in the following.

The Levich equation reads:

$$I_L = 0.62 \cdot n \cdot F \cdot A \cdot D^{2/3} \cdot \nu^{-1/6} \cdot c_0 \cdot \omega^{1/2} \qquad (3)$$

where I_L is the experimental limiting current (A), n is the number of electrons to reduce a single O_2 molecule, F is the Faraday constant(96486.7 C mol^{-1}), A the geometric electrode area (cm^2), D the reactant diffusion coefficient in the bulk solution ($1.93 \cdot 10^{-5}$ cm^2 s^{-1}), ν is the kinematic solution viscosity (0.01 cm^2 s^{-1}), c the bulk reactant concentration ($1.22 \cdot 10^{-6}$ mol cm^3) and ω the electrode rotation rate (rad s^{-1}).

By this equation limiting current values of O_2 reduction at different rotation rates, for a given solution and electrode surface area can be calculated a priori.

The Koutecky-Levich equation is an implementation of the Levich equation and permits to extract kinetic current values from the experimental ones:

$$\frac{1}{i} = \frac{1}{i_{kin}} + \frac{1}{i_L} \qquad (4)$$

$$\frac{1}{i} = \frac{1}{i_{kin}} + \frac{1}{0.62 \cdot n \cdot F \cdot D^{2/3} \cdot \nu^{-1/6} \cdot c_0 \cdot \omega^{1/2}{}_L} \qquad (5)$$

i = experimental current density,
i_{kin} = kinetic current density,
i_L = diffusion limited current density through the diffusion layer thickness.

It is based on the assumption that reactant diffusion in solution, i_L, occurs in series with the following electron transfer step, i_{kin}. Using reciprocal coordinates permits to separate the kinetic and diffusion currents by extrapolation at infinite RDE rotation rate, where any contribution from diffusion becomes zero ($i_L \to \infty$).

Additionally determination of i_k at different E values allows real kinetic parameters, unaffected by reactant mass transport, to be obtained by combination of the Koutecky-Levich equation with the explicit Levich equation form. Plots of i^{-1} against $\omega^{-1/2}$ at given E are predicted to be linear with an intercept representing the kinetic current at E. Providing that the number of exchanged electron per unit reactant molecule, n, is a constant, these plots should be more over parallel; the slope in this case only depending on the mass transport parameters in the denominator of the second term on the right hand side of eq. (3), that are obviously constant in a given experimental conditions.

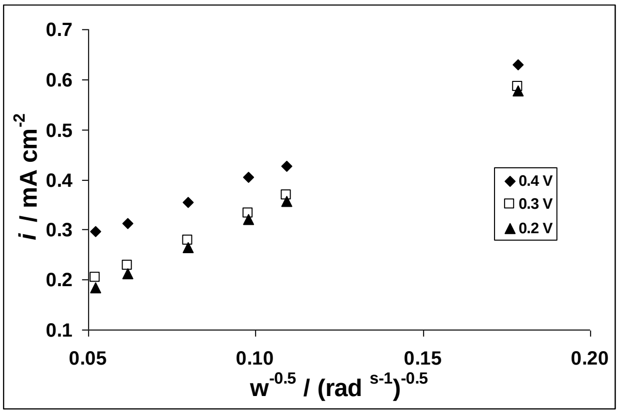

Fig. 1.3. Koutecky-Levich plot for O_2 reduction at Pt polycrystalline electrode for different electrode potentials. Data are from experimental voltammogram in Fig. 1.2 (cathodic sweep direction).

Koutecky-Levich lines, in Fig.1.3, are indeed characterized by a constant slope. This is a proof that the number of electron exchanged per O_2 molecules, *n*, is also a constant. By using the above reported parameters in the Levich equation, *n* is calculated at *n*=3.9, closely approaching the stoichiometry of *n*=4 so that:

$$O_2 + 4H^+ + 4e \rightarrow 2H_2O$$

This shows that , on Pt the parasitic reaction to H_2O_2 occurs by a small fraction yield:

$$O_2 + 2H^+ + 2e \rightarrow H_2O_2$$

When plotted in logarithmic form, i_k values at different potentials give rise to the usual Tafel plots, Fig. 1.4, in accordance with the Tafel equation:

$$\eta = a - b \log i \qquad (6)$$

Where η is the overpotential, *a* is a constant depending on the exchange current and *b* is a constant.

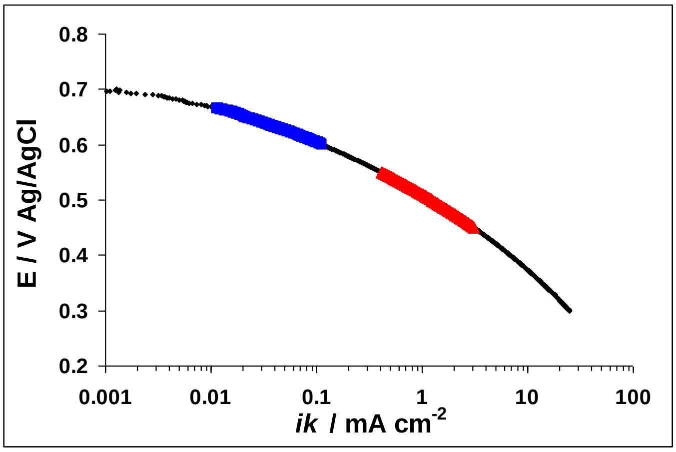

Fig. 1.4. Tafel plot for O_2 reduction on polycrystalline Pt. Color points evidence the linear regions where Tafel slopes have been determined.

The values of intercept and slope are in good agreement with literature data for polycrystalline Pt. Reference values from the literature are reported in Tab. 1.2.

Even though it is clear that the Tafel slope for the ORR is continuously changing with the potential [4-7], the experimental data fit two Tafel slope regions at low (62 mV dec^{-1}) and high (122 mV dec^{-1}) overpotentials, in accordance with calculated Tafel coefficients of 2.3RT/F and 2×2.3RT/F, respectively. These values are in good agreement with literature results for different forms of Pt metals (oriented single crystal [8] and polycrystalline [9]).

It can be also mentioned that the above results are not corrected from uncompensated ohmic drops which may contributed to the experimental curvature. This consideration holds for all other Tafel plots in the following.

The exchange current density value was determined extrapolating the current at $\eta=0$ in a plot η vs. log i_k.

Value of extrapolated exchange current was $i_{0=}$ 1.11×10^{-6} mA cm^{-2} that agree with data reported in literature of 10^{-6} mA cm^{-2} [10].

Tab. 1.2. Onset potential, low and high overpotential Tafel slopes and exchange current densities for polycrystalline Pt. Data from voltammograms in Fig. 1.2.

Onset potential E / V	Tafel Slope/mV dec^{-1} 0.675>E>0.600 V	Tafel Slope /mV dec^{-1} 0.550>E>0.400 V	i_0 mA cm^{-2}
This work: 0.7	62	122	1.1×10^{-6}
[4] 0.9 RHE	63	120	----

1.4 Platinum supported on high surface area carbons

1.4.1 RDE onto Pt/C

To increase the available surface area, and the output power of an operating fuel cell, Pt nanoparticles are usually dispersed onto an electronically conductive, low cost, high surface area material. These requirements are satisfied by carbon based materials like activated carbon and carbon black.

An investigation of O_2 reduction on dispersed platinum is interesting to fundamental and practical aspects. Dispersed Pt on high area carbon black is at present the reference electrocatalyst for acid fuel cells so that it is important to find out what supporting materials, Pt loading and catalyst preparation method are optimal for low cost and high efficiency catalysts.

The kinetic of oxygen reduction was examined on an ink type electrode made with a commercial platinum supported onto high area carbon, Pt/C, (E-Tek, EC20 20 wt% Pt and Heraeus 40 wt % Pt). The main difficulty in investigating supported catalyst is to obtain the intrinsic catalytic activity, unaffected by the many parameters involved in the overall electrode preparation and behavior, like, for instance, catalyst distribution, electrode thickness, porosity and uniformity. Electrode structure effects are most pronounced in thick gas diffusion electrode which are the electrodes used in fuel cells. As a fast screening tool of fuel cell catalysts, a technique was developed [4] that relies on the

RDE configuration, to control mass transport processes of soluble reactants to the electrode surface, and on the use of very thin catalyst layer such as to mimic a smooth, flat surface. Such electrodes are generally prepared depositing small volume of a catalyst suspension (ink) onto an electrochemically inert, conducting material, like glassy carbon. This technique (thin-film rotating disk electrode, TFRDE) is able to avoid, at least to some extent, many of the drawbacks of a real, porous, fuel cell electrode.

In all the electrodes mentioned above the efficiency depend on ink and electrode preparation. For this reason a correct experimental procedure and data elaboration is necessary.

As pointed out by Stamenkovic [17] there are some guidelines to compare high surface area supported Pt catalysts using the TFRDE:

1. Normalization of experimental data based on the Pt loading (catalyst mass activity) or surface area (specific activity).
2. For determination of mass activity the complete utilization of the catalyst is mandatory. The electrochemical active area has to be linearly dependent on catalyst loading. The electrochemical active area has to be evaluated by applying a proper method that also take into account the Faradic capacity of the carbon support.
3. For a correct data analysis the electrode thickness of thin-layer electrodes has to be lower than ~10.0 µm, that is comparable to Nernst diffusion layer thickness in the solution.
4. Diffusion limited currents for ORR has to be within 10% of theoretical Levich values.
5. The current at any potential of interest has to be within 10% and 80% of the diffusion limited current.

To set the experimental conditions necessary to obtain reliable data on supported Pt/C catalysts without exceeding the above theoretical limitations a preliminary study was performed.

The first point in the above list, is the normalization procedure, which is necessary to compare different electrodes and catalysts. Normalization using the Pt mass is not easily performed because the tiny Pt amounts thus can only be calculated by approximation from the used ink volumes in the range of few µl's, thus introducing a too high and not evaluable error.

An alternative normalization procedure might be based on the electrochemical active area obtained from H adsorption/desorption data. This is not considered appropriate when limiting currents are involved because, in these conditions, the active area is the geometrical one and such areas are representative of the overall Pt surface even if the relevant particles are buried deep in the electrode layer, while limiting current, by definition, only depends on the outermost exposed hydrodynamic geometrical area. This holds as for as the electrode rugosity is smaller than the diffusion layer, thickness ~10 µm. Nevertheless, H-adsorption/desorption data are available to access the amount of supported Pt, permitting comparison of different electrodes. Normalization for the electroactive area and Pt amount are used with other purpose in the following.

Stated otherwise the rate of electron transfer far from limiting conditions, depends on the surface sites available for reactant adsorption and therefore on the overall, also internal, catalyst surface area and therefore which might be related to the H adsorption/desorption data. However when limiting currents are approached at high overpotentials, the internal catalyst surface is excluded from external reactant supply and current become again controlled by the external surface area and by mass transport across a laminar diffusion layer in solution which coincide with electrode external surface area.

For the above reason normalization of curves on geometrical electrode area was performed. This normalization is based on a complete, uniform coverage of the inert tip by the deposited catalyst with a thickness smaller than the diffusion layer. The electrode coverage can be evaluated by voltammograms in nitrogen saturated solution where the charge underlying the voltammograms is proportional to the amount of catalyst deposited and by the theoretical limiting current value (4th point of the list above) determined by the Levich equation. This double check, electrochemical active area and Levich limiting current was used to evaluated effects of catalyst layer and Nafion film thickness.

In this study the electrode was prepared depositing a small amount of Pt/C suspension onto a glassy carbon rotating-disk tip. Nafion was used to bind the supported platinum at the disk surface.

To verify the second point of the list above different amounts of EC20 were deposited onto the electrode to obtain electrodes with different amount of catalysts. Since Pt concentration in the Pt/C is constant (20wt%), increase amount of Pt deposited means to increase electrode thickness.

Characterization by H- adsorption/desorption

Characterization by cyclic voltammetry in nitrogen saturated solution was performed as in case of smooth Pt electrode, Fig. 1.6.

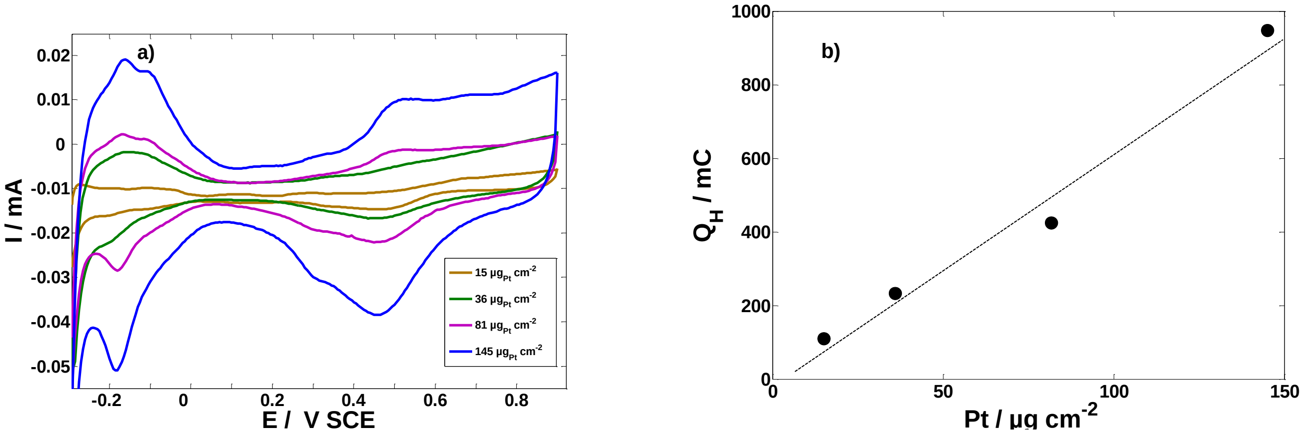

Fig. 1.6. a) Cyclic voltammograms of Pt/C electrode at different Pt loading. Electrode geometric area 0.07 cm^2, N_2 saturated solution. $HClO_4$ 0.1 M, 5 mV s^{-1}, T=25°C.
b) Hydrogen desorption charge as function of amount of Pt/C deposited onto the electrode.

The peaks of voltammogram in nitrogen saturated solution for Pt/C have the same morphology of massive Pt. Current peaks for hydrogen and oxygen adsorption/desorption are present but they are not sharp as on smooth Pt electrode. Currents in Fig. 1.6a increase with the increasing of platinum loading onto the glassy carbon tip. Values of hydrogen adsorption/desorption charge values have been determined by integration of the relevant areas. As reported in Fig. 1.6b the charge varies by a good linear relation to the amount of Pt deposited onto the tip: this behavior indicates that in deaerated solution the overall Pt surface is equally accessible by reacting protons and linearly increases with increasing Pt amount or Pt/C. This satisfies the second point of the list above: the electroactive area is a linear function of Pt loading.

As for polycrystalline Pt, the electroactive Pt area of Pt/C can be calculated assuming a Pt-H adsorption stoichiometry, to the exclusion of H interactions with carbon.

Diffusion limited ORR on Pt/C

This section mainly focuses on the behavior of limiting currents to establish reliable criteria for RDE usage.

The onset potential for oxygen reduction on Pt/C is E~0.67 V Ag/AgCl, very near to the value of massive platinum.

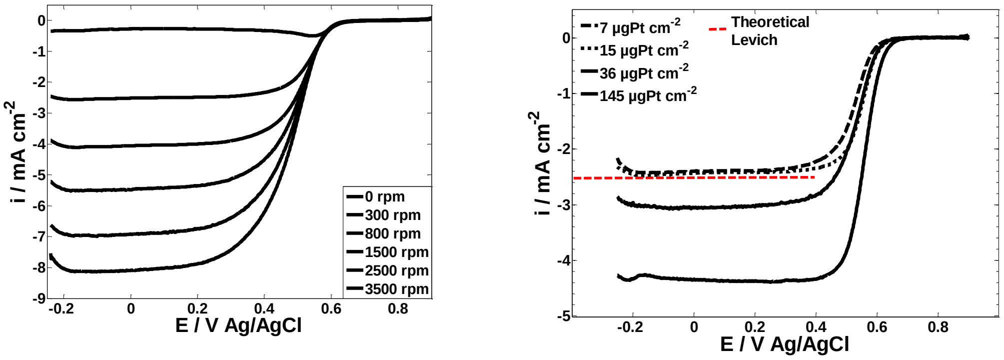

Fig. 1.7.a) Cathodic curves of cyclic voltammograms of Pt/C in O_2 saturated solution at different rotation rates 15 µgPt cm^{-2}, 0.07 cm^2 geometric area.
b) Cathodic curves at different Pt loading, O_2 saturated solution 300 rpm, 0.07 cm^2 geometric area.
(0.1 M $HClO_4$, 5 mV s^{-1}, T=25°C).

The recorded ORR current increases as a function of both electrode rotation rate and Pt loading, Fig. 1.7a and Fig. 1.7b respectively. Even if limiting currents are normalized on the Pt amount (or Pt electroactive surface area, from Fig.1.8a), they still differ for different Pt loading. This suggest that Pt inside the catalyst layer contributes to oxygen reduction, also in external diffusion limited conditions.

In this latter figure, ORR limiting currents are seen to increase with increasing Pt/C loading. This occurs in spite of the use of limiting currents normalized on the geometrical surface area. Moreover, in the same figure the limiting Levich current density is at first approached for comparatively low Pt/C loading and then largely exceeded with increasing loading. This data are comparable with those reported in literature [11] for Pt supported electrode with different thickness. The above trend of behavior is made more systematic on Fig. 1.8a and Fig. 1.8b. In the first case, limiting currents are shown to increase non linearly with increasing catalyst loading. A more extensive set of $i_L/\omega^{1/2}$ data is plotted in Fig. 1.8b using Levich coordinates and are seen again to approach from below the theoretical Levich slope for low Pt/C loading and to exceed this limit at higher thickness even if a good linear relation is still obtained. No ready explanation can be proposed for such anomalous behavior other than noticing that controlling the geometrical electrode area was found gradually more difficult when using thick Pt/C suspension, so larger areas than the geometrical one may be involved.

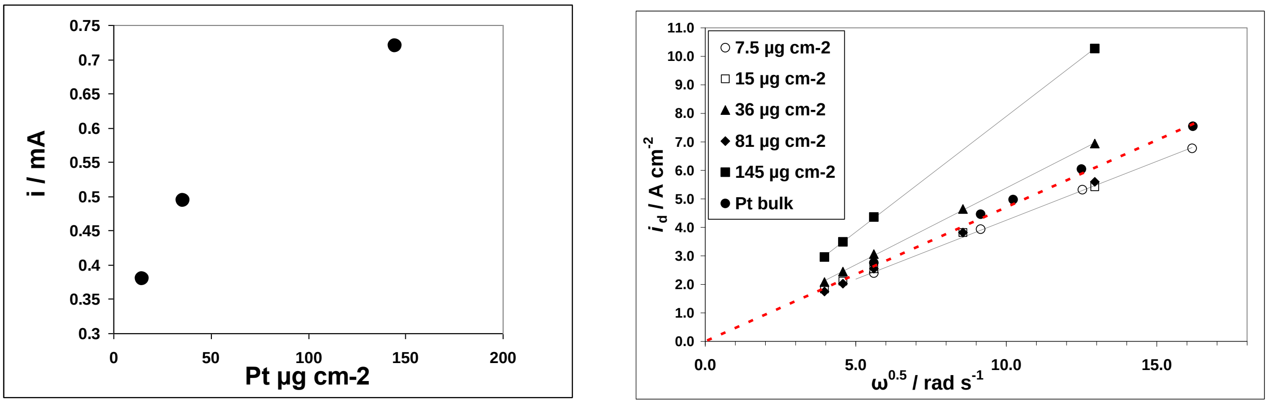

Fig. 1.8. a) Limiting ORR currents, at different Pt loading, corrected for the background,. b) Effect of increasing Pt loading (see legend). Nafion film thickness=0.08 µm, 300 rpm. The theoretical Levich line is reported for the used geometrical surface area.

Other explanations are reported in the literature. In [11,12], pronounced changes in Pt utilization, electrode activity and ORR kinetics have been observed varying the catalyst layer thickness. In such study thicker film electrodes exhibit higher Pt utilization efficiency and higher activity, it is proposed that Pt surfaces may support electron charge transfer when not in contact with the electrolyte by surface diffusion (spillover), of oxygen or oxygen containing species, OH and O [12,13]. This explanation may be part of the picture however it should be noted that increasing catalysts layer thickness may make invalid the Levich treatment by which the catalyst layer must be thinner than the Nernst diffusion layer, Fig. 1.8b

This section outlines some criteria that have to be obeyed to obtain reliable RDE results on supported Pt/C electrodes:

1. Pt catalyst amounts must be reproducibly controlled. This is achieved by means of the overall Pt-H adsorption/desorption charge which is insensitive of electrode layer thickness,

2. ORR limiting current densities must conform to the Levich model, where the geometrical electrode area is adopted as current normalization factor,

3. Thickness of supported Pt/C catalyst must be as thin as feasible, provided on almost complete coverage of the glassy carbon tip is achieved, in order that hydrodynamic RDE conditions are not perturbed.

Kinetics for ORR

Currents in the mixed control region were elaborated by means of the Koutecky-Levich equation, to evidence real kinetic currents free from diffusion mass transport and to obtain Tafel like plots, E/log*i*, Fig. 1.9

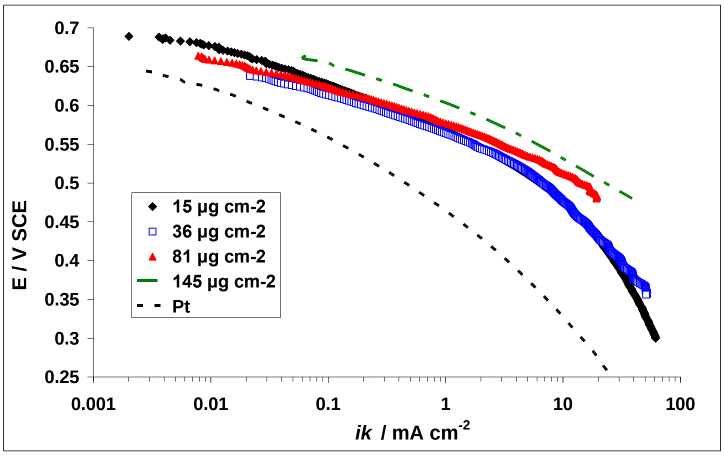

Fig. 1.9. Tafel plot for O_2 reduction Pt/C at different electrode thickness. In the potential range E=0.67-0.6 V the slope is ≈60 mV dec^{-1}, in the range E=0.55-0.45 V is ≈120 mV dec^{-1}.

In Fig. 1.9 Tafel plots recorded for Pt loading ranging 15-81 µg cm^{-2} are closely superposable and are therefore unaffected by electrode thickness. The Thicker electrode (145 µg cm^{-2}, green dotted line) deviates from the behavior with a Tafel plot that at any potential is shifted to greater currents, which is likely due to greater rugosity or porosity factors related to electrode preparation.

Kinetic parameters from Tafel plots are reported in Tab. 1.3 and are comparable with ones obtained for a smooth Pt electrode.

Tab. 1.3. Kinetic parameters for ORR at different catalyst thickness for Pt/C electrodes. Nafion film thickness=0.08 µm. LCD=low current density region, HCD=high current density region.

Thickness µm	LCD mV SCE	Tafel slope mV dec^{-1}	i_0×10^{-6} mA cm^{-2}	HCD mV SCE	Tafel slope mV dec^{-1}	i_0×10^{-8} mA cm^{-2}
7	640-550	60	1.1	510-430	119	2.1
36	600-530	57	1.2	530-430	130	2.9
145	590-550	67	11.6	540-500	87	25.0

Effect of Nafion overlayers

This section deals with one of the literature methods adopted to bind Pt/C powders onto the RDE glassy carbon tip. In this method a small volume of Pt/C suspension in water is pipetted onto the RDE tip. After drying, aliquots of commercial Nafion solution are successively added.

The following effects are observed with increasing total Nafion deposited amounts. These effects differ from similar ones recorded by directly mixing Pt/C powders and Nafion, as shown in the next section.

In rotating disk electrode experiments, Nafion is used to bind the catalyst powder to the rotating electrode by covering film formation. The effect of these additional layer was evaluated varying its thickness by subsequent addition.

On the top of the dried Pt/C catalyst layer a Nafion layer was coated. Experiments were performed onto a 15 μg cm^{-2} electrode. The Nafion film thickness was calculated by Eq. 11.

$$L = \frac{V \times d \times C_N}{d_N \times A \times 100} \tag{11}$$

L = Nafion film thickness (cm);
V = volume of Nafion solution coated on the catalyst layer (cm^3);
d = density of Nafion solution (0.874 g cm^{-3});
C_N = weight percent of Nafion in the solution (2%);
d_N = density of dried Nafion (2 g cm^{-3});
A = projected surface area of the glassy carbon electrode (0.07 cm^{-2});

To obtained the figure results, Nafion aliquots were added in successive working days onto the same Pt/C layer. Nominal Nafion thickness are calculated by Eq. (11) and vary in the range 0.26-1.05 µm, see figure legend.

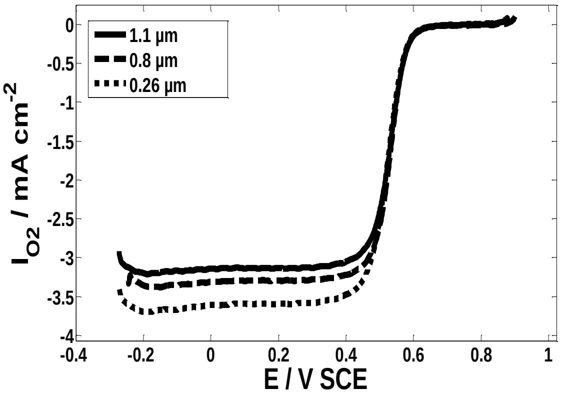

Fig. 1.10. ORR curves (cathodic scan) at different Nafion thickness on Pt/C in O_2 saturated solution, 0.07 cm^2 electrode geometric area (15µg Pt, 300 rpm, 0.1 M $HClO_4$, 5 mV s^{-1}, T=25 °C).

Oxygen reduction starts at about 0.65 V SCE, constant, and limiting currents are reached for every film thickness at about 0.4 V SCE. Limiting currents decrease with increasing Nafion thickness. As reported in the literature for both bulk Pt disk [14] and Pt/C supported catalysts [15] the decrease in ORR current is attributed to an O_2 mass transport resistance across the Nafion film. Accordingly the polymer film behaves as a second barrier for mass transport in addition to the Nernst diffusion layer of dissolved oxygen to the electrode surface. Therefore limiting currents should depend on film thickness, decreasing with increasing thickness, as observed experimentally in Fig. 1.10 and Fig. 1.11 in which increasing Nafion thickness causes an increasing curvature of $i/\omega^{1/2}$ plots.

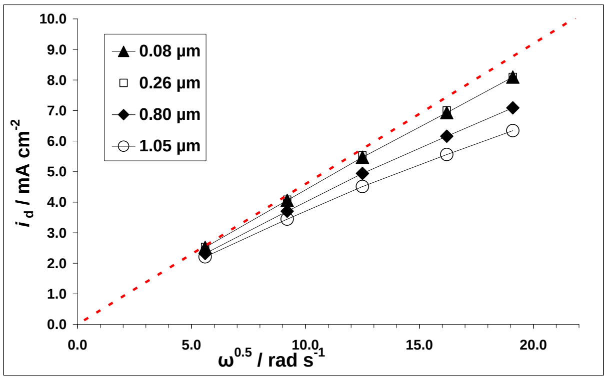

Fig. 1.11. Effect of Nafion film thickness over the catalyst layer. Pt=15 µg cm^{-2}.

This data are in good agreement with literature data [16-18].

The kinetic parameters for oxygen reduction with increasing film thickness were determined by means of Koutecky-Levich equation. The real kinetic currents are not affected by Nafion thickness, as shown by the close superposition of logi/E plots for E>0.45 V, and film thickness effects occurs at lower potentials introducing an additional hindrance to the extrapolated currents. This latter effect is the only contribution from the Nafion film, results are shown in Fig.1.12.

The additional mass transport process through the Nafion layer is represented in the Koutecky-Levich equation as internal mass transport process because it takes place in the electrode.

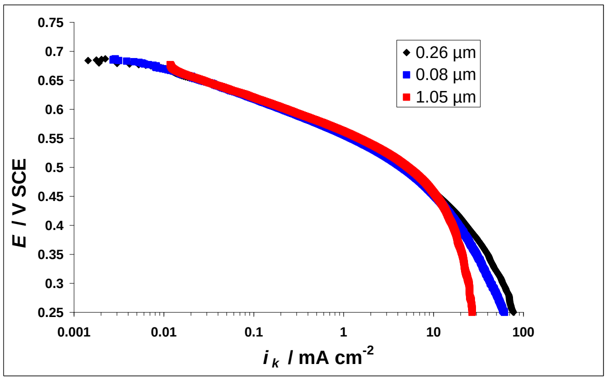

Fig. 1.12. logi/E results in logarithmic coordinates (Tafel plots) for different Nafion thickness as in the legend.

Tab. 1.4 reports data elaboration of Fig.1.12. The non dependence of kinetic parameters on Nafion thickness is apparent.

Tab. 1.4. Kinetic parameters for ORR at different Nafion film thickness for Pt/C electrodes. Pt =15 μg cm^{-2}.

Thickness μm	LCD mV SCE	Tafel slope mV dec^{-1}	i_0×10^{-6} mA cm^{-2}	HCD mV SCE	Tafel slope mV dec^{-1}	i_0×10^{-8} mA cm^{-2}
0.08	650-450	57	1.1	530-450	118	5.3
0.26	650-450	60	1.2	530-450	115	7.5
1.05	650-450	57	1.1	530-450	130	3.6

Results reported in Tab. 1.4 and 1.3 for increasing Nafion thickness and also Pt loading are comparable thus excluding effect of these parameters on the orr current/potential behavior.

As shown in the Tafel plot (Fig. 1.8 and 1.12) the Tafel slopes changes continuously with increasing potential. However experimental data could be safely plotted by two Tafel slopes at low and high potentials, respectively. This is in accordance with literature data; the above independence of Pt/C and Nafion film thickness is again confirmed.

1.4.2 Nafion as catalyst binder

Besides being deposited as a catalyst overlayer, Nafion can also be dispersed within the porous catalyst structure to extend the three dimensional reaction zone [20], see Fig. 1.13, and to minimize ohmic and mass transport limitations. In this case a different electrode preparation is adopted: catalyst powder and Nafion are mixed together and deposited onto the glassy carbon disk thus avoiding the formation of a separate Nafion film on the electrode structure. The relative Nafion/Catalyst ratio (N/C) becomes an experimental variable.

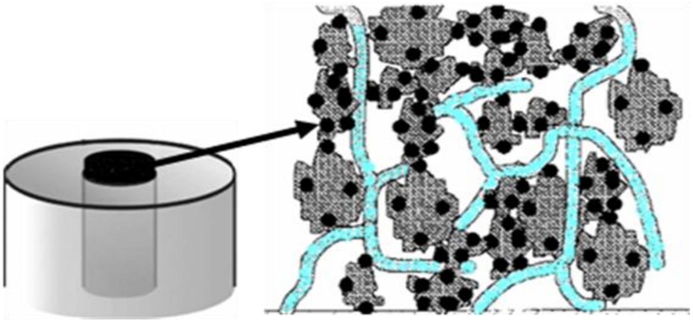

Fig. 1.13. Schematic representation of Nafion inside the catalyst layer.

The influence of Nafion ionomer on the oxygen reduction properties of Pt/C catalysts was investigated by means of a rotating disk electrode (RDE) by changing the relative Nafion/Catalyst ratio (N/C=0.25-1.5).

N/C ratios were changed by varying the H_2O+Nafion total amount with respect to total solids (Nafion and Pt/C, Heraeus 40 wt%), in order to keep constant the catalyst amount per unit slurry ink volume. For instance, N/C=1.0 was obtained suspending 0.1 g catalyst in 1.5 g H_2O added with 0.67 g of the Nafion suspension (15 wt%). After component mixing, the resulting suspension was mechanically stirred 48 hours. In this way the catalyst amount could be kept constant as well as the catalyst layers thickness by dosing constant ink volume, typically 10 µl which corresponds to a layer thickness of ~ 10 µm.

Well defined I/E relations were recorded in any case with Tafel slopes, that are presented below, vary in the range ~120 mV/current decade depending on potential, Fig. 1.13, and with limiting currents that, most relevant and contrary to results in the previous section, weakly increase with increasing N/C ratio, with a maximum at N/C=0.5.

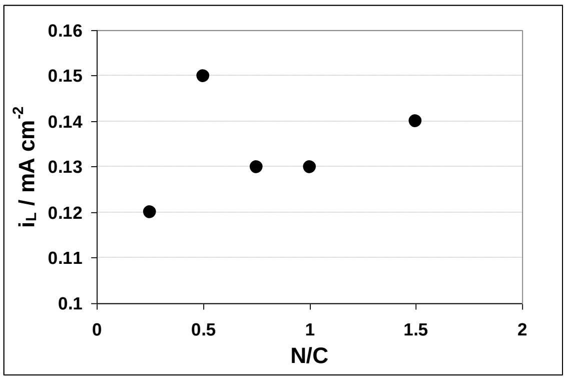

Fig. 1.13. Limiting current densities of Pt/C catalysts as a function of N/C (0.1 V SCE, 700 rpm).

Characterization by H- adsorption/desorption

Fig. 1.14 shows I/E curves from experimental CVs of Pt/C catalysts from the above preparation procedure, in N2 saturated solutions with different Nafion amounts.

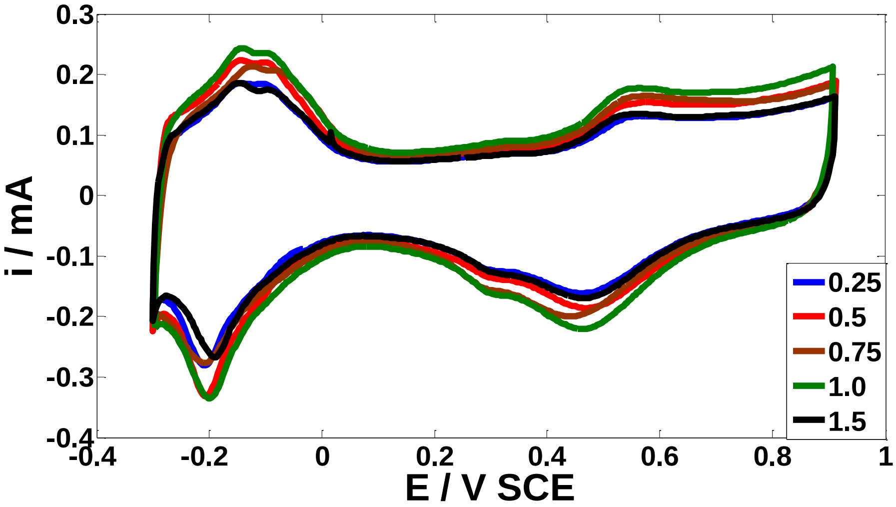

Fig. 1.14. CVs curves of Pt/C catalyst in N_2 saturated solutions. Currents are experimental values. (Pt 40 wt%,0.1M $HClO_4$, Tamb, 5 mV/s, 0 rpm).

The reported curves show the typical behavior of carbon-supported Pt catalysts ([1] and previous section) without any systematic variation in morphology that may safely be attribute to experimental variation of Nafion/Carbon and Nafion/Pt ratios. Thus, in the present conditions, Nafion does not apparently interfere with the energy distribution of hydrogen and oxygen adsorbing/desorbing Pt sites. Similarly, weak Nafion interactions also regard Pt-H charge values as calculated by I/E profile integration in the hydrogen adsorption/desorption region.

As shown in Fig. 1.15 these charge values slowly increase with increasing N/C, apparently reaching a quasi plateau value.

Surprisingly enough, Fig. 1.15 results in differ from similar ones in the literature [14, 19], where increasing Nafion causes a trend of decreasing hydrogen adsorption/desorption currents. Reasons for this difference are difficult to settle. However in [14, 19] Nafion was added in the last electrode preparation step, pipetting any necessary Nafion volume at the top of the catalyst layer already deposited at the RDE tip surface. However in the present case Nafion and Pt/Carbon catalyst were stirred a long time (48 h) permitting a homogeneous distribution of ionomer molecules within the internal porosity system and external surface of the solid catalyst, thus preventing Nafion from forming films with an increasing thickness, separating the catalyst from the electrolyte.

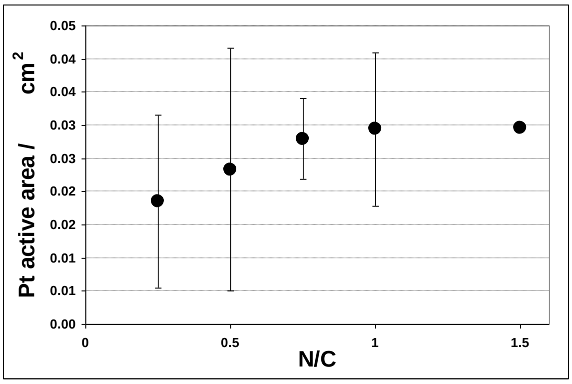

Fig. 1.15. Experimental charge for hydrogen adsorption/desorption of Pt/C catalysts as a function of Nafion content.

Oxygen reduction reaction

Fig. 1.16 shows I/E results recorded in O_2 saturated solution on Pt/C with different N/C ratios. Currents are normalized with respect to the projected electrode surface area. ORR onset potentials are ~0.72 V for all N/C ratios but for the somewhat higher value of N/C=1.5 (E~0.74 V).

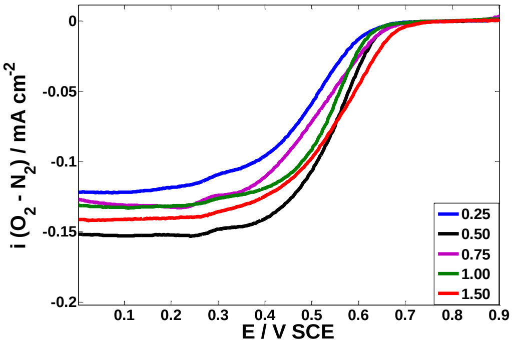

Fig. 1.16. Background-corrected ORR I/E relations of Pt/C catalyst at increasing N/C ratio. (0.1M HClO4, Tamb, 5 mV/s, 700 rpm).

ORR limiting currents reflect the overall Platinum utilization and, as already shown in Fig.1.13, depend on the Nafion content. In the first figure a first maximum occurs at N/C=0.5, followed by a slow increase (from N/C=0.75 to N/C=1.5) even though at lower current density values. This complex limiting current behavior can be reconciled with a number of factors among which variation of the Nafion ionomer contact with platinum nanoparticles and carbon, formation of more or less effective proton conducting networks. A further and most relevant effect may concern an increased O_2 solubility in Nafion with respect to aqueous electrolyte [29]. Variation of the local oxygen solubility and of oxygen diffusion coefficient can be considered meaningful

To obtain more insights on the overall ORR behavior a procedure was adopted relying on a sequence of elaboration steps of I/E results, as already described in section 1.3.1 for Pt/C with Nafion overlayer; the first one is based on the well established Koutecky-Levich equation (eq. 2-3, 1.2 “Oxygen Reduction Reaction”) permitting a separation of kinetic contributions due to diffusion in solution from any other kinetically slow reaction step, electron charge transfer included.

Background-corrected experimental ORR currents densities are plotted in Fig. 1.17 in the (i^{-1} vs. $\omega^{-0.5}$) format of the Koutecky-Levich equation.

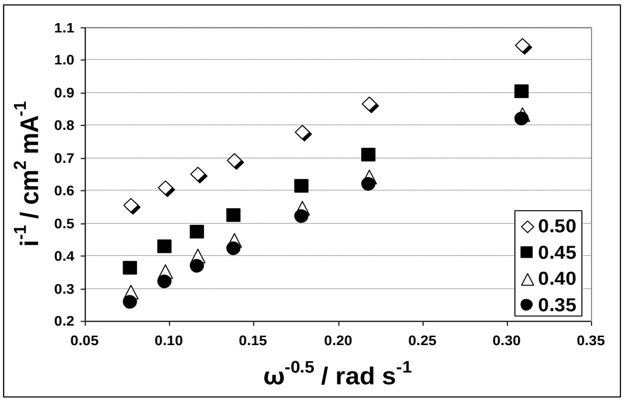

Fig. 1.17. Koutecky-Levich plot for O_2 reduction at various potentials in non limiting conditions (N/C=0.25, O_2 saturated 0.1 M $HClO_4$, Pt/C, Pt 40 wt%)

At any reported potential closely linear plots are obtained, except that at the highest used rotation rate (3000 rpm), with extrapolated (ω=∞) i^{-1} values that gradually increase with increasing electrode potential. On the form of the Koutecky-Levich, nearly superimposing lines are obtained with decreasing potential, in correspondence of the potential independent limiting currents region.

The above extrapolated (ω=∞) current densities are shown in Fig. 1.18 using Tafel coordinates.

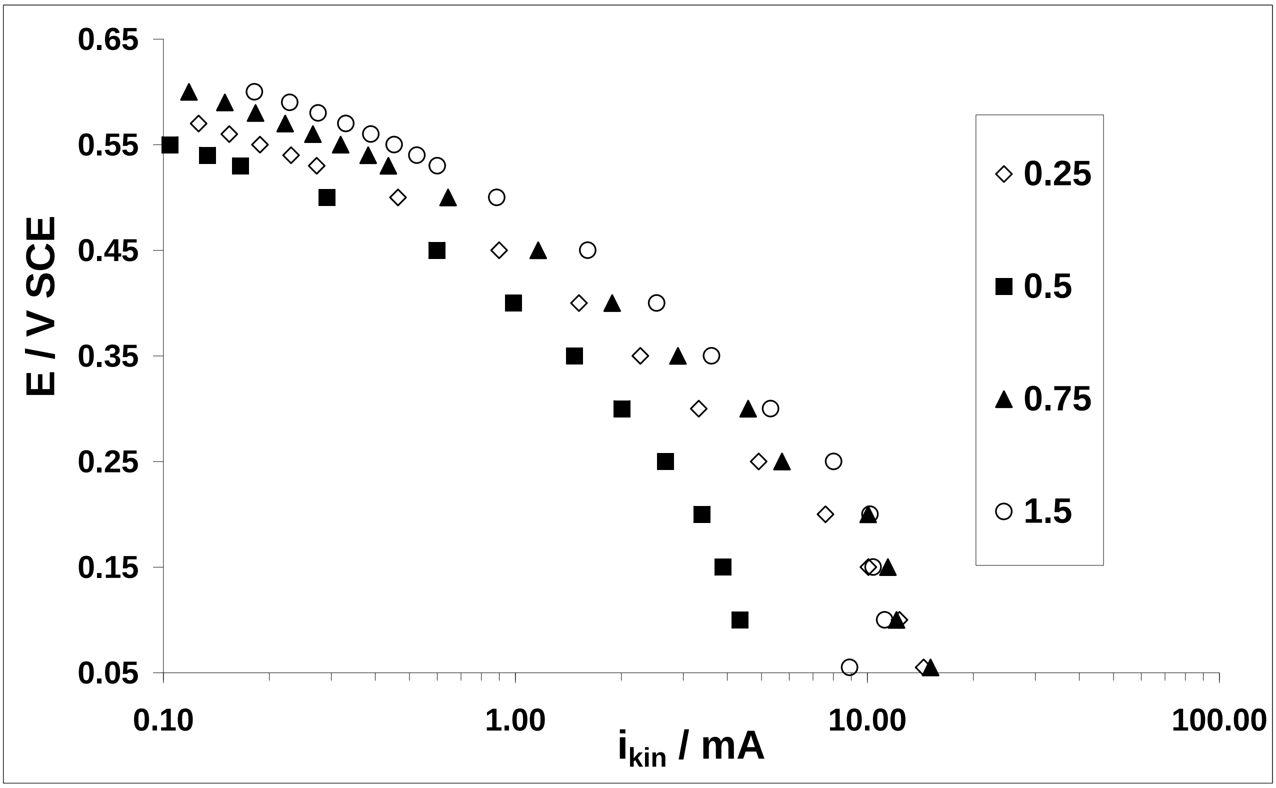

Fig. 1.18. Tafel plot for extrapolated kinetic current of Pt/C, 40 wt%, at different N/C ratio as in the legend.

Complex conditions apply in the figure, where the catalytic electrode response is actively modified by Nafion contents. Relatively good linear sections are observed in all cases, with Tafel slopes of ~60 and ~120 mV dec^{-1}, at high (E~0.65-0.55 V) and somewhat lower (E~0.50-0.35 V), potential respectively.

Effects from the Nafion content are also observed to variously shift one curve with respect to the other ones. By reference to the Tafel curve with the lowest N/C value (N/C=0.25), the curve with the second higher N/C (N/C=0.5) is shifted to more negative potentials and smaller currents, which might be attributed to Nafion screening effects of Pt active sites. However, for N/C=0.75 currents are shifted positive all over the potential range, also reaching maximal values at most negative potentials. The same behavior occurs for N/C=1.5 with most positive potentials in the low current region and, again, the maximum current density at the lowest potentials. Then, except for the inversion of N/C=0.25 and N/C=0.5 results, Nafion behaves as a promoter instead of an inhibitor of ORR.

In a further aspect, inspection of the figure shows that the overall morphology of logI/E plots is characterized by quasi potential-independent currents in the lowest potential region, which suggests that a further mass transport limitation occurs, differing from the one across the Nernst diffusion layer which given that this is already taken into account, and corrected for, by the Koutecky-Levich extrapolation procedure.

This further mass transport limitation step can only occur within the “solid” electrode thickness and is therefore kinetically connected in series with respect to the previous mass transport in solution and the following charge transfer at the catalyst surface.

The Koutecky-Levich equation (5) can be therefore modified as:

$$\frac{1}{i}=\frac{1}{i_{kin}}+\frac{1}{i_{L,\mathrm{int}}}+\frac{1}{i_L} \qquad (11)$$

i = experimental current density,
i_{kin} = charge transfer kinetic current density,
$i_{L,int}$ = diffusion limited current density through the catalyst layer thickness.
i_L = diffusion limited current density through the Nernst diffusion layer.

The second equation term, $i_{L,int}$, is the kinetic hindrance of the internal mass transport and is experimentally obtained as the maximum current at the most negative potentials of Fig. 1.18. Such values are separately shown in Fig. 1.19 as a function of N/C ratio.

By subtracting these $i_{L,int}$ values from each data point of the relevant logI/E plot in Fig. 1.18, real i_{kin} values are obtained and are reported in Tafel coordinates in Fig. 1.20, which is the final result of the above data elaboration.

Tafel slopes at high and low electrode potentials remain at essentially the above mentioned values (~60 and ~120 mV dec^{-1}), the second one extending down to the lowest potentials removing the masking effect of internal diffusion and providing further information on the kinetically slower charge transfer step.

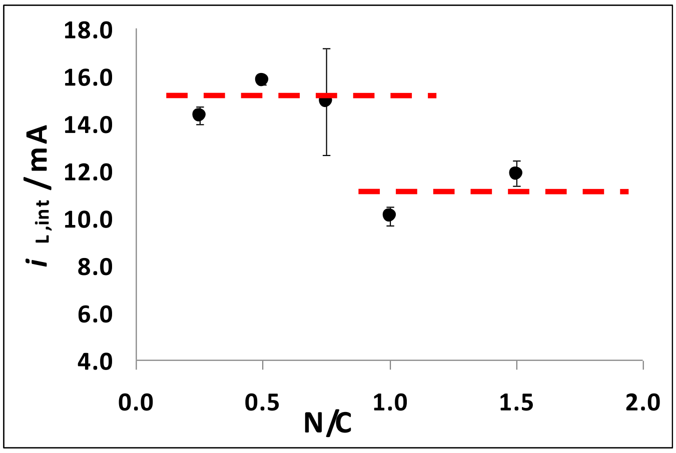

Fig. 1.19. Oxygen diffusion currents inside the catalyst layer as function of Nafion loading.

The internal diffusion limiting currents, $i_{L,int}$, are nearly the same from N/C=0.25 to N/C=0.75 with a small relative maximum at N/C=0.5. A sharp decrease, like a jump, occurs for N/C higher than 0.75. It may be proposed that Nafion causes two competing effects, the first one presumably taking place by increasing oxygen solubility within the “composite” electrode structure, the second one being instead a pore clogging mechanism that might prevail at high Nafion amounts [2].

The current decreases increasing the Nafion content indicates that the oxygen diffusion is favorited for Nafion concentration in the N/C ratio between 0.25 and 0.75. The small increase for N/C=1.5 could be due to non homogeneous dispersion of Nafion in the carbon structure that can partially clog the pores [2].

The real kinetic currents, i_{kin}, free from internal and external mass transport contributions, can be plotted in Tafel coordinates (Fig.1.20.).

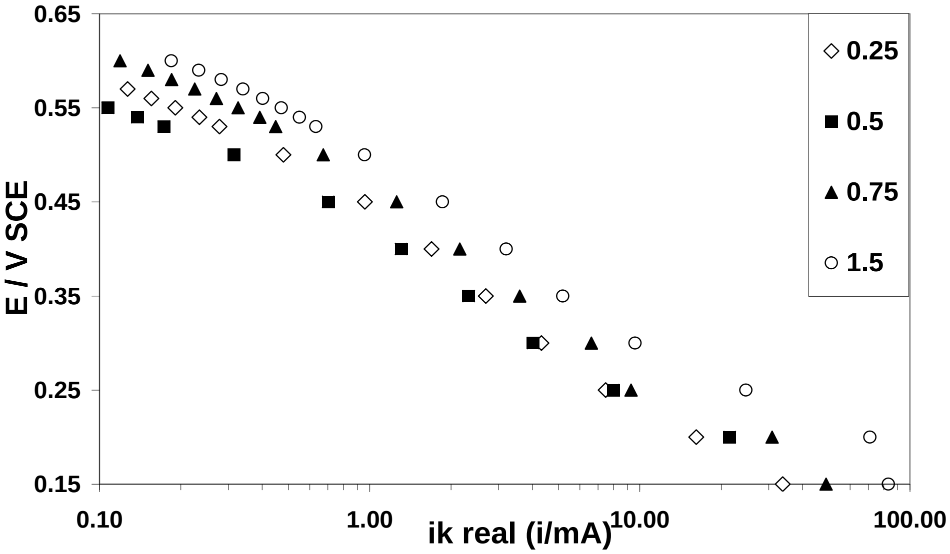

Fig. 1.20. Tafel plot for real kinetic current at different N/C ratio.

After this correction, the limiting current disappears and the Tafel slopes in the high overpotential region change in comparison with the uncorrected kinetic currents. In the low overpotential region the straight lines are not affected by the correction for internal diffusion.

The region with quasi potential-independent current, which in the above is attributed to internal diffusion, could also be interpreted as a linear Tafel region with infinite slope. This would be consistent with the 4th step of the Damjanovich mechanism with the electrode coverage near 1 in Langmuir adsorption conditions where $\left(\frac{\partial \Delta\Phi}{\partial \ln i}\right)_{p_{O_2}} = \infty$ applies (see Tab. 1.1, Section 1.2).

The above conclusion cannot be supported further by present results that only rely on Tafel plots obtained at constant proton concentration and oxygen pressure. However, in Fig. 1.21 after correction for the internal diffusion and neglecting the three points at the highest current densities, the potential independent current region at high overpotentials becomes linear with a slope of ≈120 mV dec^{-1} so that the rate determining step can still be considered the 5th step of the Damjanovich mechanism, Fig. 1.21.

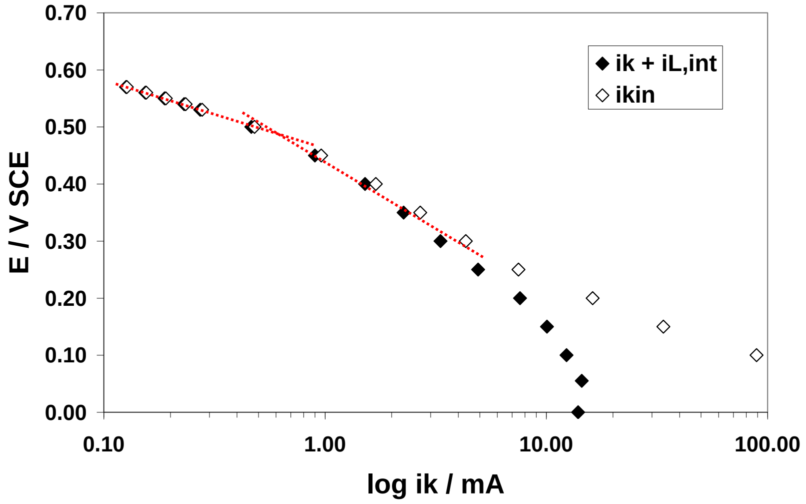

Fig. 1.21. Tafel plot before and after correction for the internal limiting current at N/C=0.25

1.4.3 Conclusions on Nafion effects

1. Comparison of results where Nafion was used as an overlayer (Section 1.3.1) and as a binder dispersed within the electrode structure shows that Nafion is not an inert electrode component with respect to ORR.
2. When used as an overlayer inhibition, screening, effects are dominating causing a limiting current decrease with increasing Nafion overlayer thickness.
3. When Nafion is adopted as an electrode binder, dispersing it into the catalyst slurry, ORR reaction promotion are evidenced at comparative low N/C. At higher concentration inhibition effects prevails as the above overlayer results.
4. Nafion is also active in modifying the kinetic charge transfer behavior which is, mainly, evidenced by the electrode potential shift towards more positive values shown in Fig. 1.20, after correction for external and internal diffusion processes.

References

[1] "*Electrochemical methods, Fundamentals and applications*", Allen J. Bard, Larry R. Faulkner, Wiley 1980, par. 12.6.

[2] "*Surface Electrochemistry, a Molecular Level Approach*", John O'M. Bockris, Shahed U. M. Khan, Plenum Press 1970, par.1.2.7.

[3] T.J. Schmidt, H.A. Gasteiger, G.D. Sta¨b, P.M. Urban, D.M. Kolb, R.J. Behm, *J. Electrochem. Soc.*, 145 (1998), 2354.

[4] N.M. Markovic, H.A. Gasteiger, P.N. Ross, *J. Electrochem. Soc.*, 144 (1997), 1591.

[5] F.A. Uribe, T.E. Springer, S. Gottesfeld, *J. Electrochem. Soc*,. 139 (1992), 765.

[6] C.F. Zinola, L. Castro, A.J. Arvia, *Electrochim. Acta*, 39, (1994), 1951.

[7] A. Parthasarathy, S. Srinivasan, A.J. Appleby, C.R. Martin, *J. Electrochem. Soc.*, 139 (1992), 2530.

[8] Grgur, N.M. Markovic, P.N. Ross, Jr., *Can. J. Chem.*, 75 (1997), 1465.

[9] A. Damjanovic, D.B. Sepa, *Electrochim. Acta*, 35 (1990), 1157.

[10] "*Modern Electrochemistry*", John O'M. Bockris, Amulya K. N. Reddy, A Plenum/Rosetta Edition, 1973, par. 10.4.4.

[11] J. Jiang, Baolian Yi, *J. Electroanal. Chem.*, 577 (2005), 107.

[12] J. McBreen, *J. Electrochem. Soc.*, 132 (1985), 1112.

[13] W. Tu, W. Liu, C. Cha, B. Wu, *Electrochim. Acta*, 43 (1998), 3731.

[14] M. Watanabe, H. Igarashi, K. Yoshioka, *Electrochim. Acta*, 40 (1995), 329.

[15] U.A. Paulus, T. J. Schmidt, H. A. Gasteiger, R. J. Behm, *J. Electroanal. Chem.*, 75 (1997), 1465.

[16] E. Higuchi, H. Uchida, M. Watanabe, *J. Electroanal. Chem*, 583 (2005), 69.

[17] K.J.J. Mayrhofer a, D. Strmcnik, B.B. Blizanac, V. Stamenkovic, M. Arenz, N.M. Markovic, *Electrochim. Acta*, 53 (2008), 3181.

[18] S. K. Zecevic, J. S. Wainright, M. H. Litt, S. Lj. Gojkovic, R. F. Savinell, *J. Electrochem. Soc.*, 144 (1997), 2973.

[19] A. Ohma, K. Fushinobu, K. Okazaki, *Electrochim. Acta*, 55 (2010), 8829.

[20] A. Hayashi, H. Notsu, K. Kimijima, J. Miyamoto, I. Yagi, *Electrochem. Acta*, 53 (2008), 6177.

[21] Y-H. Shih, G.V.S, .D. L., *J. Phys. Chem. C*, 112 (2008), 123.

[22] A. Damjanovic, V. Brusic, *Electrochim. Acta*, 12 (1967), 615.

[23] D.B. Sepa, V. Vojnovic, A. Damjanovic, *Electrochim. Acta*, 26 (1981), 781.

[24] O. Antoine, Y. Bultel, R. Durand, *J. of Electroanal. Chem.*, 499 (2001), 85.

[25] A. Damjanovic, V Brusic, *Electrochim. Acta*, 12 (1967), 615.

[26] "*Modern Aspects of Electrochemistry*", J. Bockris, B. E. Conway, Butterworth, London (1969),Vol.5, pag. 369

[27] B. V. Tilak, S. Venkatesh, S. K. J. Rangarajan, Electrochem. Soc., 136 (1989), 1977.

[28] J. O. M. Bockris, S. Srinivasan, "Fuel Cells: Their Electrochemistry"; McGraw-Hill: New York, 1969.

[29] V. A. Sethuraman1, S. Khan, J. S. Jur, A. T. Haug, J. W. Weidner, Electrochim Acta, 54 (2009), 6850.

Platinum-Free Catalysts

2.1 Introduction

Polymer Electrolyte Membrane Fuel Cells (PEMFCs) are at present recognized as energy efficient, clean energy converting devices. However, they are not yet commercially available because two main technical gaps limit their commercialization: cost and reliability. Currently, the slow kinetic of Oxygen Reduction at the cathode electrode is catalyzed by platinum nanoparticles supported onto carbon-based materials. To reduce PEMFC cost, in the short-term it is necessary to decrease the amount of Pt; in the long-term non-noble metal catalysts would be a better solution.

Disadvantages of Pt-based catalysts

Even if platinum is the best catalyst for oxygen reduction the difference of open circuit or low-current density electrode potentials with respect to the thermodynamic value are large [1].

This potential difference arises from polarization losses at the oxygen electrode. On the contrary, in a fuel cell the hydrogen electrode operates in near reversible conditions. At low current densities power losses are about 20-30% of the theoretical value and become higher under practical conditions. To improve fuel cell power output it is necessary to develop new catalysts for oxygen reduction. For that reason studies of oxygen reduction at various electrodes is an important research topic worldwide.

In the present technology noble metal based catalysts, like supported Pt-nanoparticles, are the most active, reliable catalysts for fuel cell application. However, additionally to cost other drawbacks are involved in their usage:

On Pt-based catalysts ORR does not exclusively proceed by the 4-electron mechanism but also involves the 2-electron process with hydrogen peroxide production. This 2-electron process reduces the system efficiency and the product peroxide can degrade the catalyst, decreasing its activity, but also other FC components, like carbon support and proton exchange membrane, resulting in FC degradation and even failure. To improve the overall FC efficiency a material that selectively promotes the 4-electron reaction is necessary.

Another issue related to Pt-based catalysts is that Pt is very sensitive to contaminants possibly present in the gas stream like CO, NH_3, NO_x, SO_x and organic compounds. Platinum poisoning would result in lower FC performance and degradation.

Non-noble metal catalysts

Active non-noble metal catalyst for ORR in acid medium can be classified [2] in (i) inorganic and (ii) molecular or molecular-derived catalysts. Only a few inorganic non-noble metal catalysts are available for ORR in acidic medium, with however poor activity. Chalcogenides, nitrides and oxides have been investigated. The second class contains nitrogen doped systems. Research in this direction was introduced by Jasinski who discovered that cobalt phthalocyanines catalyze ORR in basic medium [3]. Later, it was found that phthalocyanine and other Metal-N_4 chelates are also ORR active in acid medium. An important improvement for such systems was the discovery that high temperature treatment (400-1000 °C) of Metal-N_4 under inert gas flow increases catalyst stability and activity [4-6]. Since Metal-N_4 chelates decompose at such high temperatures the nature of the active sites has been, and still is, a subject of controversy [5,7]. Another important improvement was the synthesis of non noble metal catalysts without metal-N_4 chelates as precursor. Gupta et al. [8] experimentally demonstrated that the simultaneous presence of nitrogen, carbon and metal is necessary to induce ORR activity in nitrogen-doped catalysts. Materials from high temperature pyrolysis (T=800 °C) of polyacrylonitrile added with Co(II) or Fe(II) were used. The next step was to demonstrate that a transition metal, nitrogen and carbon can be introduced separately during pyrolysis by means of a gaseous nitrogen source (i.e. CH_3CN or NH_3) [9].

Since 1990s, many research groups have synthesized nitrogen doped carbon material using a single, or several, heat treatment steps, metal complexes or salts mixed with nitrogen compounds (polymers, NH_3 or CH_3CN) as the nitrogen source and with carbon black, polymers or organic molecules as the carbon source.

Along this line, in the present work a set of nitrogen doped carbons were obtained by grafting nitrogen containing compounds (amines, diamines and nitrogen based polymers) onto activated carbon and carbon black that were subsequently high temperature-treated in inert or reducing atmosphere. This latter step is crucial to exploit ORR catalytic behaviour.

In the first synthesis adopted nitrogen-grafting procedure, aliphatic amines were condensed in stoichiometric amounts onto the already existing acidic carbon surface groups. In a second variation of this procedure an aromatic amine, *o*-phenylenediamine, was at first condensed on carbon as before and then polymerized with excess amine still present in the solvent.

In a second synthesis procedure much greater amine amounts were used to behave as solvent and reactant, largely in excess of the acidic carbon groups.

Other materials were synthesised by carbonisation of appropriate precursors, e.g. glucose/histidine mixtures added with Fe and Cu salts, in the presence of silica gels as a hard templating agent to increase the available product surface area.

2.2 Commercial carbon modification and ORR

2.2.1 Stoichiometric amination of activated carbons

To synthesise amine doped carbon an effective route is to take advantage of carboxylic groups that are normally present at the carbon surface, reacting them with terminal aliphatic amine compounds (di-, tri-amine) such as to anchor a single amine group by amide bonding to the carbon surface, leaving the second one free to react further [10]. The synthesis procedure is briefly outlined: carbon powder was suspended under stirring in diglyme and added with a large di-amine excess with respect to the total amount of acidic groups separately determined by Boehm titrations. The suspension was heated at 145 °C to promote amidic condensation by water elimination.

Reaction conditions are reported in detail in the Experimental Section.

This synthesis was performed using different carbon substrates, both activated carbon and carbon black, using a set of amino compound. Two metals were separately used: iron and cobalt. The synthesized materials are reported in Tab. 2.1.

Tab. 2.1. Synthesized carbon based materials and, in brackets, the abbreviation adopted in the following.

Carbon Support	Amine	Metal Ion 2 wt%	Pyrolysis Temperature
Darco KB-G, activated carbon, (DG)	1,6-hexamethylenediamine (D6)	Fe, Co	700-900 °C
	Diethylenetriamine (DETA)	Fe, Co	700-900 °C
	o-phenilenediamine (*o*-phen)	Fe, Co	700-900 °C
	Poly *o*-phenilenediamine (P *o*-phen)	Fe, Co	700-900 °C
FW200, carbon black (FW)	1,6-hexamethylenediamine	Fe, Co	700-900 °C
	Diethylenetriamine	Fe, Co	700-900 °C

End carbon products are specified by the abbreviation of the carbon support followed by that of the used amine, by the chemical symbol of any added metal and by pyrolysis temperature. For example, the abbreviation FW DETA Co 700 stands for the carbon black substrate FW200, reacted with diethylenetriamine, loaded with cobalt and finally pyrolyzed at 700 °C. Similarly, the abbreviation FW 700 indicates the same carbon black pyrolyzed at 700 °C, without amine and metal added.

The synthesized materials were characterized by Rotating Disk Electrode (RDE) technique, to obtain kinetic parameters for Oxygen Reduction Reaction (ORR), Membrane Electrolyte Assembly (MEA) and physical techniques like BET, XRD and XPS.

RDE intrinsic redox behaviour

The study of electrochemical behaviour of carbon based materials must focus on the carbon electrode/electrolyte interface, where the surface structure and functional groups of carbon play an important role. A study of surface carbon modification was performed combining cyclic voltammetry, Boehm titrations, EDX, XRD, XPS and SEM analysis (see section 2.3.1).

The intrinsic redox behaviour of carbon materials was evaluated by cyclic voltammetry in nitrogen saturated solution, to exclude charge transfer reactions of foreign reactants.

As reported in Fig. 2.1a, the I/E profile of an unmodified carbon (DG) involves very low currents without any defined peak.

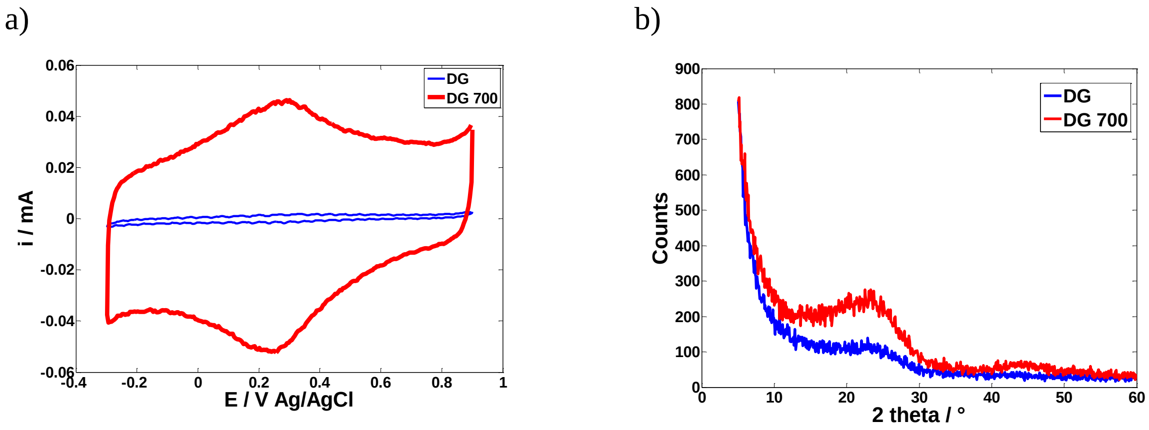

Fig. 2.1. a) Cyclic voltammograms of carbon support DG. (Electrode geometric area 0.07 cm^2, N_2 saturated solution, 0 rpm, 0.1 M $HClO_4$, 5 mV s^{-1}, T=25 °C).
b) XRD data of pristine and pyrolyzed (700 °C, N_2 atmosphere), activated carbon support.
Electrode geometric area 0.196 cm^2, N_2 saturated solution, 1600 rpm, 0.1 M $HClO_4$, 5 mV s^{-1}, T=25 °C.

After high temperature activation this same carbon gives rise to a completely different pattern with much higher currents and, moreover, with two related anodic and cathodic peaks, at ~0.25 V, showing the presence of a redox system due to oxidation/reduction of surface groups, possibly quinone-hydroquinone surface sites [11,12].

Pyrolysis in inert atmosphere also strongly changes the carbon XRD pattern (Fig. 2.1b) with a well defined increase of the (002) reflection due to thermally induced carbon graphitization.

The high temperature-dependent current increase in Fig. 2.1a is meaningful of an increase of the electrochemical active area. However, BET measurements show that the N_2 accessible surface area actually decreases upon thermal treatment (Tab. 2.2) related to a partial collapse of the internal porosity structure.

Then, electrochemical and gas adsorption measurements give a different estimate of accessible samples area.

Tab. 2.2. Pyrolyzed material B.E.T. surface area.

Carbon sample	B.E.T. surface area
DG	1615 $m^2\ g^{-1}$
DG 700	1137 $m^2\ g^{-1}$

Because of this evidence, surface areas of the many investigated carbon samples were measured “in situ” integrating CV pattern areas, like that in Fig. 2.1a. As already mentioned for supported Pt/C catalyst, CV pattern areas are meaningful of the electrical charge necessary to change the double layer potential within experimentally chosen limits.

In Fig. 2.2a a comparison of the above I/E CV patterns with a third one recorded after amine treatment of the same carbon with DETA in diglyme followed by thermal treatment at 700 °C.

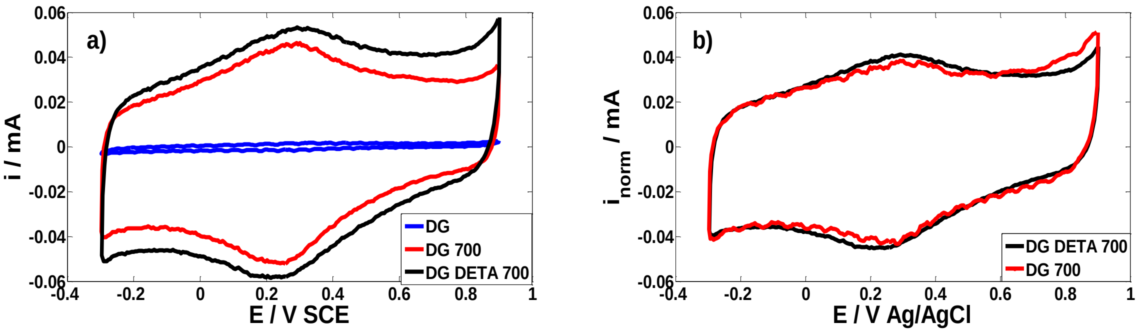

Fig. 2.2a. Experimental CV currents of DG carbon at different modification stages: untreated (blue line); pyrolyzed (red line); after DETA amination followed by pyrolysis (black line).
Fig. 2.2b. Normalization of the two latter CV results on a common electrochemical area.
Electrode geometrical area: 0.07 cm^2, N_2 saturated solution, 0 rpm, 0.1 M $HClO_4$, 5 mV s^{-1}, T=25 °C.

The overall pattern shape is essentially that of the amine-untreated sample with however greater currents all over the potential range. Even though the used thermal treatment is the same, the surface amine presence and thermal reactions cause an increase of the electrochemically active area.

Then, to compare carbon materials from different preparations, some surface area normalization procedure had to be adopted. Charge values were measured by integration of CV patterns and compared with the similar charge of a given carbon sample, adopted as an internal, though arbitrary reference (see Fig. 2.2a and 2b).

Results of this normalization are shown in Fig. 2.2b as comparison of the above amine treated and untreated samples. A good superposition of CV patterns is observed with a normalization factor of 1.29 (pyrolyzed DETA-treated/untreated ratio).

An increase of electrochemical active electrode area was anyway observed after carbon amination and metal loading, satisfactorily taken into account by the above normalization procedure. Fig. 2.3 shows normalized CVs carbon metal loading with Fe and Co.

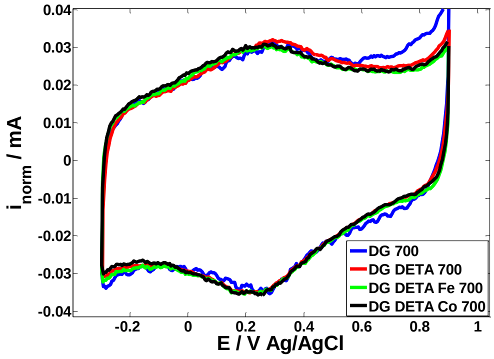

Fig. 2.3. Comparison of normalized i/E curves for aminated and metal loaded DG samples after pyrolysis. No changes in the intrinsic redox behavior is observed. Electrode geometric area 0.07 cm^2, N_2 saturated solution, 0 rpm, 0.1 M $HClO_4$, 5 mV s^{-1}, T=25 °C.

In a more general assessment, as shown normalization factors in Tab. 2.3, amine treatment and metal loading only affect the relative electrode area that in all cases increases with respect to the chosen DG 700 reference substrate.

Tab. 2.3. Normalization results of DETA treated DG with and without added metal.

Sample	Area	Charge	Normalization factor
	A V	C	
DG	$1.81 \cdot 10^{-6}$	$3.61 \cdot 10^{-4}$	0.06
DG 700	$2.84 \cdot 10^{-5}$	$5.00 \cdot 10^{-3}$	1.00
DG DETA	$3.66 \cdot 10^{-5}$	$7.31 \cdot 10^{-3}$	1.29
DG DETA Fe	$3.79 \cdot 10^{-5}$	$7.59 \cdot 10^{-3}$	1.34
DG DETA Co	$5.06 \cdot 10^{-5}$	$1.01 \cdot 10^{-2}$	1.78

It is rather surprising that the above treatments do not affect the quinone/hydroquinone redox system which is intrinsic to the materials, the more so also taking into account that, as shown in the following, strong changes in ORR activity ensue from these treatments

The same synthesis was adopted using a carbon black support (Degussa FW200). CV results in nitrogen saturated solution are reported in Fig. 2.4 and evidence a very similar redox behavior with, however, less well developed intrinsic peaks of the quinone/hydroquinone system.

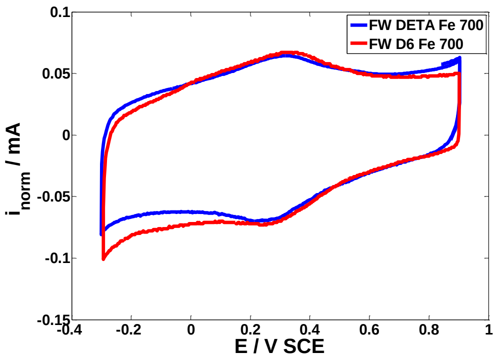

Fig. 2.4. Normalized E/i curves for aminated and metal loaded carbon black FW after pyrolysis. Electrode geometric area 0.196 cm^2, N_2 saturated solution, 1600 rpm, 0.1 M $HClO_4$, 5 mV s^{-1}, T=25 °C.

The same intrinsic redox behaviour was found for pyrolyzed DG at first modified by *o*-phenylendiamine grafting in low temperature conditions, followed by polymerization of excess amine with $(NH_4)_2S_2O_8$. The synthesis procedure is reported in the Experimental Section.

Amine bonding causes a first decrease of experimental BET surface area, followed by a further, stronger one after amine polymerisation (Tab. 2.4).

Tab. 2.4. BET surface areas of pristine DG, o-phenylendiamine-treated DG (DG *o-phen*), and polymerised o-phenylendiamine DG (DG P *o-phen*).

Carbon sample	BET surface area
DG	1616 m^2 g^{-1}
DG *o*-phen	1278 m^2 g^{-1}
DG P *o*-phen	650 m^2 g^{-1}

Elaboration of BET results shows that the surface area decrease is due to an overall pore volume decrease regardless of pore size, with surface-bound *o*-phenylendiamine behaving as a non-specific cover of the exposed surface (Fig. 2.5a). In spite of this, after polymerisation, pores smaller than 6 nm increase in relative volume (Fig. 2.5b). Then, in this instance, a second pore system apparently develops within the supported polymer chains, at the smallest experimentally detected pore size range.

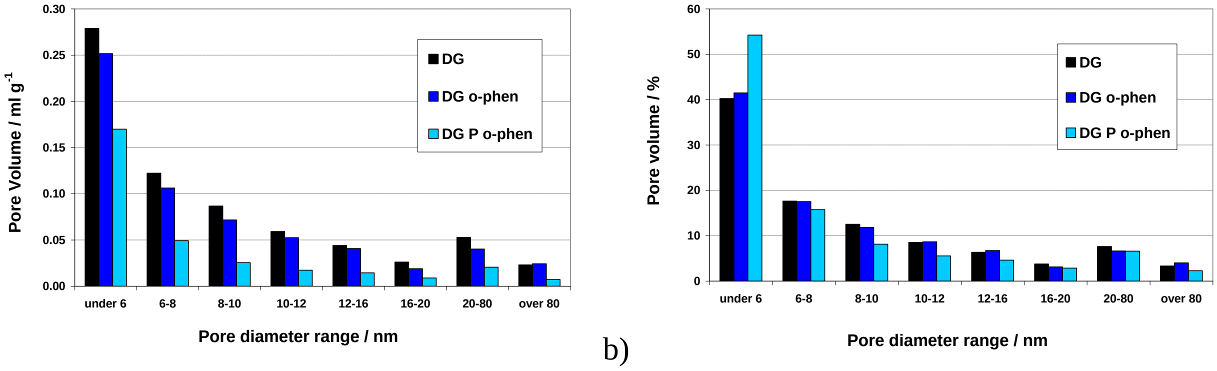

a)

b)

Fig. 2.5. Pore volume distribution (a) in ml/g and (b) percent after o-phenylendiamine anchoring and subsequent polymerisation.

Voltammetric results show that pyrolysis and metal loading of these aminated materials retain the intrinsic redox behaviour of DG 700 substrate (Fig. 2.6) with, however, somewhat less developed quinone/hydroquinone peaks.

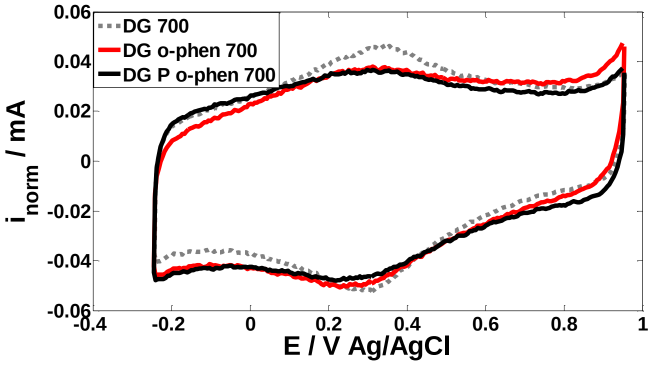

Fig. 2.6. CVs of DG, DG *o*-phen, DG P *o*-phen, after pyrolysis at 700 °C in N_2 saturated solution (N_2 saturated solution, 1600 rpm, 0.1 M $HClO_4$, 5 mV s^{-1}, T=25 °C).

RDE oxygen reduction reaction

The synthesized materials were tested for ORR activity using the rotating disk electrode (RDE) technique, as already used for Pt/C, to evaluate the different reactants and modification procedures. As shown in Fig. 2.7, heat treatment improves ORR catalytic activity of even otherwise untreated samples, giving rise to higher currents and more positive incipient oxygen reduction potentials with respect to the same thermally untreated carbon.

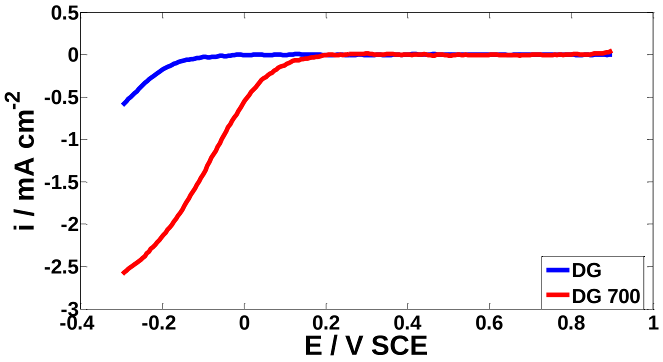

Fig. 2.7. CV for O_2 reduction on pristine and high temperature activated DG carbon in O_2 saturated solution (0.07 cm^2 geometric area, 0.1 M $HClO_4$, 5 mV s^{-1}, T=25 °C, 1600 rpm).

Fig. 2.8 refers to a DG sample that was preliminarily acid-washed in a Soxhlet apparatus to remove possibly present contaminants. As shown by Bohem titrations (see section 2.4.1 and Experimental Section), acid washing changes the relative abundance of carbon surface groups, increasing the acidic groups at the expense of the basic ones. It was therefore felt interesting to asses if such variation might also correspond to changing ORR responses. As reported by the comparison in Fig.

2.8 of acid and base treated DG samples this actually occurs, with the ORR activity of an acid treated sample displaced at higher currents and potentials with respect to the basic one.

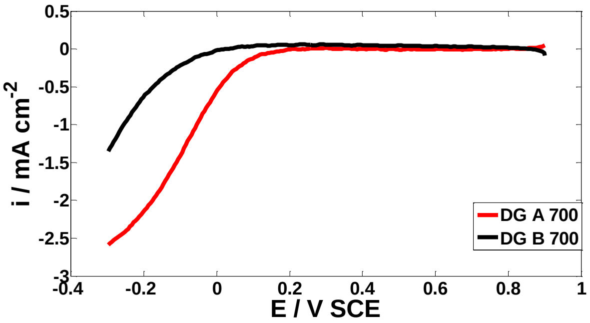

Fig. 2.8. i/E curves for DG-A (acid washed sample) and DG-B (basic washed), both of them pyrolyzed at 700 °C. (0.1 M HClO$_4$, O$_2$ saturated solution, 1600 rpm, 5 mV s^{-1}, T=25 °C).

Further ORR improvements were obtained by amination and metal loading (Fig. 2.9).

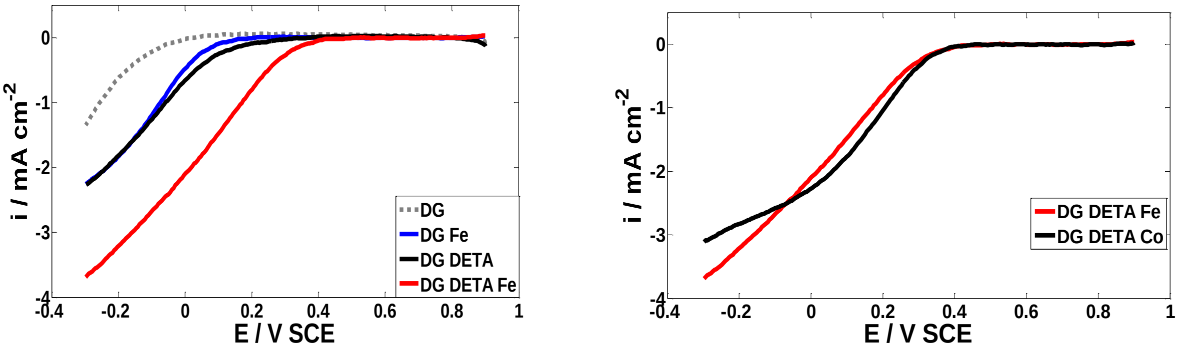

Fig. 2.9a. E/i curves for DG-B (basic washed samples) at different synthesis stages as specified in the figure legend.
Fig. 2.9b. Comparison of Fe and Co loading.
All samples were pyrolyzed at 700 °C (0.1 M HClO$_4$, O$_2$ saturated solution, 1600 rpm, 5 mV s^{-1}, T=25 °C).

Fig. 2.9a reports the effects of each synthesis step on the ORR catalytic activity. Fe loading shifts the ORR onset potential somewhat positive of ~0.1 V and also causes a current increase (see the blue curve). The catalytic activity remains however poor. Also, DETA amination alone does not increase the catalytic activity (black line). When amine and metal ions are both present during pyrolysis a strong increase in current and a more positive potential shift (~0.4 V) are recorded. This confirms that the contemporary presence of a carbon support, a nitrogen precursor and metal ions is necessary to achieve some catalytic activity for this kind of materials.
Similar results were obtained when Co was substitute for Fe, Fig. 2.9b.

To increase nitrogen content in precursor carbon before pyrolysis, amination and polymerization with *o*-phenylenediamine was tried (see the Experimental Section). Amine grafting followed by polymerization do not improve significantly ORR results (Fig. 2.10, blue and black lines). Metal loading (Fe, Co) is necessary to shift positive the ORR onset potential at about 0.45 V/AgCl (red and magenta lines).

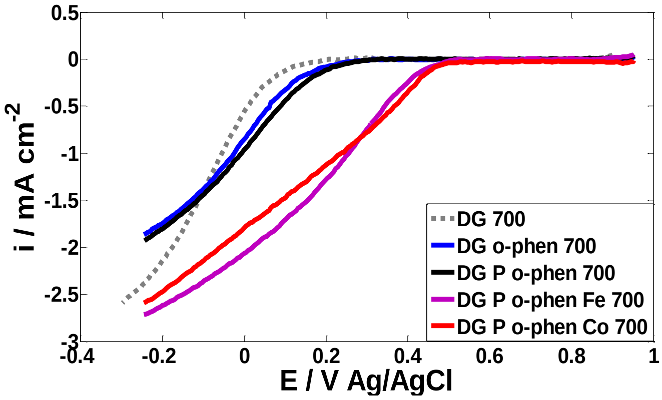

Fig. 2.10. E/i curves for DG-A (acid washed carbon) at different synthesis stages as specified in the figure legend. All samples were pyrolyzed at 700 °C. (0.1 M $HClO_4$, O_2 saturated solution, 1600 rpm, 5 mV s^{-1}, T=25 °C).

Similar conditions and ORR results occur using FW instead of DG carbon as a support. Fig. 2.11 reports the relevant i/E voltammograms.

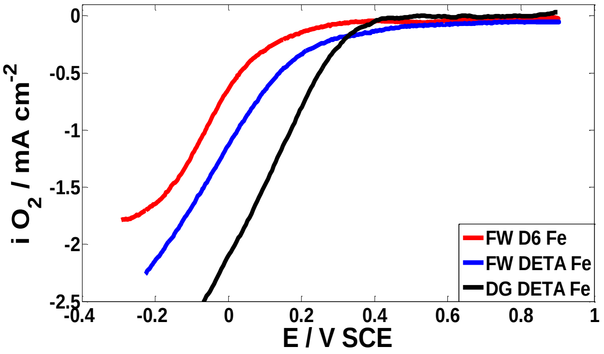

Fig. 2.11. E/i curves for FW 200 and DG carbon pyrolyzed at 700 °C. Amine compounds: hexamethylenediamine, red curve; diethylenetriamine, blue curve; diethylenetriamine. (0.1 M $HClO_4$, O_2 saturated solution, 1600 rpm, 5 mV s^{-1}, T=25 °C).

FW 200 carbon black affords end samples with poor catalytic activity, lower than that of DG activated carbon (see the black and blue curves in Fig. 2.11). Substituting Co for Fe on in this DETA aminated carbon black does not increase ORR catalytic activity (not reported results).

2.2.2 Carbon Flooding Synthesis

Attempts to improve ORR activity were performed by means of a second synthesis procedure, based on the idea of completely wetting a precursor carbon surface, the internal porosity system included, by reactive amine compounds. Briefly, this synthesis involves suspending a carbon substrate in a liquid amine such that it behaves as both a reactant and solvent, calculating the relative carbon and amine amounts to completely flood the internal carbon pore volume. Three commercially available carbon blacks (Degussa FW 200, XPB 334 and its oxidized version, XPB 390) were used suspending them in DETA which is liquid at room temperature. Chosen metal ions (Fe, Co) were dissolved in amine in 5 wt% with respect to carbon. Small propanol amounts were used as dispersing agent. Other details are reported in the Experimental Section.

Some variations in pyrolysis conditions were performed using different temperatures (700 and 900 °C) and flowing gas composition (Ar or H_2/N_2, 1/9).

The obtained materials are reported in Tab. 2.5.

Tab. 2.5. Synthesized samples, synthesis conditions and, in brackets, the abbreviation adopted in the following.

Carbon Support	**Amine**	**Metal Ion 5 wt%**	**Pyrolysis Temperature °C**	**Pyrolysis gas flow**
FW 200 (FW)	Diethylenetriamine (DETA)	Fe, Co	700-900	Ar, H_2/N_2
XPB 334 (334)	Diethylenetriamine (DETA)	Co	900	Ar
XPB 390, (390)	Diethylenetriamine (DETA)	Co	900	Ar

The samples nomenclature is as in the above omitting in this case the amine compound that is a constant. For example, the abbreviation FWf Co 700 is for: FW 200 loaded with DETA, added with Co and pyrolyzed at 700 °C in argon gas flow. The abbreviation FWf Co 700 H is for the same sample pyrolyzed in flowing H_2/N_2.

The synthesized materials were characterized by Rotating Disk Electrode (RDE) and by a single fuel cell by Membrane Electrolyte Assembly (MEA) technique, to obtain kinetic parameters for Oxygen Reduction Reaction (ORR).

RDE intrinsic redox behaviour

The intrinsic redox behaviour in nitrogen saturated solution is scarcely affected by heating temperature and gas flow composition, Fig. 2.12, as for the synthesis in diglyme onto activated carbon, see Fig. 2.2b.

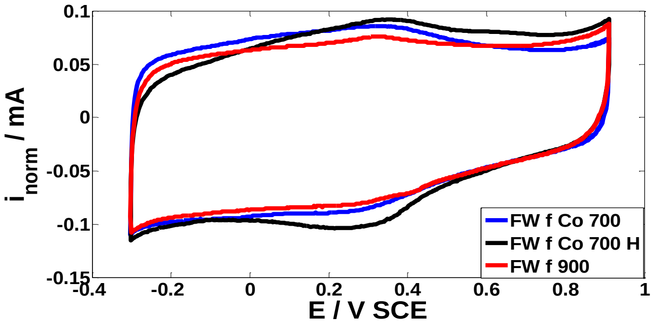

Fig. 2.12. Normalized i/E results of different samples from FW f carbon support. (Electrode geometric area 0.196 cm^2, N_2 saturated solution. 0.1 M $HClO_4$, 5 mV s^{-1}, T=25 °C).

This lack of sensitivity of the carbon intrinsic redox behavior to chemical preparation conditions is a general feature of the present materials. Similar i/E results were obtained also on XPB 334 and XPB 390 derivatives.

RDE oxygen reduction reaction

Oxygen reduction results on FWf Fe 700 are reported in Fig. 2.13 in a comparison with the similar stoichiometric amination product from the same carbon (FW DETA Fe 700). Clearly, the flooding synthesis affords more effective ORR catalytic activity. Much higher ORR onset potentials (~0.5 V SCE) and higher currents are achieved that also approach a well defined limiting current value at the lowest potentials. As shown by means of a detailed kinetic analysis, which is reported in a following section, the materials from this synthesis are promising Pt-free candidate catalysts. The presence of a well defined limiting current shows in fact that any reaction step prior to diffusion mass transport is kinetically fast, as it should be for effective catalysts.

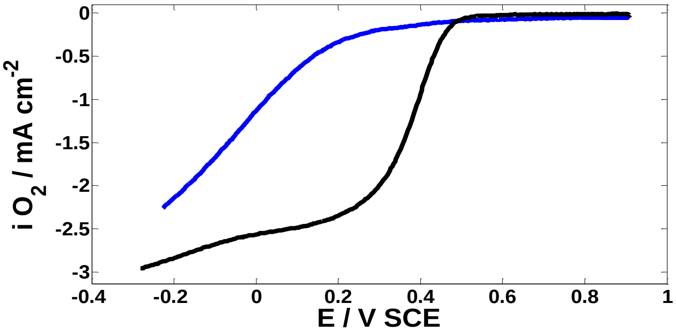

Fig. 2.13. Comparison of i/E ORR results for the two used synthesis conditions. Blue line: stoichiometric amine grafting of DETA in dyglime. Black line: flooding synthesis, DETA as the reagent and solvent.
(Electrode geometrical area 0.196 cm^2, O_2 saturated solution, 1600 rpm, 0.1 M $HClO_4$, 5 mV s^{-1}, T=25 °C, 700 °C pyrolysis in flowing Ar).

Variations in the synthesis procedure were introduced to explore possible improvements. Fig. 2.14 shows a comparison of different pyrolysis conditions. The most effective catalyst turns out to be the sample heated at 900 °C in flowing Ar.

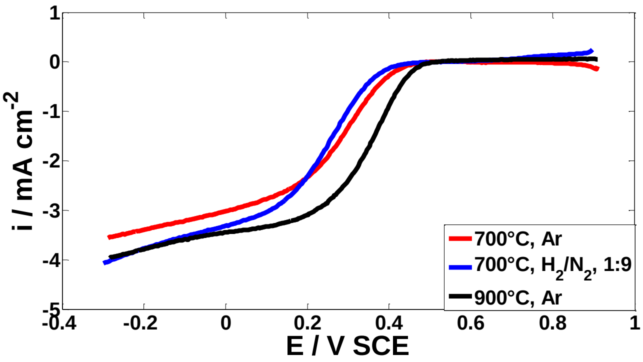

Fig. 2.14. i/E curves on FW200 from the flooding synthesis with DETA and Co. Pyrolysis temperature and gas flow are reported in the legend. (Electrode geometrical area 0.196 cm^2, O_2 saturated solution, 1600 rpm, 0.1 M $HClO_4$, 5 mV s^{-1}, T=25 °C).

Limiting currents are approached in all cases, the best performing sample having been heated at T=900 °C in Ar and showing an ORR onset potential of ~0.5 V SCE.

Currents in the mixed control region were elaborated by means of the Koutecky-Levich, see Chap.2 Section 1.2., to evidence real kinetic currents, after correction for diffusion mass transport and to obtain Tafel line plots, E/logi$_k$, Fig. 2.15.

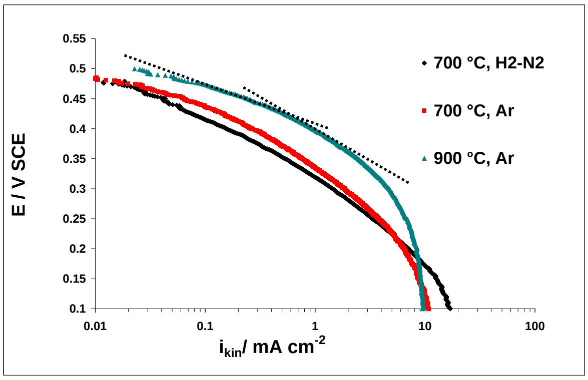

Fig. 2.15. Tafel plots for O_2 reduction onto FW f at different pyrolysis conditions. Black dotted line evidence linear region

Fig. 2.15 shows ORR results from this kind of preparation for different pyrolysis conditions. In the used coordinates a continuous slope variation is observed where, however, relatively good linear sections are apparent, with Tafel slopes of ~60 and ~120 mV dec^{-1} at high (E~0.48-0.43 V) and somewhat lower potentials (E~0.40-0.30 V), respectively.

Results of the sample pyrolyzed at 700 °C in flowing H_2-N_2 (black curve) are close to the similar ones for pyrolysis in Ar at the same temperature (red curve). A shift to more positive potentials and higher currents occurs by increasing the pyrolysis temperature to T=900 °C in Ar (green curve).

Tafel slopes and extrapolated exchange current densities are reported in Tab. 2.6, where Tafel slopes are seen approximately independent of gas composition and temperature even though with favorable effects on exchange current densities that selectively arise by using T=900 °C in Ar.

As far as it was possible to asses the flooding synthesis followed by pyrolysis at T=900 °C in Ar was the best set of conditions developed in the work, and as such was used on other commercial carbon samples.

Tab. 2.6. Kinetic parameters for ORR of FWf samples pyrolyzed in different conditions.

Pyrolysis conditions	LCD mV SCE	Tafel slope mV dec^{-1}	i_0×10^{-10} mA cm^{-2}	HCD mV SCE	Tafel slope mV dec^{-1}	i_0×10^{-6} mA cm^{-2}
700 °C, H_2-N_2	480-430	63	8.53	360-240	125	4.65
700 °C, Ar	480-430	59	0.35	400-300	121	4.38
900 °C, Ar	470-440	62	6.00	420-340	120	9.21

The following results on Degussa XPB 334 and XPB 390, its oxidized version, were obtained to extend the above conclusion to different carbons, with different surface oxidation condition. By results in Section 2.3.3 XPB 390 contains twice as much (~10 atomic %) oxygen groups as the parent XPB 334.

Fig. 2.16 shows a comparison of voltammetric profiles for ORR obtained by RDE technique for such DETA modified carbon supports. The most effective catalyst turns out to be the one from XPB 390, thus suggesting that surface oxygen groups are useful to shift positive the onset ORR potential of the 390 f derivative by E~0.06 V with respect to the similar one of 334 f, to increase ORR currents that also show a steeper potential dependence and better defined limiting current.

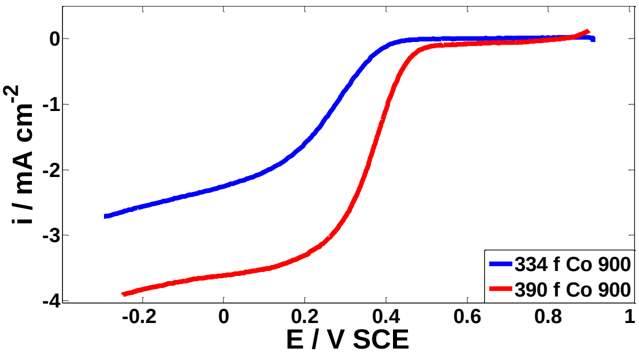

Fig. 2.16. i/E curves for 334 f Co 900 and 390 f Co 900. (Electrode geometrical area 0.196 cm^2, O_2 saturated solution, 1600 rpm, 0.1 M $HClO_4$, 5 mV s^{-1}, T=25 °C).

Catalysts 390 f Co 900 and 334 f Co 900 were adopted to investigate effects from the overall electrode preparation in that, specifically, Nafion amounts are concerned. These results are reported in Section 2.3.

MEA results

Some of the above materials were tested in a single H_2/O_2 fuel cell assembly with the aim of extending and confirming RDE results in realistic usage conditions. A 25 cm^2 electrode surface area was used after optimization of cell assembly and catalyst ink composition. All MEA results in the following are obtained with H_2 and O_2 gas feeding (p=1 atm, T=70 °C) and keeping constant the N/C ratio (N/C=1). Other relevant details are reported in the Experimental Section.

Fig. 2.17 compares some of the relevant galvanostatic E/i curves recorded in the same experimental conditions.

In Fig. 2.17a electrode potentials decrease significantly with increasing current density. Thus, effective catalysts are not obtained by means of stoichiometric amine grafting, also by varying the grafted amine compound and added metal ions.

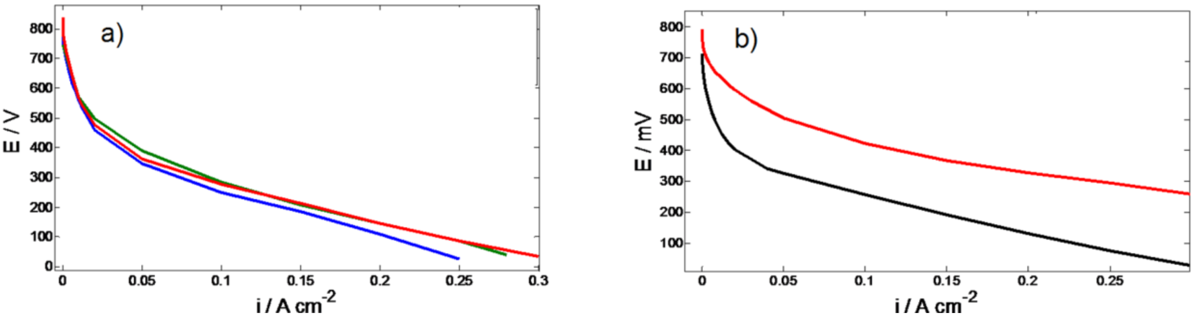

Fig. 2.17. a) Comparison of catalysts from the grafted amine synthesis. Different amine compound and added metal ions (FW D6 Fe 700, blue line; FW D6 Co 700, green line; FW DETA Fe 700, red line).
b) Comparison between amine grafting (FW DETA Fe700, black line) and flooding synthesis (FWf Co 700, red line) with DETA.

In Fig. 2.17b a more effective catalyst is obtained using DETA from the flooding rather than by the amine grafting synthesis. In fact, the open circuit voltage (OCV~800 mV) is higher for former than the latter one (OCV~700 mV) and the potential difference of the cells remains higher (~180 mV) under circulating increasing current. The above difference also occurs by varying temperature and flowing gas composition during pyrolysis.

Effects from pyrolysis temperature (700 and 900 °C) and metal loading (Fe, Co) were investigated on flooding synthesis products only given that, from the above, this brings to better ORR results. In From Fig. 2.18a,b, heating at 900 °C results in better catalytic activity than at 700 °C, with also higher OCV (~40 mV) and higher potentials at comparable current densities. Effects due added metals are more complex because at 700 °C Fe bring to higher potentials than Co, with the opposite taking place at T=900 °C.

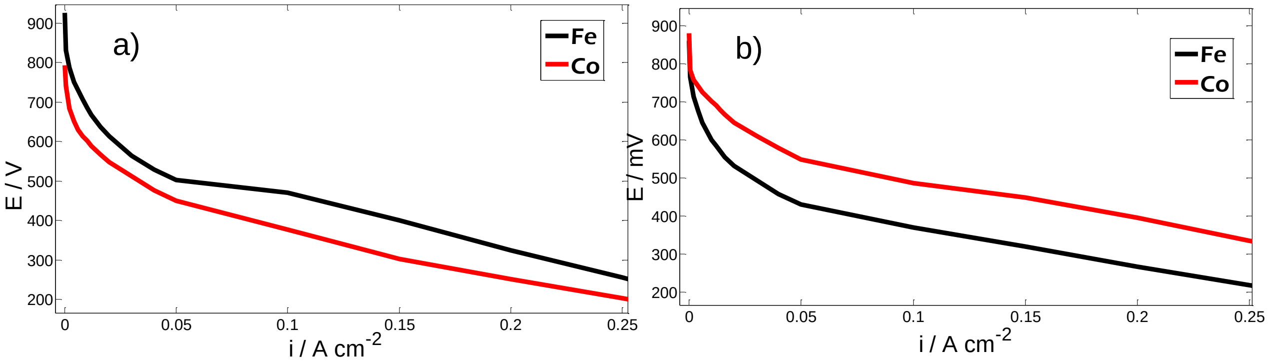

Fig. 2.18. Added metal ion effects on FW f from flooding synthesis after pyrolysis at T=700 °C, a) and T=900 °C b).

This also appears in Power Density plots in Fig. 2.19, that shows the results for all the material tested.

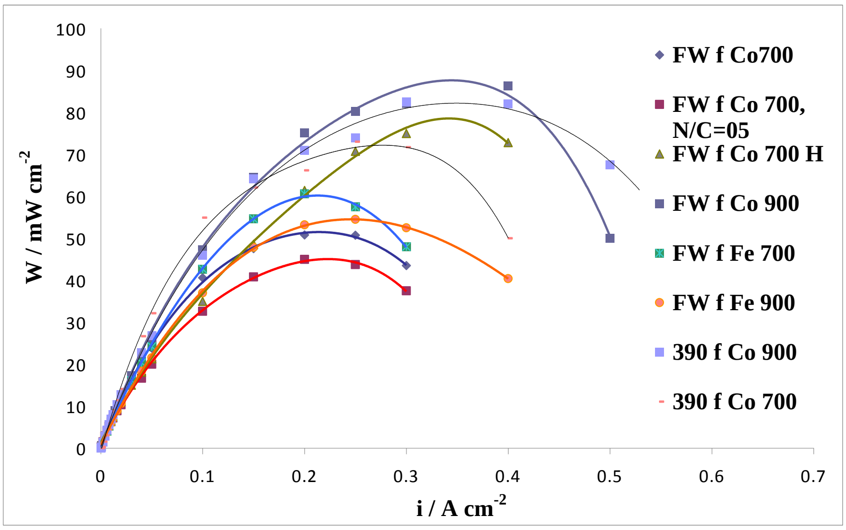

Fig. 2.19. Power density plots from MEA results (25 cm^2 geometric surface area).

For assembled H_2–O_2 fuel cell systems, the maximum output power density reached is ≈90 mWcm^{-2} at 25 °C with FW f Co 900 and 390 f Co 900. These results confirm that effective catalysts are obtained by Flooding synthesis onto oxygen rich-support, Co as metal ion, and pyrolysis at 900 °C**.**

2.3 Nafion as catalyst binder

As described in Chapter 1 Section 1.3.2 Nafion can be used as a binder inside the catalyst layer to minimise both ohmic and mass transport limitations, Fig. 2.20. Effect of Nafion ionomer within the catalyst layer of supported Pt/C has been reported in the previous chapter where the oxygen reduction properties of Pt/C catalysts were investigated by means of a rotating disk electrode (RDE), by varying the relative Nafion/Catalyst ratio (N/C). Well defined limiting currents were recorded for all the investigated Nafion concentrations that weakly depend on the N/C ratio. Tafel slopes were determined in the range ~60-120 mV/ dec^{-1} depending on the potential range. Kinetic hindrances from the diffusion mass transport through the Pt/C layer were obtained by the Koutecky-Levich extrapolation procedure and found to increase for N/C greater than ~0.75.

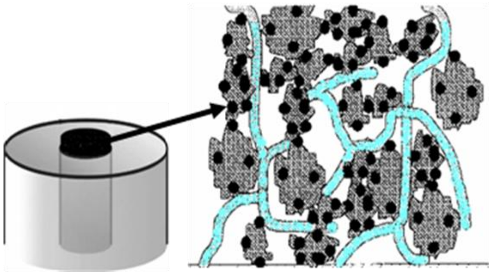

Fig. 2.20. Schematic representation of Nafion inside the catalyst layer.

Stronger N/C effects were observed on Pt-free catalysts, with I/E relations that continuously change in shape with increasing N/C and with well defined, potential independent limiting currents only observed for N/C=0.75 where results of the above extrapolation procedure show that the internal diffusion hindrance is at a minimum.

2.3.1 Electrochemical characterization

The synthesized materials were characterized by Rotating Disk Electrode (RDE) and by a single fuel cell by Membrane Electrolyte Assembly (MEA) technique, to obtain kinetic parameters for Oxygen Reduction Reaction (ORR).

RDE Intrinsic redox behavior

Nafion effects were evaluated by varying Nafion concentration using synthesized materials with some interesting catalytic activity, i.e. nitrogen doped carbon XPB 334 and XPB 390 (Degussa) modified by the flooding synthesis.

The intrinsic redox behavior is reported in Fig. 2.21. H-adsorption/desorption currents are obviously absent. As for other Pt-free materials, I/E profiles in the figure are not affected by N/C variation (see section 1.3.2).

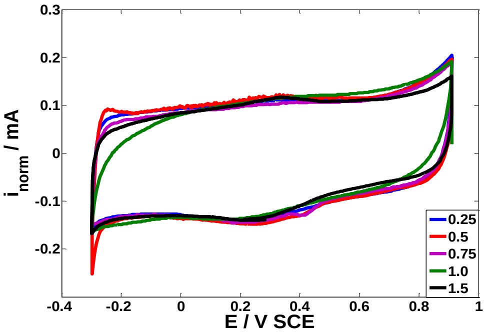

Fig. 2.21. CV I/E curves of 390 f Co 900 catalysts at increasing N/C (see the legend). (N_2 saturated solutions, 0.1 M $HClO_4$, Tamb, 5 mV/s, 0 rpm).

To a better definition of the above feature, results in Fig. 2.21 have been normalized on the total charge obtained by integration of I/E profiles in the investigated potential region.

RDE Oxygen reduction reaction

ORR experimental curves of XPB 390, modified with DETA and added with Co 5 wt% are reported in Fig. 2.22, for all used N/C ratios.

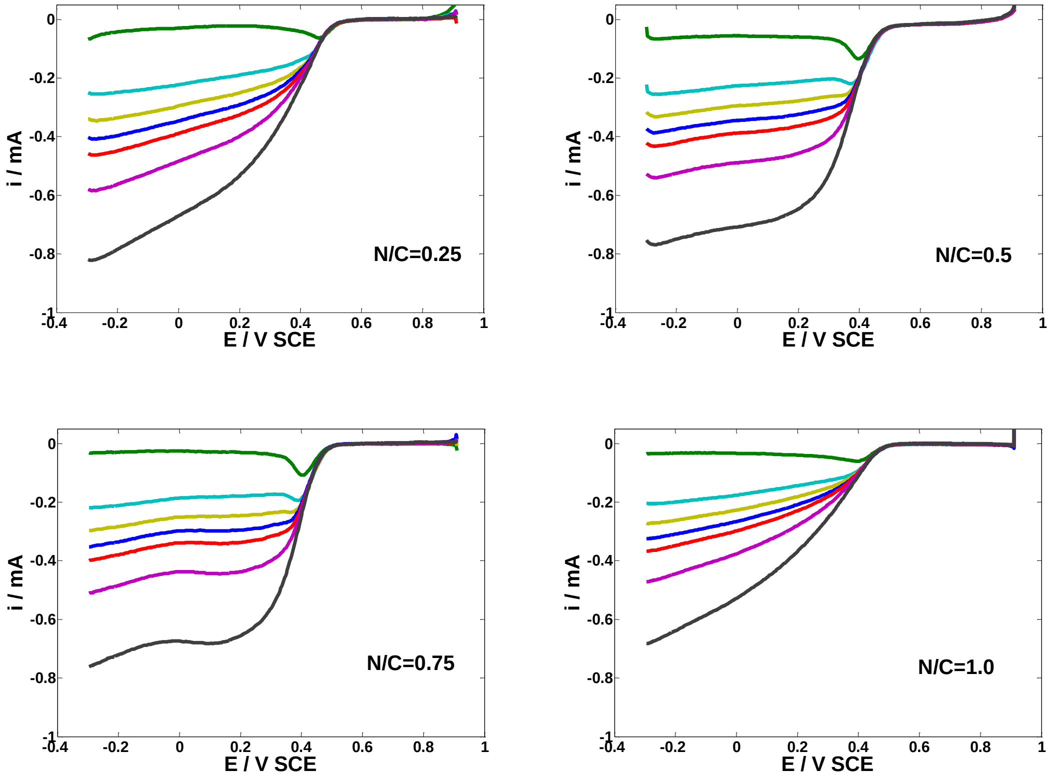

Fig. 2.22. Experimental ORR I/E profiles for increasing N/C ratios at different rpm. XPB 390, modified with DETA and added with Co 5 wt%. RDE rotation rates increase in the order, from 0, 100, 200, 300, 500, 700, 1600 rpm in all the figures (0.1 M $HClO_4$, 5 mV s^{-1}, T=25 °C).

The onset ORR potential (≈ 0.5 V SCE) is not affected by N/C ratio. For N/C=0.25 no limiting current is observed, even for the lowest electrode rotation rate. With increasing N/C a limiting current is at first approached (for N/C=0.5) and fully develops for N/C=0.75 at all rotation rates. With increasing further the N/C ratio the I/E profile changes, losing the limiting current region. This non linear behavior suggests that Nafion is not an inert binder but it plays a more complex ORR role by some interaction with the carbon substrate and active catalytic centre. These interactions are difficult to establish also because the active centre nature is in itself unknown. To obtain some insights into the interplay of mass transport and kinetically controlled reaction steps, the procedure already reported for Pt/C catalysts is adopted (see 1.3.2). In this way Nafion effects on oxygen (and proton) diffusion inside the catalyst layer will be evidenced.

To this end, the first elaboration step is to use the Koutecky-Levich equation to obtain kinetic currents free from mass transport effects across the Nernst diffusion layer in solution. Fig. 2.23 is such a first step showing Koutecky-Levich lines at different electrode potentials for N/C=0.25 and N/C=0.75

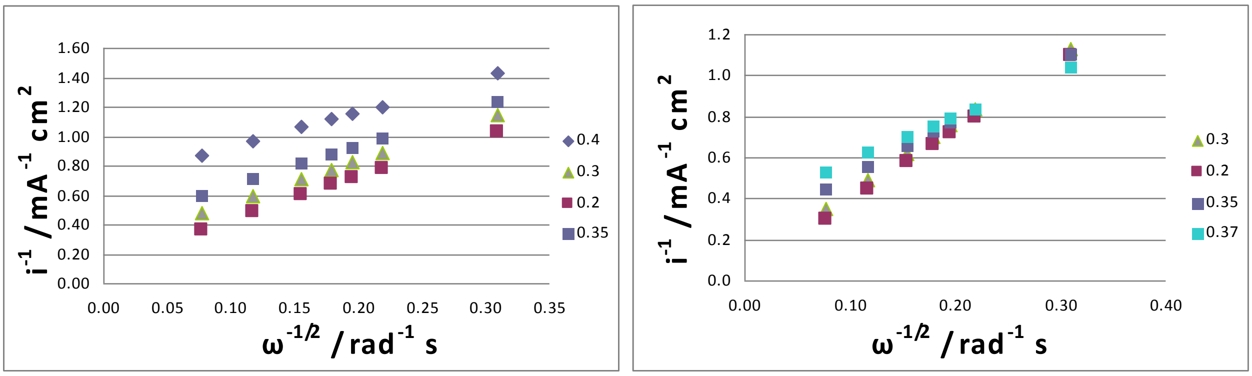

Fig. 2.23. Koutecky Levich plots for O_2 reduction at various electrode potentials as in the legend. Left panel: N/C=0.25; right panel: N/C=0.75. (XPB 390, modified with DETA and added with Co 5 wt%, O_2 saturated 0.1 M $HClO_4$, 5 mV s^{-1}).

Closely linear plots are obtained at the reported N/C ratios for all potentials. Extrapolated i_k^{-1}values (at $\omega\rightarrow\infty$) increase with increasing electrode potential, on the contrary approaching limiting low values with increasing overpotential. Extrapolated kinetic currents are plotted in Tafel coordinates in Fig. 2.24.

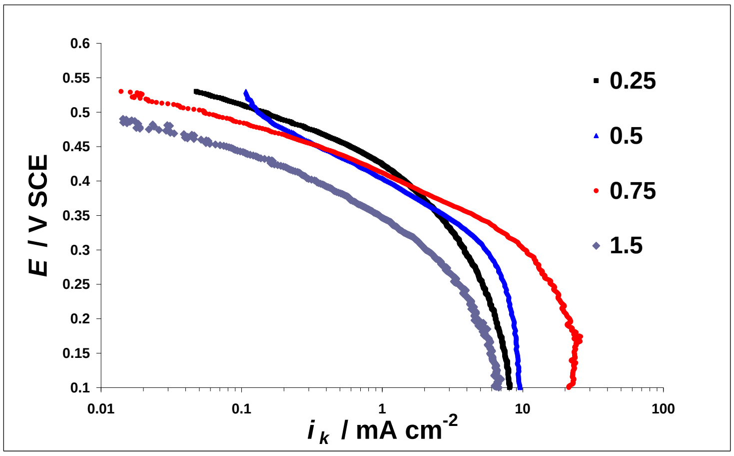

Fig. 2.24. Tafel plots for extrapolated kinetic currents at different N/C ratio (XPB 390, modified with DETA and added with Co 5 wt%).

Quite complex features apply to the figure because of the readily observed Nafion dependent ORR response. Linear Tafel lines are observed for all N/C ratios with slopes of ~60 and ~120 mV dec^{-1}, at high and low potentials, respectively (see Tab. 2.7). An exception occurs for N/C=0.5 with Tafel slope and exchange current density higher than the other values.

Nafion effects also cause the curves to shift with respect to one another. Assuming the N/C=0.25 curve as a reference, the curve with N/C=0.5 is shifted to smaller currents and more negative potentials. The curve with N/C=0.75 is fairly superimposable with the previous one in the high potential region; with decreasing potential (E<~0.4 V) the relevant currents are however higher than for N/C=0.5. A curve shifted to more negative potentials and lower currents is recorded for N/C=1.0.

In the investigated N/C range a well defined Nafion concentration effect occurs, with a maximum ORR promoting effect at N/C=0.75.

Tab. 2.7. Kinetic parameters for ORR at different N/C ratio on 390 f Co 900. LCD=low current density region, HCD=high current density region.

N/C	LCD mV SCE	Tafel slope mV dec^{-1}	i_0 mA cm^{-2}	HCD mV SCE	Tafel slope mV dec^{-1}	i_0 mA cm^{-2}
0.25	540-500	65	4.8×10^{-9}	440-403	118	1.5×10^{-5}
0.50	470-430	97	1.6×10^{-6}	370-320	123	2.5×10^{-5}
0.75	500-460	58	2.6×10^{-10}	360-310	123	2.5×10^{-5}
1.0	500-450	62	1.0×10^{-10}	440-380	122	8.2×10^{-6}

Like for Pt/C catalyst, extrapolated Tafel plots in Fig. 2.24 are characterized by quasi potential-independent currents in the lowest potential region. Because of the previous extrapolation, these currents depend on kinetic mass transport limitations across the catalyst layer. Such internal diffusion currents within the catalyst layer are plotted as a function of N/C ratio in Fig. 2.25 and are seen to increase with increasing N/C up to a maximum at N/C=0.75 and to decrease further at higher N/Cs.

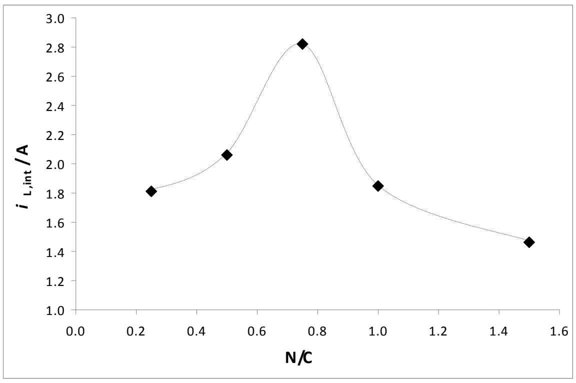

Fig. 2.25. Internal limiting currents as function of Nafion loading

It may be noted that experimental RDE limiting current and internal diffusion currents are obtained for the same Nafion content (N/C=0.75). This coincidence may be assumed to support the conclusion that the internal diffusion step dominates the overall ORR electrode behavior.

It may be noted further that Pt/C and Pt-free catalysts are characterized by different maximum N/C values and different trends of dependence (comparison between Fig. 2.25 and Fig. 1.19). This may be related to variation in the Nafion ionomer interaction with carbon substrates and with ORR catalytic active centre. In Pt/C catalysts active centres are in the form Pt nanoparticles while in Pt-free carbon such centers are presumably distributed throughout the carbon surfaces with likely macrocycle pyridinic structures [1].

After correcting each data point in Fig. 2.24 for internal diffusion, the resulting currents are plotted in Tafel coordinates in Fig. 2.26.

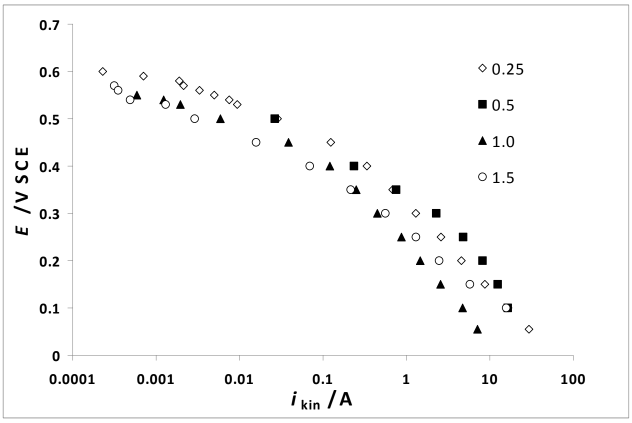

Fig. 2.26. Tafel plot of kinetic currents corrected for external diffusion on nitrogen doped XPB390 with increasing N/C ratio.

As expected limiting currents at higher overpotentials disappear, and, as most relevant to the self-data consistency, each curve maintains the same slope of the starting un-corrected result.

MEA Results

Effect of Nafion concentration inside the catalyst layer was also studied galvanostatically in MEA (Membrane Electrolyte Assembly, see Experimental Section for details about MEA assembly). The aim was to evaluated if RDE data satisfactorily compare with results from fuel cell operating conditions. Data are reported in Fig. 2.27.

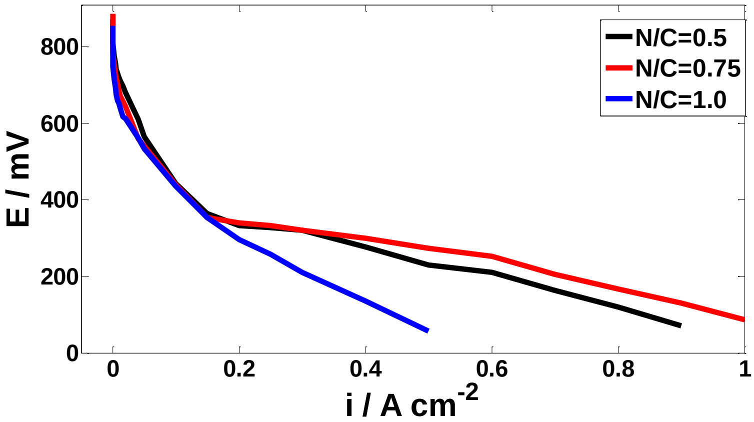

Fig. 2.27. Steady-state cathode polarization curves for 390 f Co 900 at different N/C ratio (see legend). H_2/O_2 feeding, p=1 atm, T_{cell}=70 °C.

The MEA assembly with N/C=1.0 shows the lowest potential in all the current range. Improved activity was obtained decreasing the Nafion concentration to N/C=0.75, where the highest electrode potentials were obtained. For N/C=0.5 potentials are somewhat lower in comparison with N/C=0.75 with values that however remain higher than N/C=1.0.

Thus, MEA results confirm RDE data, independently confirming that Nafion is not an inert catalyst binder, but it interacts with the catalyst determining the cell performance of a fuel cell system.

2.3.2 Un-oxidized carbon support

The same variation in Nafion content was investigated on the un-oxidized support (XPB 334) DETA-doped and metal (Co) loaded from the flooding synthesis procedure.

It is noteworthy that on this carbon support no limiting currents were reached, regardless of the used Nafion concentration. Experimental CVs at different N/C ratio are reported in Fig. 2.28.

The lack of limiting currents, which is apparent as compared to the well defined ones on the oxidized carbon, shows that oxygen-containing surface groups are necessary to improve the catalytic ORR together with nitrogen and metal centres.

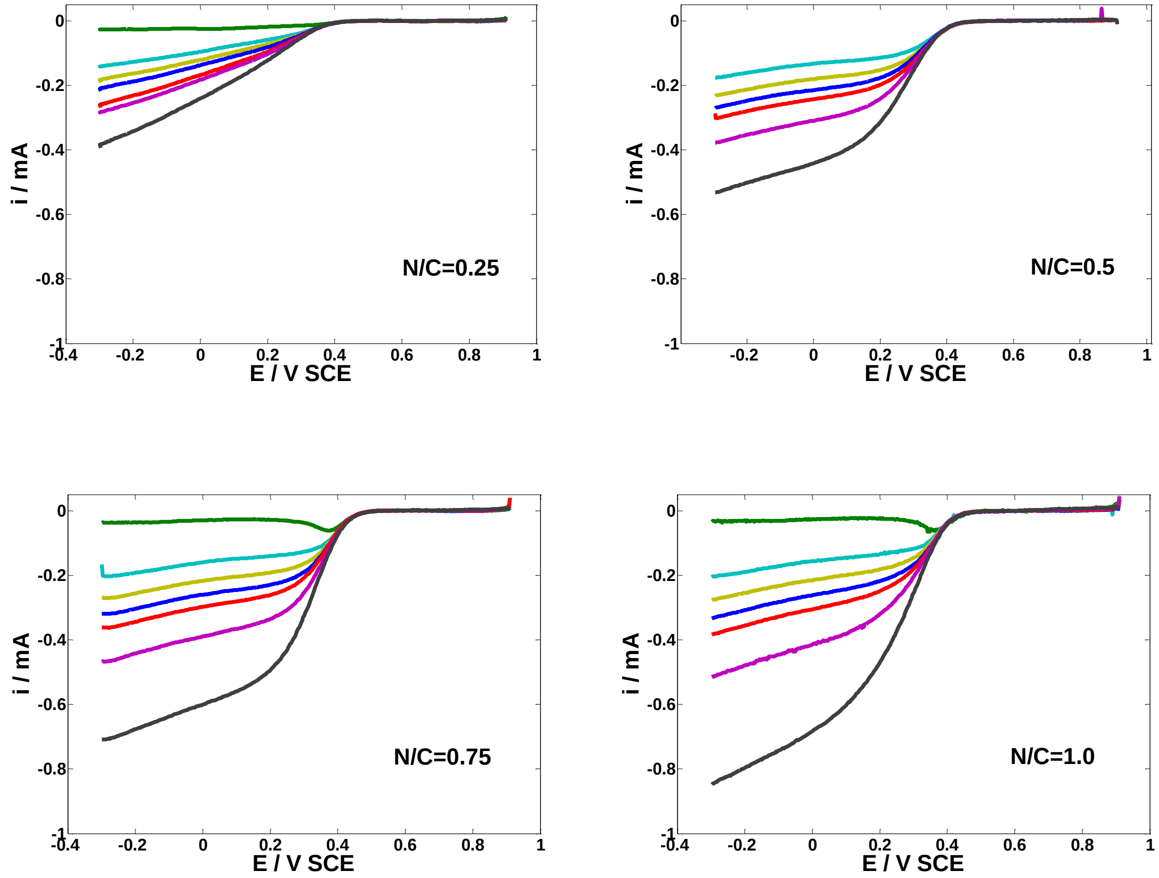

Fig. 2.28. Experimental ORR i/E profiles for increasing N/C at different rpm. Un-oxidized carbon support XPB 334, flooding synthesis with DETA and Co addition (5 wt%). (0.1 M $HClO_4$, 5 mV s^{-1}, T=25 °C).

On this un-oxidized carbon I/E profiles still depend on N/C ratio as for the oxidized support, but in this case limiting currents are only approached, better for N/C=0.75. However, a currents increase occurs with increasing the Nafion (see Fig. 2.29), with at first a linear increase followed by a sharp drop at N/C=1.5.

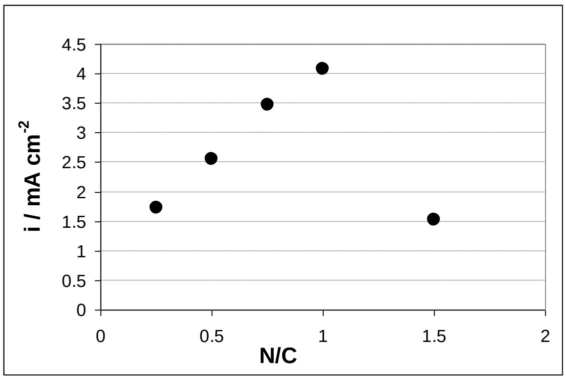

Fig. 2.29. Currents at a constant electrode potential (E=-0.2 V/SCE) for increasing N/C ratio (334 f Co 900, 1600 rpm, 0.1 M $HClO_4$, 5 mV s^{-1}, T=25 °C).

2.4 AUXILIARY CHARACTERIZATION OF CARBONS

Modification of the carbon support is crucial to improve ORR catalytic activity. To obtain more insights into chemical and textural surface features a series of data is reported from investigation techniques like Bohem titrations, SEM and EDAX analysis, BET were used.

Both activated carbon and carbon blacks were used as support. Carbon blacks are produced from pyrolysis of hydrocarbons. They are described by their graphitic crystallite size, (10-25 Å), particle size (20-50 nm), agglomerate size and shape and BET surface area (30-130 m^2 g^{-1}). Pristine carbon black can be modified in a post production stage by an etching gas, leading to BET surface area up to 1000-1500 m^2 g^{-1} and porous network. Activated carbons are produced from pyrolysis of carbonaceous source materials (i.e. wood, lignite, coal and coconut shell) and sequent activation. This latter step can be chemical or physical, in the first case carbons are manufactured by the simultaneous carbonisation and activation of the raw material at 600 - 800 °C. The activating agent for this process, e.g. H_3PO_4 or $ZnCl_2$, is incorporated into the raw material before heating starts. Physical activation, or so-called steam activated carbons, are manufactured from a pre-carbonised material which is obtained by thermal decomposition of a carbonaceous precursor at 600 - 800 °C in the absence or under controlled admission of air. The activation step is usually performed in the presence of steam and/or CO_2 at 800 -1100 °C.

2.4.1 Darco KB-G

Darco KB-G is an activated carbon.

Washing procedure

Boehm titrations were performed to determine the amount of acids (phenols, lactones and carboxyls) and basics groups at the carbon surface. These data are useful to characterize the stoichiometry of carbon surface groups and are therefore essential to the following carbon functionalisation by amine groups.

Results for the activated carbon DG are reported in Tab. 2.10. Two different pre-treatments were used on this carbon by acid (HCl) and basic washing (NH_3) in soxhlet apparatus, both of them followed by extensive washing with Mill-Q water. The resulting carbons are denoted as DG-A and DG-B, respectively. The purpose was to eliminate inorganic impurities normally present in activated carbon (P, Fe) that originated from synthesis and activation procedure.

The commercial carbon and resulting washed samples were characterised and compared with one another by determinations that are reported below. Each washing procedure modifies functional groups at the carbon surface, with the number density of acidic functionalities increasing upon acid washing and that of basic functionalities increasing instead upon basic washing. The extensive water washing after acid and base treatments excludes that these data may depend on acid or base carryover. Then the carbon modification is a real process taking place in spite of the mild condition adopted, Tab. 2.7.

Tab. 2.7. Surface groups onto washed-carbon surface determined by Boehm titrations.

	Phenols µeq/g	Lactones µeq/g	Carboxyls µeq/g	TOT acids µeq/g	Basic groups µeq/g	TOT groups µeq/g	TOT acids/Basics
DG-A	405	169	326	900	42	942	21.43
DG-B	109	25	56	190	487	677	0.39

BET analysis also show that after washing procedure the surface area increase as reported in Tab. 2.8. The surface area increase could be attributed to pore cleavage and impurities removal by the adopted treatment.

Tab. 2.8. BET surface area variation of activated carbon after washing procedure.

Sample	B.E.T. surface area
DG	1493 m^2 g^{-1}
DG-A	1616 m^2 g^{-1}
DG-B	1563 m^2 g^{-1}

Pyrolysis

A more detailed set of BET data were recorded to obtain some insight pyrolysis effect, Tab. 2.9. Since carbon-amine-metal adducts are usually stabilized by thermal treatment in reducing gas flow (N_2/H_2=2:1) at T=600-900 °C, DG-A and DG-B were pyrolyzed at different temperatures to determine any heat treatment effect on the carbon supports alone. Results are reported below (numbers after carbon abbreviation indicate pyrolysis temperature, Celsius degree).

Tab. 2.9. Pyrolyzed activated carbon B.E.T. surface area.

Carbon sample	B.E.T. surface area
DG-B	1563 m^2 g^{-1}
DG-B 500	1509 m^2 g^{-1}
DG-B 700	1127 m^2 g^{-1}
DG-B 800	1120 m^2 g^{-1}
DG-B 900	1111 m^2 g^{-1}
DG-A	1616 m^2 g^{-1}
DG-A 700	1137 m^2 g^{-1}

Heat treatment at 500 °C causes little variation in B.E.T. surface area with respect to untreated carbon DG-B. Surface areas decrease stronger up to T=700 °C and thereafter remain almost unchanged up to T=900 °C.

Pore volume variations after heat treatment are show in Fig. 2.30. Similar to surface area, changes in pore volume mainly occur from 500 °C to 700 °C with only small variations at higher temperature.

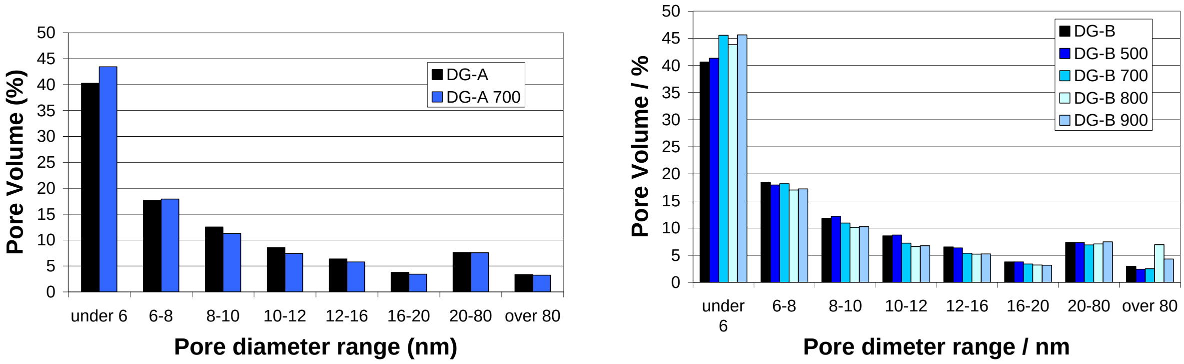

Fig. 2.30. Pore volume variations after heat treatment.

Boehm titrations show a complex picture with thermally induced redistributions of surface groups. As shown in Tab. 2.10 phenols increase on both heat treated DG-A and DG-B. Carboxyls increase especially on DG-A and remain nearly constant on DG-B. An opposite trend of variation is observed for lactones that strongly increase on DG-B and remain nearly constant (with actually a small decrease) on DG-A. Basics groups decrease on both DG-A and DG-B.

Tab. 2.10. Pyrolyzed material Boehm titrations results.

	Phenols μeq/g	Lactones μeq/g	Carboxyls μeq/g	TOT acids μeq/g	Basic groups μeq/g	TOT gruops μeq/g
DG-B	109	25	56	190	487	677
DG-B 500	262	113	54	429	311	740
DG-A	405	169	326	900	42	942
DG-A 500	447	130	553	1130	8	1138

2.4.2 FW200

Washing procedure

The commercial carbon black Degussa FW 200 (COLOUR BLACK FW 200, CAS. 1333-86-4) was also used as a supporting material for nitrogen doped carbon synthesis. This carbon black is a pigment black obtained by the Degussa Gas Black Process and its properties are briefly reported in Tab. 2.11.

Tab. 2.11. Properties of the commercial carbon black FW200

Type	High Colour Gas
Volatile Matter 950 °C	17.0-23%
pH value	1.0-4.0
Ash Content	0.02%
BET Surface Area	471 m^2/g
Average primary particle size	13 nm

Boehm titrations were performed to determine the amount of acids (phenols, lactones and carboxyls) and basics groups at the carbon surface. These data are useful to characterize the stoichiometry of carbon surface groups and are therefore essential to the following carbon functionalisation by amine groups, Tab. 2.12.

Tab. 2.12. Surface groups determined by Boehm titrations onto untreated carbon black FW200.
***Total groups are not reported due to the negative value of basic groups.**

	Phenols µeq/g	Lactones µeq/g	Carboxyls µeq/g	TOT acids µeq/g	Basic groups µeq/g	TOT groups µeq/g
FW200	226 ± 46	553 ± 18	766 ± 10	1545 ± 74	-320 ± 2	*

The negative value of basic groups is only apparent and is attributed to release of acid impurities during carbon equilibration in HCl solution as necessary to determine basic groups. So, in data elaboration the amount of released acid is greater than possible contributions from any basic group and gives rise to negative values for basic groups. This hypothesis was confirmed performing Boehm titrations onto a carbon black washed 24 hours with water in a Soxhlet apparatus by which a decrease in the (negative) amount of basic group was found.

From energy dispersive X-ray analysis (EDAX) and thermal analysis coupled with a mass spectroscopy (TGA-MS) sulphur is detected as impurity in carbon. After washing procedure sulphur content decreases from 0.15% (atomic percentage) to 0.10% indicating that sulphur is at least partly reticular. The oxygen content is very high and remains fairly constant (from 16% atomic percentage to 17%) upon Soxhlet extraction, with however a redistribution of acidic oxygen containing groups as shown in Tab. 2.13 and Fig. 2.31.

Tab. 2.13. Surface groups determine by Boehm titrations onto water-washed carbon black (FW200_w).
***Total groups are not reported due to the negative value of basic groups.**

	Phenols µeq/g	Lactones µeq/g	Carboxyls µeq/g	TOT acids µeq/g	Basic groups µeq/g	TOT groups µeq/g
FW200 w	390 ± 16	160 ± 18	1079 ± 7	1629 ± 41	-151 ± 15	*

Phenols and carboxyls groups are seen to increase and lactone groups to decrease. This is probably due to lactone rings opening to form carboxyls and phenols groups.

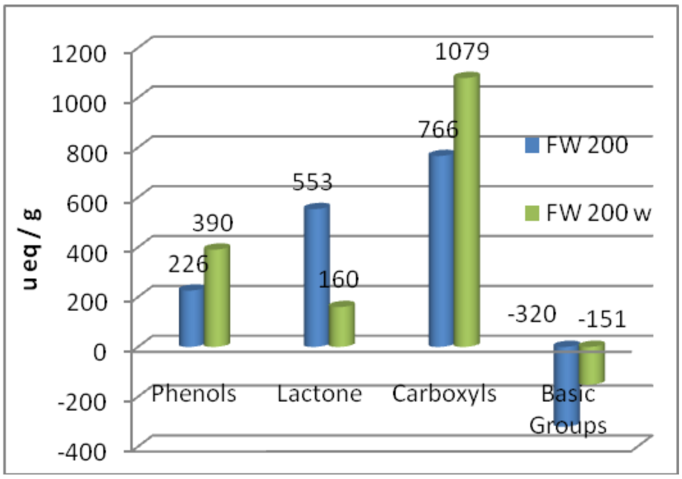

Fig. 2.31. Redistribution of commercial carbon black surface groups after washing procedure in a Soxhlet apparatus for 24 hours at 100°C.

As mentioned before the commercial carbon black was also characterised by thermo gravimetric analysis combined with mass spectroscopy analyzer. The carbon black decomposes releasing H_2O (50-150 °C), CO and CO_2 (120-900 °C) and SO_4-related species (220 °C-400 °C with a maximum at 280 °C).

SEM EDX characterization

Scanning Electron Microscopy (SEM) uses the scattering of electrons from the surface of the sample to reveal the topography of the material. It also utilises the scattering power of different materials to distinguish them. Gold coating is used to increase resolution of the topographical features. Another useful SEM facility which uses the interaction of the electron beam with some of the surface atoms (up to 100 nm deep) to give X-rays which can be analyzed to reveal the surface composition, EDAX. This technique is limited in most general instruments to elements of higher atomic weight than fluorine.

Scanning electron microscopy (SEM) and energy dispersive X-ray analysis (EDX) were performed onto the commercial carbon black to determine morphology and surface atomic composition.

As shown in Fig. 2.32 agglomerates are present comprised of smaller particles with quite homogeneous particles size distribution. The white color in the first figure, is representative of less conductive material and therefore, of amorphous carbonaceous matter in the carbon structure.

There are no differences from pristine carbon black and Soxhlet extracted carbon black (pictures not reported).

Surface area analysis performed using the BET method shows that the carbon porosity is in the macroporosity range.

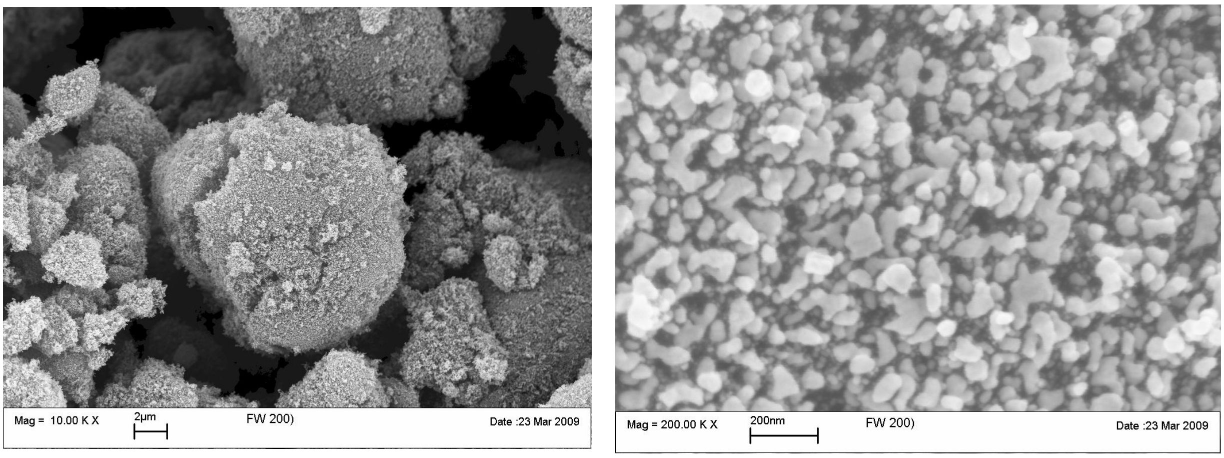

Fig. 2.32. SEM images of commercial carbon black FW 200 at different magnification.

2.4.3 XPB 334 and XPB 390

BET surface area

Other carbon supports were used, XPB 334 that is a very fine furnace black with high surface area and high structure, and the commercially available oxidized form of it, XPB 390. The idea was to understand if surface oxide, introduced by oxidation, may offer a reactive sites for nitrogen loading. A preliminary study of the carbon support was performed by SEM, EDX, BET.

BET surface areas of the two carbon blacks are reported in Tab. 2.14. After oxidation the surface area increases of ~115 m^2 g^{-1}

Tab. 2.14. B.E.T. surface area of pristine carbon blacks, XPB 334 and its oxidized version, XPB 390.

Sample	B.E.T. Surface Area m^2 g^{-1}	Media m^2 g^{-1}
XPB 334	625.1	616±13
	607.0	
XPB 390	741.4	730±17
	716.8	

Porosity distribution is not affected by oxidation process and it is mainly concentrated in the meso-macro porous region.

SEM and EDX analysis

SEM images show that no morphological modifications take place after oxidation. It is possible that morphological modification are not visible at SEM magnification, Fig. 2.33.

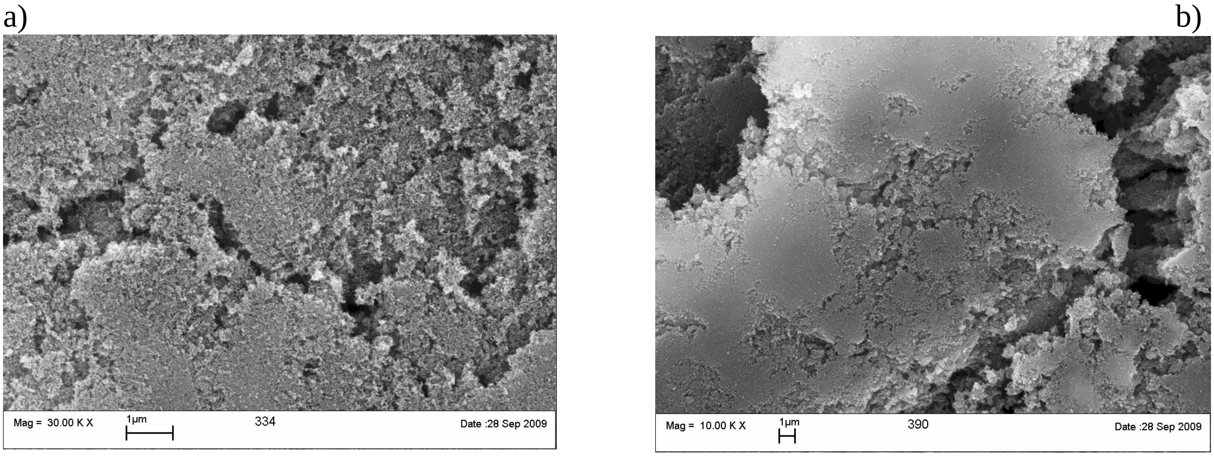

Fig. 2.33. a) SEM images of XPB 334, b) XPB 390. Scale 1 µm.

EDAX analysis reveals an increase in oxygen content after oxydation, Tab. 2.15, from ~6% to ~12% mass percentage. Since this technique shows the composition up to 100 nm deep, The oxygen increase can be attributed to surface groups that can react in with amino compound during the synthesis procedure.

Tab. 2.15. Carbon blacks surface composition from EDAX analysis.

	C		**O**		**S**	
	Mass%	**Atom %**	**Mass%**	**Atom %**	**Mass%**	**Atom %**
XPB 334	93.72	95.28	6.08	4.64	0.20	0.08
XPB 390	87.09	90.06	12.69	9.85	0.22	0.08

2.4.4 Synthesized catalyst

FW 200 derivates

Scanning Electron Microscopy (SEM) and Energy Dispersive X-ray Analysis (EDX) were performed onto the modified carbons to determine the morphology and surface atomic composition.

All analyzed samples have the same morphology: big agglomerates formed by smaller particles with homogeneous particles size distribution. Pictures at lower magnification (Fig. 2.34, Mag. 250x) show that the biggest particles are agglomerates of different shape and size that vary from few to more than 100 micron.

The smaller particles in the agglomerates are homogeneous in size with apparently no difference among.

Pictures at higher magnification are reported in the Fig. 2.34b.

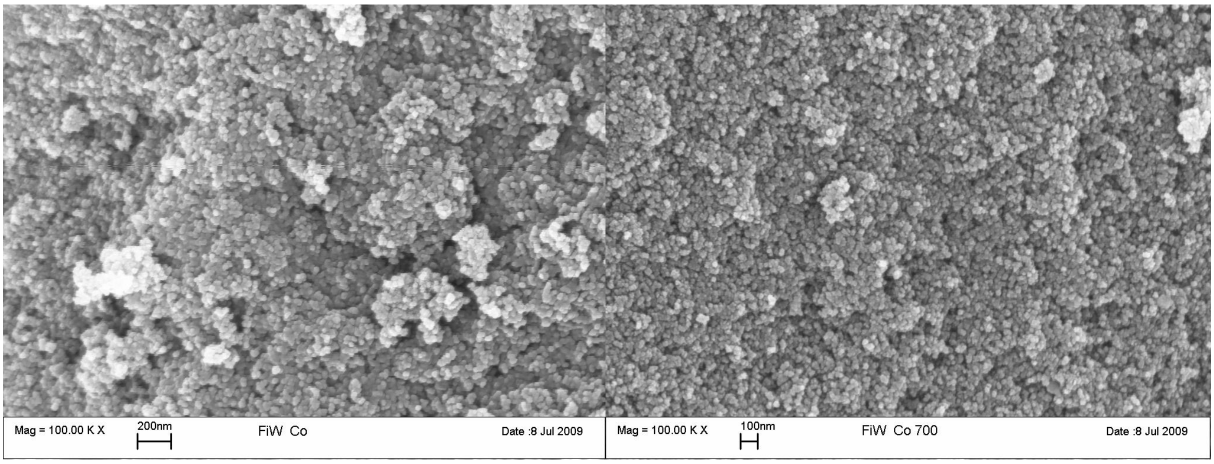

a) b)

Fig. 2.34. SEM pictures of FW f Co before (a) and after (b) heat treatment at 700 °C in argon gas flow.

The agglomerates are formed by particles ranging ~20 nm in size, often fused together to form an homogeneous layer. This is the typical morphology for a carbon black.

After pyrolysis there is a decrease in the amorphous part of the carbon black that is shown in the picture by the white (less conductive) parts.

Carbon black morphology does not change with increasing temperature and varying gas flow composition.

Atomic composition of the pristine and modified carbons was determined by EDAX analysis and are reported in Tab. 2.16.

Tab. 2.16. EDAX analysis for pristine and modified carbon black FW.

	C		O		Co		Fe		S	
	Mass %	**Atom %**	**Mass %**	**Atom %**	**Mass %**	**Atom %**	**Mass %**	**Atom %**	**Mass %**	**Atom %**
FW	83.8	87.2	16.2	12.7	-	-	-	-	0.4	0.2
FW 700	88.5	91.2	11.3	8.8	-	-	-	-	0.2	0.1
FW f Co	79.3	85.6	16.4	13.3	3.6	0.8	-	-	0.6	0.3
FW f Co 700	89.5	93.7	7.0	5.5	3.2	0.7	-	-	0.3	0.1
FW f Co 700 H	87.8	93.7	6.2	4.9	5.9	1.3	-	-	0.2	1.3
FW f Co 900	90.8	94.4	6.3	4.9	2.8	0.6	-	-	0.2	0.1
FW f Fe 700	88.4	92.5	8.7	6.9	-	-	2.7	0.6	0.2	0.6
FW f Fe 900	89.6	93.3	7.8	6.1	-	-	2.4	0.5	0.2	0.1

After pyrolysis at T=700 °C (FW 700) the commercial carbon black FW undergoes a decrease in sulfur and oxygen content (~4%). Release o sulfur species probably indicates the presence of surface groups containing this element. Such groups can explain the negative value of basic surface groups determined by Boehm titrations if this element is in the form acidic impurities.

Total weight losses upon sample pyrolysis at 900 °C is 29.5%, due to release of H_2O, CO and CO_2 as shown by thermogravimetric analysis (TGA). TGA analyses also show a release of sulfate groups from circa 200 °C to 400 °C, which explains the decrease in sulfur content.

After modification with diethylenetriamine and cobalt by flooding synthesis, FW f Co, EDAX analyses detected Co but not N because such element cannot be detected if present in amounts lower than 20% (atom percentage). The cobalt amount in FW f Co remains fairly constant after pyrolysis at 700 °C in Ar flow; O and S content instead decrease after modification. When FW f Co is pyrolyzed at 700 °C in H_2/N_2, Co and O are detected in greater and lower amounts, respectively, than in inert atmosphere. Increasing the pyrolysis temperature (900 °C) in inert gas flow does not significantly change atomic percentage distributions, with only a small decrease in oxygen content. The weight loss during the pyrolysis at 900 °C is 32%, close to 30% of the sample pyrolyzed at 700 °C.

When Fe is used as metal centre, atomic composition does not change at the pyrolysis temperatures used, 700-900 °C. By comparison with the samples pyrolyzed at the same temperature but loaded with Co, the Fe is detected in lower amount

XPB 334 and XPB 390 derivates

SEM and EDAX analysis were also performed onto XPB 334-390 carbons modified by flooding synthesis, Tab. 2.17.

Tab. 2.17. EDAX analysis for pristine and modified carbon black XPB 334 and XPB 390. Abbreviation "b" stands for an analysis onto a completely independent sample (reproducibility test).

	C		O		Co		S	
	Mass %	**Atom %**	**Mass %**	**Atom %**	**Mass %**	**Atom %**	**Mass %**	**Atom %**
XPB 334	93.72	95.28	6.08	4.64	-	-	0.20	0.08
334 f Co 900	89.41	93.63	7.12	5.60	3.28	0.70	0.19	0.07
334 f Co 700	91.37	95.40	4.79	3.76	3.66	0.78	0.17	0.07
XPB 390	87.09	90.06	12.69	9.85	-	-	0.22	0.08
390 f Co	84.94	90.47	10.74	8.59	4.32	0.94	-	-
390 f Co 700	88.38	93.39	7.03	5.57	4.34	0.93	0.25	0.10
390 f Co 900	89.23	94.00	6.34	5.01	4.24	0.91	0.18	0.07
390 f Co 900 b	89.18	94.04	6.24	4.94	4.36	0.94	0.22	0.09

Considerations on the EDAX analysis onto un-modified carbon are reported in the previous Section 2.4.3 and are reported here for comparison with the modified carbons.

For XPB 334 the O amount decrease after flooding synthesis and pyrolysis at 700 °C while surprisingly increase after pyrolysis at 900 °C. The S amount remains fairly unchanged. For that reason it is thought that such element is not an impurity as in the case of FW 200 but it is in form of stable compound onto the carbon surface. Co mass amount is somewhat higher ($Co_{700\ °C}$ =3.66% and $Co_{900\ °C}$ =3.28%) for the sample pyrolyzed at lower temperature.

Atomic distribution after flooding synthesis and pyrolysis for XPB 390 is reported. The O amount decrease after amino and metal loading, 390 f Co. Such decrease is more evident after pyrolysis at 700 °C and it is higher after heat treatment at 900 °C. Co amount remain fairly the same after synthesis (390 f Co), pyrolysis at 700 °C (390 f Co 700) and pyrolysis at 900 °C (390 f Co 900), like S. The Co constant amount may explain the high catalytic activity of this materials, it should be that oxygen surface group stabilized the catalytic centre that could contains Co.

2.5 Glucose/histidine based composites

2.5.1 Introduction

Among various materials, nitrogen modified carbons also containing non-precious transition metals (Fe and Co) are considered interesting because of their ORR activity and reliability as confirmed by results from independent groups [13-23]. Several preparative methods are reported: (1) carbon impregnation with metal organosalts or cyanoderivatives, followed by thermal activation in the presence of e.g. ammonia gas [13]; (2) thermal treatment of nitrogen-containing metal complexes adsorbed onto carbon [24-34]; (3) polymerization of aromatic compounds, e.g. pyrrole [35, 36], onto carbon surface followed by metal ion adsorption (Co^{2+}) to obtain porphyrine- like structures; (4) thermal treatment of mixed precursors from a carbon and nitrogen source, respectively, e.g. glucose and an amino acid, added with transition metal salts (Fe, Cu) [17, 22]. These latter materials are considered interesting because of the ease and flexibility of the synthetic route and, moreover, of the catalytic activity, with incipient oxygen reduction potentials closely approaching (by ~40 mV) those of commercial Pt catalysts [22]. Unfortunately, however, they are reported with low stability [22].

Recently, thermodynamic criteria were put forward to model the catalytic activity of Pt-free bimetallic alloys [47] permitting to evaluate, what metal, or combination of metals, may be most effective in ORR. As a result, Fe^{2+}/Cu^{+} ions were shown most favorable. Interestingly these ions are also present in natural enzymatic systems like cytochrome *c* oxidase, an effective and selective catalyst in the reduction of oxygen to H_2O, based on a cooperative effect of the two ions.

Improving catalyst activity is not only a matter of varying composition but also involves morphological/textural aspects. By reference to carbon supported Pt catalysts, carbon origin, surface area, porosity and pore size distribution reportedly affect end material performances. Reviewing these aspects, Antolini [48] has recently shown that besides good electrical conductivity, carbon supports have to be characterized by high surface areas and high fractional pore percentage in the mesoporosity region (2–50 nm) in order to favor reactant mass transport to and from catalytic centers, the more so if the catalytic sites are preferentially located at inner positions of the carbon structure, in the micropore size region as reported in Ref. [49].

Histidine was chosen as the nitrogen-bearing precursor, because it contains both an imidazolic ring and a carboxyl group that, if retained in end products upon thermal activation, may presumably contribute to ORR activity [48-50]. In the attempt of increasing carbon surface area and at the same time controlling porosity in the mesoporosity range, a hard template method was adopted using silica gel suspensions in water. Also, Fe^{2+} and Cu^{2+} in variable ratios were used to explore the entire composition range as suggested by the theoretical examination in Ref. [47].

The synthesized materials, at different glucose and histidine molar ratio and relative amount on Fe and Cu (Fe and Cu ions at 1 wt.-% total with respect to glucose + histidine, at variable ratios between them) are reported in Tab. 2.18.

Tab. 2.18. Synthesized carbon materials.

	Glu/Hist Molar ratio	**Fe/Cu wt. %**
Glu (no silica)	1:0	-
Glu	1:0	-
Glu Hist 0.1	1:0.10	-
Glu Hist 0.25	1:0.25	-
Glu Hist 0.5	1:0.5	-
Glu Hist	1:1	-
Glu Hist Fe 0	1:1	0/100
Glu Hist Fe 25	1:1	25/75
Glu Hist Fe 50	1:1	50/50
Glu Hist Fe 75	1:1	75/25
Glu Hist Fe 100	1:1	100/0

The obtained materials were characterized using electrochemical, cyclic voltammetry, and physical techniques like BET, XRD and XPS.

2.5.2 Characterization

BET analysis

In the presence of silica gel as a templating agent, carbon materials with expanded, sponge-like overall morphology are obtained as shown by TEM images in Fig. 2.35, for a plain glucose sample heated at *T* = 600 °C.

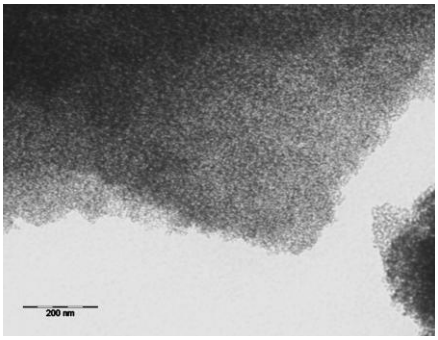

Fig. 2.35. TEM image of Glu sample (T=600 °C).

These effects are more quantitatively observed in the first two entry lines of Tab. 2.19, where the sample obtained in the presence of silica shows a tremendous increase of BET surface area (1,100 m2 g–1) instead of a few square meters per gram of the corresponding glucose-only sample.

Tab. 2.19. Specific surface area (m^2 g^{-1}).

	Surface area m^2 g^{-1} T=600°C	**Surface area m^2 g^{-1} T=900°C**	**S_{900}/S_{600}**
Glu (no silica)	25	-	-
Glu	1143	-	-
Glu Hist 0.1	950	714	0.75
Glu Hist 0.25	728	700	0.96
Glu Hist 0.5	813	-	-
Glu Hist	603	541	0.90
Glu Hist Fe 0	670	564	0.84
Glu Hist Fe 25	-	555	-
Glu Hist Fe 50	696	559	0.80
Glu Hist Fe 75	665	589	0.88
Glu Hist Fe 100	698	587	0.84

Though in the absence of comparison data without added silica, Tab. 2.19 shows that similarly high BET areas are obtained for all the samples. Interestingly, besides depending on silica, surface areas are a function of the used reactant, reactant concentration and heating temperature. Most relevant effects are due to histidine that, at even the lowest used molar ratio with respect to glucose (see GluHist0.1 in Tab. 2.19), causes a surface area decrease of ~200 m^2 g^{-1}, with a further decreasing trend taking place with increasing histidine/glucose molar ratio. Though moderate, opposite effects arise from metal ion addition, with surface areas in any case greater than the metal-free reference (sample GluHist) and also weakly increasing with increasing the Fe^{2+}/Cu^{2+} ratio. As expected on general grounds, and in accordance with some matter loss visually observed as brownish gas emitted during the second heating at T = 900 °C, surface areas decrease with increasing temperature. This decrease is in some relation with surface areas from the previous heating at T = 600 °C. As a fact, the last column in Tab. 2.19 shows that surface areas at T = 900 and 600 °C are in a circa constant ratio of 0.75–0.9. In a further aspect of this thermal behavior, BET fractional pore volume distributions of many samples were found essentially independent of heating temperature. This is shown as an example in Fig. 2.36 for sample GluHistFe75.

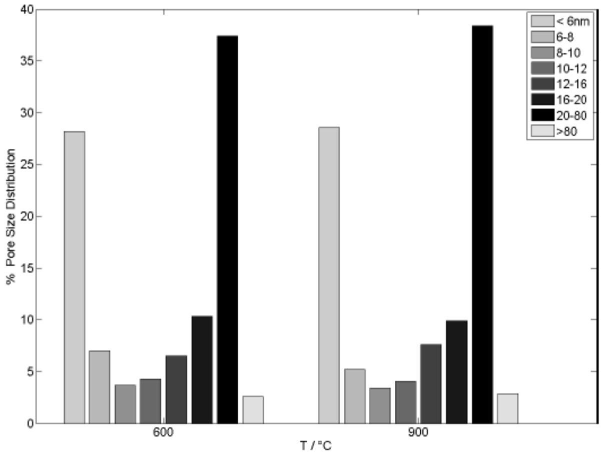

Fig. 2.36. Pore size distributions at different temperatures for GluHisFe75.

Then, the above surface area ratio and the lack of variation in pore volume distribution appear related, and jointly suggest that textural sample features are mostly established during the first heating in the presence of silica, followed by lesser rearrangements taking place at higher temperature after silica removal, these readjustments in their turn causing a moderate decrease of previous surface areas while leaving essentially unchanged porosity distribution.

Reactant composition effects on porosity are reported for the more extensively available results at T = 600 °C. In Fig. 2.37 histidine addition causes readjustments of the pristine glucose porosity, especially relevant at both the extremes of the accessible pore size range.

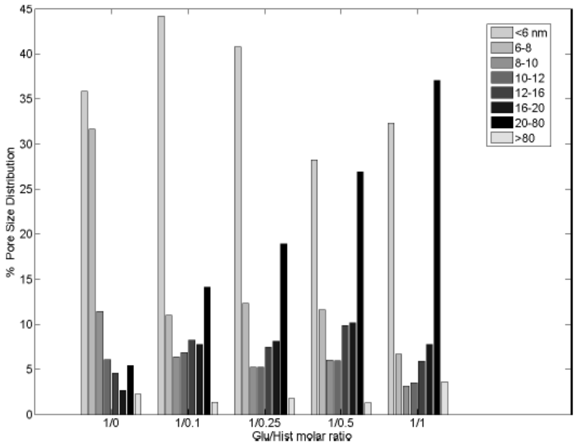

Fig. 2.37. Pore size distributions at various Glu/His molar ratio.

In the low size region, pores 6–8 nm in size undergo a first redistribution in favor of the smaller ones (6 nm). Though with irregular variations, pores with these latter sizes are a large fractional value regardless of increasing histidine amounts. At the other extreme of size, increasing histidine causes the 20–80 nm pore size to become gradually more abundant, up to ~35% of the overall sample porosity. Adding Fe^{2+} and Cu^{2+} ions in variable relative amounts has no apparent effect (not reported) on the porosity distribution of a number of carbons with constant Glu/Hist ratio (Glu/Hist = 1:1). Histidine is therefore most effective to promote pore size increase. This is at variance with Maruyama's results [17] on similar glucose/adenine carbons from a 'dry' procedure without templates.

X-ray photoelectron spectroscopy (XPS)

XPS survey results are shown in Tab. 2.20.

Tab. 2.20. Atomic C, O, N percent sample compositions.

	N 1s %		**O 1s %**		**C 1s %**	
	T=600 °C	**T=900 °C**	**T=600 °C**	**T=900 °C**	**T=600 °C**	**T=900 °C**
Glu	-	-	6	-	94	-
Glu Hist	14	7	4	2	82	91
Glu Hist 0.1	4	4	5	2	91	94
Glu Hist Fe 0	14	-	4	-	82	-
Glu Hist Fe 50	13	7	5	2	82	91
Glu Hist Fe 75	13	8	5	2	83	90

Cu and Fe are undetected even for the lower used heating temperature. This situation is frequently observed, and unresolved, in the literature with the baffling outcome that, though undetected in outermost surface layers, added metals are indeed effective in promoting electrochemical ORR carbon behavior. As also representative of the present results, we mention that Fe was undetected by both XPS and UPS [51] in spite of wide variation in added amounts, the maximum Fe value reaching 5.5 wt% with respect to the graphite oxide that was used in that case. Moreover, in [52], it is reported that, "after carbonization, the content of copper decreases as the copper ions are reduced into metallic copper nanoparticles. These nanoparticles are difficult to detect by XPS because they are coated by a thin carbon layer and migrate into the carbon matrix". As observed in Tab. 2.20 for samples heated at both T = 600 and 900 °C, the relative abundance of C1s and N1s signals is moreover only weakly affected by metal addition.

Tab. 2.20 shows that N1s signals of GluHist (T = 600 °C) are initially very high (14%) and decrease with both increasing temperature (7%, T = 900 °C) and decreasing the histidine amount adopted in preparation (4%, GluHist0.1). Notably, the temperature-dependent nitrogen decrease is accompanied by increasing C1s signals (from 82 to 91%) showing that nitrogen removal also induces chemical carbon readjustments. Figure 2.38 and Table 2.21 evidence that different nitrogen forms are present (Figure 2.38a) with variable and temperature-dependent relative amounts (Figure 2.38b).

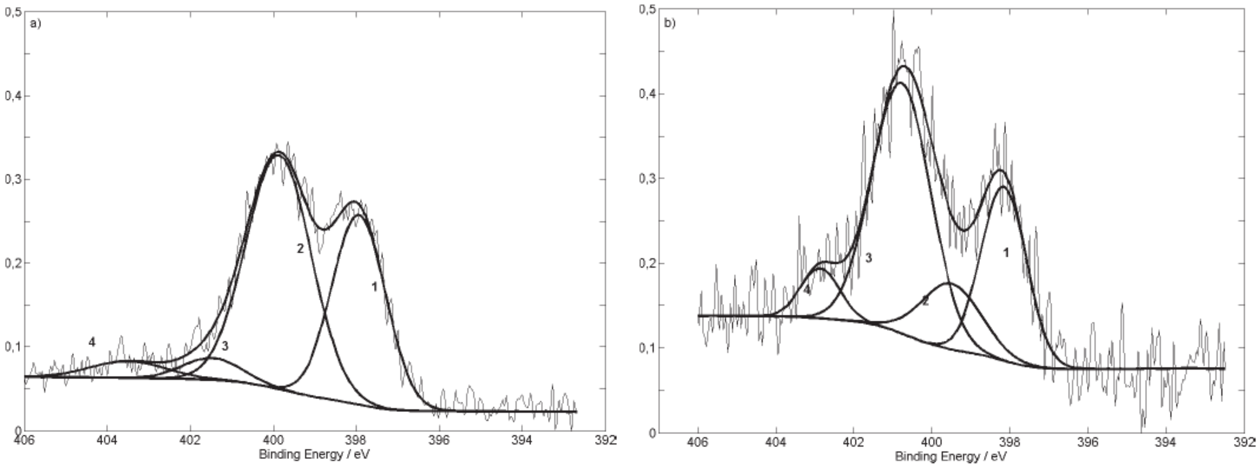

Fig. 2.38. High resolution nitrogen (N1s) spectra of GluHist: (a) T = 600 °C; (b) T = 900 °C. (1) Pyridinic N (N6) (B.E. 398–398.4 eV); (2) Pyrrolic-N in five member ring and/or pyridonic-N (N5) (B.E. 400–400.5 eV); (3) quaternary-N (NQ), e.g. N in graphene structure (B.E. 401.5– 402.2 eV); (4) pyridinic-N-oxide (NX) (B.E. 403.5–404.8 eV) B.E. are from Ref. [53-56].

Tab. 2.21. Atomic N percent sample compositions.

	B. E. (eV)	**Description**	**GluHist**		**GluHistFe50**		**GluHistFe75**	
			T=600 °C	T=900 °C	T=600 °C	T=900 °C	T=600 °C	T=900 °C
N6[a)]	398.0-398.4	Pyridinic N	36	27	39	37	38	36
N5[a)]	400.0-400.5	Pyrrolic N in five member ring and pyridonic-N	55	14	48	48	51	45
NQ[a)]	401.5-402.2	Quaternary-N	5	52	4	5	8	16
NX[a)]	403.5-404.8	Pyridinic-N-oxide	4	7	9	10	3	3

In GluHist for T = 600 °C two main contributions are due to pyridinic (N6) and pyrrolic/pyridonic (N5) forms, in relative amounts of 36 and 55 at %, respectively. Minor contributions are due to quaternary-N (NQ, ~5%), and pyridinic-N-oxide (NX, 4%) (Relevant B.E.s are reported in the caption to Fig. 2.38 [53-56]). All these nitrogen forms undergo extensive redistribution upon heating to T = 900 °C, with N6 that decreases by ~25%, N5 by ~75%, such variations being counteracted by an extraordinary, tenfold increase of NQ and doubling of NX. These readjustments are in accordance with literature data [56] by which N5 and N6 are thermally unstable with respect to NQ. This latter NQ represents a class of compounds in which substitutional nitrogen in graphene layers is theoretically advocated [57-58] as active for ORR on metal-free catalysts.

However, results in Tab. 2.21 show that adding metals (Fe, Cu) to glucose/histidine precursors surprisingly does not cause a decrease in N5 and N6 signals with the increasing heating temperature, which would be expected from all the above literature data. This behavior may be attributed to the formation of metal complexes from N5 and N6 groups, which indirectly corresponds to their thermal stabilization. In support of this hypothesis, it can be mentioned that in a recent paper [59] the signal at 399.3 eV, which is consistent with the present N5 and N6 species, was attributed to iron-associated pyridinic nitrogen species. This evidence can be considered as an indirect proof of the presence of metals onto the carbon surface, even though they are not directly determined by XPS.

Electrochemical results

The synthesized materials were characterized by Rotating Disk Electrode (RDE) to obtain kinetic parameters for Oxygen Reduction Reaction (ORR).

Electrochemical results are collectively reported in Fig. 2.39 to permit comparison of the many materials obtained with variable relative Fe/Cu weight amounts and a constant, equimolar Glu/Hist ratio. Results only concern T = 900 °C given that weak or no activity was observed for T = 600 °C.

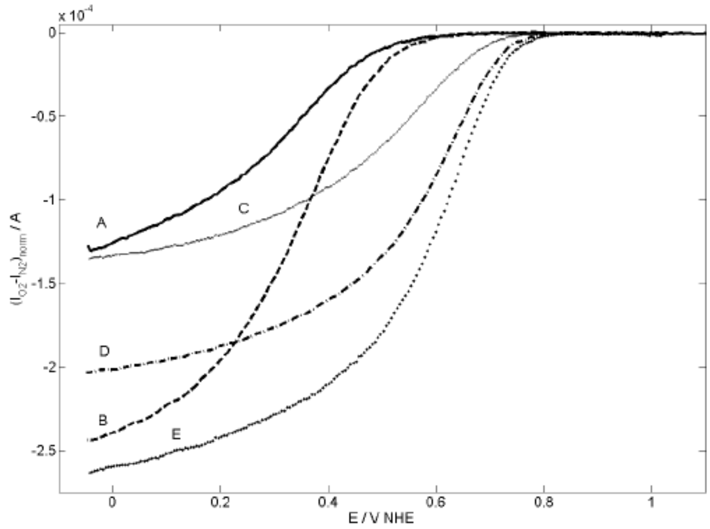

Fig. 2.39. CVs in O_2-saturated. (A) GluHist; (B) GluHistFe0; (C) Glu- HistFe25; (D) GluHistFe75; (E) GluHistFe100 (0.1 M $HClO_4$, T = 25 °C; scan rate 5 mV s^{-1}; rotation rate 700 rpm).

All curves are net oxygen reduction currents, corrections for background residual currents and real electrode surface area normalisation have been applied. The electrode surface area was measured by charge values obtained by integration of N_2 curves and the many investigated materials have been referred to Glu (T = 900°C) that was assumed as an internal, arbitrary reference.

Metal addition affects both incipient oxygen reduction potentials and currents. Notably enough, currents at first sharply increase by addition of Cu only (curve B) to the metal-free reference (curve A) and approach a limiting current behaviour at most negative potentials. Substituting a fractional Fe amount (25%) for Cu (curve C) causes the incipient oxygen reduction potential to shift anodic by ~0.2 V at the expense, however, of a decrease in current that becomes comparable to those of the Glu/Hist blank. Thereafter, any increase in fractional Fe amount is accompanied by gradually increasing currents, better approaching a diffusion mass transport behaviour, with some, though limited, further increase in incipient reduction potentials. Fig. 2.40a and b is an overview outlining the observed metal dependence of oxygen reduction currents and incipient reduction potentials (at x = 700 rpm, constant) in comparison with similar values recorded on a commercial Pt catalyst (EC-20).

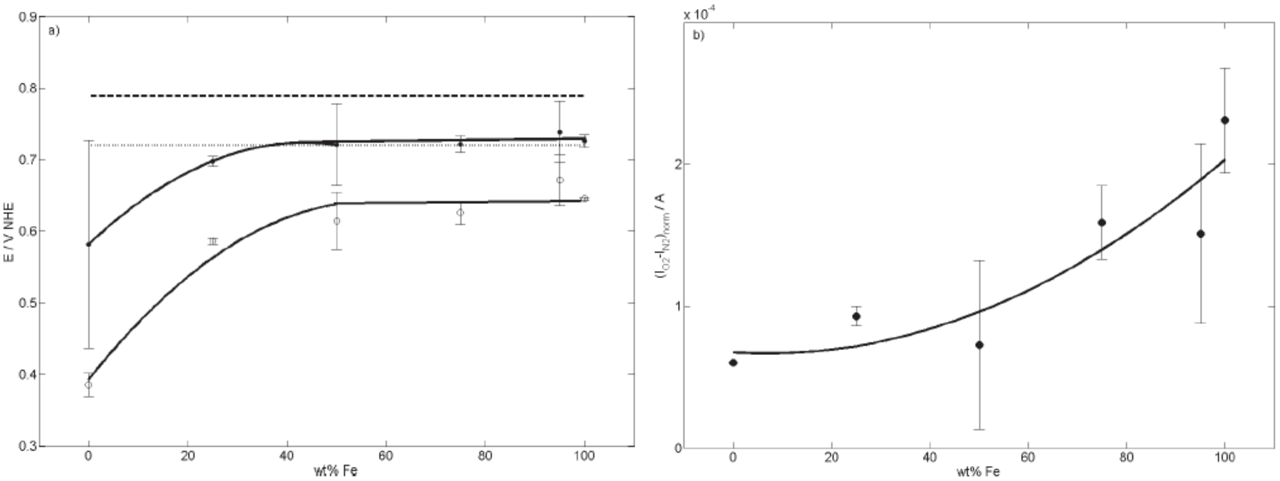

Fig. 2.40 (a) Incipient oxygen reduction potentials at different Fe wt%: ● and - - - (heavy dashes) potentials at the intersection points in Fig. 2.40; ○ and insert (light dashes) peak potentials of cathodic maxima at x = 0 rpm. Dashes are for EC-20 Pt catalyst, open and closed points are for home-made carbons. (b) Currents at E = +0.420 V NHE at different wt% Fe. Lines are a guide to the eye. Error bars represent standard deviation of experimental data. (0.1 M $HClO_4$; scan rate 5 mV s^{-1}; rotation rate 700 rpm; T = 25 °C.)

In Figure 2.40a, two series of incipient potential data are used, a first set of values being rather qualitatively based on ‘kink’ potentials at the crossover point between a first, generally flat and a second rising part of each I/E curve; the second set relying instead more quantitatively on the peak potential of a characteristic current maximum recorded at x = 0 rpm [60] (such results are not reported for brevity). In Figure 2.40a incipient potentials increase with increasing fractional Fe amount and reach well defined, limiting high values for Fe/Cu greater than ~50 wt%, lower than the corresponding Pt values by ~40–50 mV. A similar increasing trend occurs for currents (Figure 2.40b) without, however, any plateau and a maximum value at 100 wt% Fe.

Conclusions

On the one side, ORR behaviour improves with increasing Fe/Cu ratio, reaching however a maximum in the presence of Fe only, in the absence of a second metal (Cu), thus making uncertain that both metals are essential to catalytic ORR activity. Given the above XPS results, in both instances the question arises if Fe metal, possibly buried in the carbon matrix and/or complexed with nitrogen groups, is accessible, and to what extent, to the outside solution in order to form catalytically effective centres. Problems also arise concerning electrode durability given the limited amount of metal present as such or in ionic form.

2.6 Conclusions

1. Amino compound, carbon support and metal ion must be contemporarily present during pyrolysis, Fig. 2.9a and Fig. 2.10.
2. An effective and promising synthesis is the Flooding Synthesis, Fig. 2.13, based on the idea of completely wetting a precursor carbon surface and porosity system by reactive amine compounds (DETA) in which the metal ion is dissolved. Best catalyst is obtained by pyrolysis at 900 °C in flowing Ar.
3. Oxygen containing surface groups in the carbon precursor are useful to shift positive the onset ORR potential and to increase ORR currents that also show a steeper potential dependence and better defined limiting current, Fig. 2.20.
4. MEA experiments confirm the results obtained by RDE technique.
5. Nafion is not an inert binder. When it is adopted as electrode binder into the catalyst slurry, ORR promotion are evidenced at N/C=0.75. At this value experimental well defined limiting current is obtained and the internal diffusion current is at a minimum. This trend is different for Pt/C catalysts.

References

[1] L. Zhang, J. Zhang, D.P.Wilkson, H.Wang, J. Power Sources 156 (2006), 171

[2] F. Jaouen, J. Herranz, M. Lefèvre, J.P. Dodelet, U. I. Kramm, I. Herrmann, P. Bogdanoff, J. Maruyama, T. Nagaoka, A. Garsuch, J. R. Dahn, T. Olson, S. Pylypenko, P. Atanassov, E. A. Ustinov, App. Mat. And Interfaces, 1 (2009), 1623.

[3] Jasinski, R., Nature 201 (1964), 1212.

[4] Bagotzky, V. S.; Tarasevich, M. R.; Radyushkina, K. A.; Levina, O. E.; Andrusyova, S. I. J. Power Sources, 2 (1977), 233.

[5] Scherson, D.; Tanaka, A.; Gupta, S. L.; Tryk, D.; Fierro, C.; Holze, R.; Yeager, E. B. Electrochim. Acta, 31, (1986), 1247.

[6] Franke, R.; Ohms, D.; Wiesener, K. J. Electroanal. Chem., 260 (1989), 63

[7] Wiesener, K.; Ohms, D.; Neumann, V.; Franke, R. Mater. Chem. Phys., 22, (1989), 457

[8] Gupta, S. L.; Tryk, D.; Bae, I.; Aldred, W.; Yeager, E. B. J. Appl. Electrochem., 19 (1989), 19

[9] Coˆte´, R.; Lalande, G.; Guay, D.; Dodelet, J. P.; Denes, G. J. Electrochem. Soc.,145 (1998), 2411.

[10] M. Longhi, V. Bertacche, C. L. Bianchi, L. Formaro, Chem. Mater., 18 (2006), 4130.

[11] A. Proctor, P. M. A. Sherwood, Carbon, 21 (1983), 53.

[12] K. Kinoshita, J. S. A. Bett, Carbon, 11 (1973),403.

[13] M. Lefèvre, E. Proietti, F. Jaouen, J.-P. Dodelet, *Science*, 324 (2009), 71.

[14] M. Yuasa, A. Yamaguchi, H. Itsuki, K. Tanaka, M. Yamamoto, K. Oyaizu, *Chem. Mater.*, 17(2005), 4278.

[15] N. P. Subramanian, S. P. Kumaraguru, H. Colon-Mercado, H. Kim, B. N. Popov, T. Black, D. A. Chen, *J. Power Sources*, 157 (2006), 56.

[16] E. B. Easton, A. Bonakdarpour, R. Yang, D. A. Stevens, J. R. Dahn, *J. Electrochem. Soc.*, 155 (2008), B547.

[17] J. Maruyama, I. Abe, *Chem. Commun*., (2007), 2879.

[18] T. E. Wood, Z. Tan, A. K. Schmoeckel, D. O'Neill, R. Atanasoski, *J. Power Sources*, 178 (2008), 510.

[19] A. Garsuch, K. MacIntyre, X. Michaud, D. A. Stevens, J. R. Dahn, *J. Electrochem. Soc.*, 155 (2008), B953.

[20] T. Schilling, M. Bron, *Electrochim. Acta*, 53 (2008), 5379.

[21] A. H. C. Sirk, S. A. Campbell, V. I. Birss, *J. Electrochem. Soc.*, 155 (2008), B592.

[22] J. Maruyama, N. Fukui, M. Kawaguchi, I. Abe, *J. Power Sources*, 182 (2008), 489.

[23] V. Nallathambi, J.-W. Lee, S. P. Kumaraguru, G. Wu, B. N. Popov, *J. Power Sources*, 183 (2008), 34.

[24] O. Ikeda, H. Fukuda, H. Tamura, *J. Chem. Soc.*, *Farad. Trans.*, 82 (1986), 1561.

[25] R. Holze, I. Vogel, W. Vielstich, *J. Electroanal. Chem.*, 210 (1986), 277.

[26] S. Dong, R. Jiang, Ber. Bunsenges. *Phys. Chem*., 91 (1987), 479.

[27] T. Sawaguchi, T. Itabashi, T. Matsue, I. Uchida, *J. Electroanal. Chem.*, 279 (1990), 219.

[28] A. Widelöv, R. Lasson, *Electrochim. Acta*, 37 (1992), 187.

[29] A. Widelöv, *Electrochim. Acta*, 38 (1993), 2493.

[30] B. Bittins-Cattaneo, S. Wasmus, B. Lopez-Mishima, V. Vielstiech, *J. Appl. Electrochem*., 23 (1993), 625.

[31] G. Faubert, G. Lalande, R. Côté, D. Guay, J. P. Dodelet, L. T. Weng, P. Bertrand, G. Dénès, *Electrochim. Acta*, 41 (1996), 1689.

[32] G. Faubert, R. Côté, D. Guay, J. P. Dodelet, G. Dénès, P. Bertrand, *Electrochim. Acta*, 43 (1998), 341.

[33] A. L. Bouwkamp-Wijnoltz, W. Visscher, J. A. R. van Veen, *Electrochim. Acta*, 43 (1998), 3141.

[34] S. L. Gojkovic, S. Gupta, R. F. Savinell, *J. Electroanal. Chem.*, 462 (1999), 462.
[35] R. Jiang, D. Chu, *J. Electrochem. Soc.*, 147 (2000), 4605.
[36] M. Lefèvre, J. P. Dodelet, P. Bertrand, *J. Phys. Chem. B*, 104 (2000), 11238.
[37] M. Lefèvre, J. P. Dodelet, P. Bertrand, *J. Phys. Chem. B*, 106 (2002), 8705.
[38] A. L. Bouwkamp-Wijnoltz, W. Visscher, J. A. R. van Veen, E. Boellaard, A. M. van der Kraan, S. C. Tang, *J. Phys. Chem. B*, 106 (2002), 12993.
[39] M. Lefèvre, J. P. Dodelet, *Electrochim. Acta*, 48 (2003), 2749.
[40] H. Schulenburg, S. Stankov, V. Schünemann, J. Radnik, I. Dorbandt, S. Fiechter, P. Bogdanoff, H. Tributsch, *J. Phys. Chem. B*, 107 (2003), 9034.
[41] J. A. R. van Veen, H. A. Colijn, J. F. van Baar, *Electrochim. Acta*, 33 (1988), 801.
[42] G. Lalande, G. Faubert, R. Côté, D. Guay, J. P. Dodelet, L. T. Weng, P. Bertrand, *J. Power Sources*, 61 (1996), 227.
[43] M. Bron, J. Radnik, M. Fieber-Erdmann, P. Bogdanoff, S. Fiechter, *J. Electroanal. Chem.*, 535 (2002), 113.
[44] K. Sawai, N. Suzuki, *J. Electrochem. Soc.*, 151 (2004), A2132.
[45] R. Bashyam, P. Zelenay, *Nature*, 443 (2006), 63.
[46] K. Lee, L. Zhang, H. Lui, R. Hui, Z. Shi, J. Zhang, *Electrochim. Acta*, 54 (2009), 4704.
[47] Y. Ma, P. B. Balbuena, *Chem. Phys. Lett.*, 440 (2007), 130.
[48] E. Antolini, *Appl. Catal. B*, 88 (2009), 1.
[49] J. Herranz, M. Lefèvre, J.-P. Dodelet, *J. Electrochem. Soc.*,156 (2009), B593.
[50] C. W. B. Bezerra, L. Zhang, K. Lee, H. Liu, A. L. B. Marques, E. P. Marques, H. Wang, J. Zhang, *Electrochim. Acta*, 53 (2008), 4937.
[51] P. Wang, Z. Wang, L. Jia, Z. Xiao, *Phys. Chem. Chem. Phys.*, 11 (2009), 2730.
[52] R. Fu, N. Yoshizawa, M. S. Dresselhaus, G. Dresselhaus, J. H. Satcher Jr., T. F. Baumann, *Langmuir*, 18 (2002), 10100.
[53] D. Hulicova-Jurcakova, M. Seredych, G. Q. Lu, T. J. Bandosz, *Adv. Funct. Mater.*, 19 (2009), 438.
[54] S. Biniak, G. Szymanski, J. Siedlewski, A. Swiatkowski, *Carbon*, 35 (1997), 1799.
[55] D. Long, J. Zhang, J. Yang, Z. Hu, G. Cheng, X. Liu, R. Zhang, L. Zhan, W. Qiao, L. Ling, *Carbon*, 46 (2008), 1253.
[56] J. R. Pels, F. Kapteijn, J. A. Moulijn, Q. Zhu, K. M. Thomas, *Carbon*, 33 (1995), 1641.
[57] R. A. Sidik, A. B. Anderson, N. P. Subramanian, S. P. Kamaraguru, B. N. Popov, *J. Phys. Chem. B*, 110 (2006), 1787.
[58] N. P. Subramanian, X. Li, V. Nallathambi, S. P. Kumaraguru, H. Colon-Mercado, G. Wu, J.-W. Lee, B. N. Popov, *J. Power Sources*, 188 (2009), 38.
[59] R. Kothandaraman, V. Nallathambi, K. Artyushkova, S. Calabrese Barton, *Appl. Catal. B*, 92 (2009), 209.
[60] F. Jaouen, S. Marcotte, J.-P. Dodelet, G. Lindbergh, *J. Phys. Chem. B*, 107 (2003), 1376.

Conclusions

The aim of this thesis was to study and to develop nitrogen doped carbon electrocatalysts for oxygen reduction reaction (ORR). These electrocatalysts are a promising alternative to Pt/C at the cathode side of a Polymer Electrolyte Fuel Cell (PEMFC) where ORR is kinetically slow.

The investigation of commercial Pt/based catalyst was performed by means of the Thin film Rotating Disk Electrode (TFRDE) technique. This is a fast screening tool to determine the electrocatalytic activity and kinetic parameters of supported catalysts.

This investigation outlined some criteria that are useful to obtain reliable RDE results on supported Pt/C, and other electrode material:

1. Pt catalyst amounts must be reproducibly controlled. This is achieved by means of the overall Pt-H adsorption/desorption charge which is insensitive of electrode layer thickness. On Pt-free materials, where H-adsorption does not occur, the deposited amount can be controlled by the charge values measured by integration of CV patterns.
2. ORR limiting current densities must conform to the Levich model, where the geometrical electrode area is adopted as current normalization factor.
3. Determination of kinetic parameters is achievable by extrapolation from the Koutecky-Levich equation of the kinetic parameters. By plotting this data in Tafel form it is possible to determine if additional mass transport occurs within the electrode layer.
4. Thickness of supported Pt/C catalyst must be as thin as feasible in order that hydrodynamic RDE conditions are not perturbed and provided that on an almost complete coverage of the glassy carbon tip is achieved,.

Nafion was used to attach catalyst powders onto the working electrode tip.

When used as overlayer of the RDE tip, Nafion acts as an additional mass transport and diffusion hindrance. These screening effects cause a limiting current decrease with increasing overlayer thickness.

When Nafion is used as a binder, dispersing it within the catalyst layer, ORR reaction promotion can be instead evidenced at comparative low Nafion/Catalyst (N/C) ratio. At higher N/C inhibition effects prevails with respect to the above overlayer results. These results have been obtained by determination of the diffusion limited current within the catalyst layer, by a procedure based on the Koutecky-Levich equation.

Nafion is also active in modifying the kinetic charge transfer behavior, that is evident in Tafel plots after correction for external and internal diffusion processes.

Synthesis of nitrogen doped carbon catalysts was performed by modification of high surface area commercial carbons with amines and metal ions (Fe^{2+}, Co^{2+}) and by pyrolysis of templated glucose/histidine precursors loaded with Fe^{2+} and Cu^{2+} in variable ratios. All syntheses were followed by pyrolysis which is, in the first case, necessary to promote the catalytic activity and, in the latter, to carbonize precursors and enhance catalytic activity.

Stoichiometric carbon amination, metal loading and pyrolysis result in poor catalytic activity that is not improved by variation of the used amine compound, metal ion and carbon support. An effective and promising carbon modification is based on the idea of completely flooding the surface and the internal porosity system of a precursor carbon, by reactive amine compounds (DETA) in which the metal ion is dissolved.

By means of RDE and MEA results, textural and chemical characterization of those materials the following conclusion were obtained.

The contemporary presence of a nitrogen containing precursor (amines), metal ion (Fe or Co) and carbon support during pyrolysis is mandatory to improve the catalytic activity.

Oxygen containing surface groups at carbon surface, from Boehm titrations and EDX data, are useful to improve the catalytic activity, both shifting positive the onset ORR potential and increasing ORR currents.

The effect of Nafion as binder within the catalyst layer was investigated by varying the N/C ratio.

Internal diffusion currents depend on N/C ratio, with a different trend than that of Pt/based materials. Currents increase with increasing N/C up to a maximum at N/C=0.75 and then decrease at higher N/Cs.

The internal diffusion dependence on potential is different for Pt/C and Pt-free catalysts. This may be related to variation in the Nafion ionomer interaction with carbon substrates and with ORR catalytic active centres. In Pt/C catalysts these centres are in the form Pt nanoparticles while in Pt-free carbon they are presumably distributed throughout the carbon surface with presumably macrocycle pyridinic structures.

Effective catalysts were also obtained by carbonization of a hard templated glucose/histidine precursor loaded with different Fe/Cu ratio. Metal loading effects were investigated by XPS obtaining an indirect proof of the metal presence onto the carbon surface.

Electrochemical parameters were obtained by means of RDE technique: onset ORR potentials increase with increasing Fe amount, with a maximum value that is only ≈40-50 mV lower than the corresponding Pt value.

Experimental section

Synthesis and carbons pre-treatment

Activated carbon pre-treatment (washing procedure):

Acid treatment: Acid treatment consist on stirring a Darco KB-G (DG)carbon suspension in HCl 2 M solution for 70 hours, then soxhlet extraction of impurities with HCl 2M, then filter and washing with m-Q waters until pH=7 and conductivity values of water of 50 μS are reach. On water used a qualitative analysis shows that iron and phosphates are efficiently removed by this treatment.

At the end carbon is dry under nitrogen flow at 100°C for 24 h and next at 110°C for 24 hours.

Carbon after this treatment is labelled DG-A

Basic treatment: Basic treatment consist on stirring a DG suspension in NH_3 0.5 M for 40 hours, and then soxhlet extraction of impurities with ammonia solution and subsequently with water until pH=7 and conductivity values of 85 μS are reach. Carbon after this treatment is labelled DG-B

Carbon black pre-treatment:

Carbon blacks (FW 200, XPB 334 and XPB 390) were used as received.

Stoichiometric amination of activated carbon DG and carbon black FW 200

Binding procedure of o-phenylenediamine, diethylenetriamine and 1,6-hexamethylenediamine onto activated carbon surface:

In a typical run an acid treatment was used to wash carbon and then this material (~8 g) was added to a 150 ml of amine ($3.3\ 10^{-2}$ mol $-NH_2$/g carbon) solution in diethylenglycol dimethylether.

Suspension was heated at 140°C for 40 hours. Reacted samples were filtered and redispersed several times in water. Drying was performed in flowing N_2 for 24 h at 110°C. After this treatment carbon is labelled DGA-*amine compound abbreviation*.

In the stoichiometric activation synthesis the amine amount was calculated in excess than to the sum of carboxyl and lactone groups at the carbon surface quantify with Boehm titration method. Using this synthesis the amino groups react with the carboxyls and lactone groups at the carbon surface forming an amide compound. Using a large excess of a terminal diamine compound only one of these groups reacts with the carboxyls, leaving the other one free to react further. In this case the free amino group was used to coordinate a cobalt or iron ion introduced by a incipient wetting method. The so modified carbon black was pyrolyzed to obtain the catalyst. This kind of synthesis take advantage of the carboxyls group at carbon surface so the amount of amino compound bonded to the carbon surface is limited by this factor.

***o*-phenylenediamine polymerization at the carbon surface.**

o-phenylenediamine monomer, introduced with the previous synthesis is used as starting point for polymerization in acid conditions.

In a typical synthesis aminated carbon (2.5 g) was suspended in 240 ml of glacial acid acetic. Using syringe pump 60 ml of 0.15 M o-phenylene in glacial acetic acid was added at 2.2 ml/min. As polymer catalyst $(NH_4)_2S_2O_8$ (30 ml, 0.901 M) was used. After stirring for 10 minutes the suspension was refluxed at 110°C for 72 h. Carbon was filtered and washed with acetic acid to remove un-reacted amine and then water until pH=7. Drying was performed in flowing N_2 for 24 h at 110°C.

After polymerization the carbon is called DGA P *o*-phen.

Pyrolysis of aminated carbons

Pyrolysis in the stoichiometric amination is performed with a 3 steps procedure in a vertical oven:

1. Degasing in N_2 gas flow at 100 ml min^{-1} for 25 minutes,
2. Ramp at 6°c min^{-1} until 700 °C or 900 °C depending on the final temperature N_2 gas flow,
3. Step at 700-900°C for 3 hours N_2 gas flow,
4. Rapid quenching at room temperature N_2 gas flow.

Metal loading

Carbons aminated with the stoichiometric synthesis were loaded with $Fe(COOH)_2$ and $Co(COOH)_2$ to introduce 2 wt% of the metal ion. About 0.800g of aminated carbon were added with 2.0 ml of water to obtain a semi-solid paste (*incipient wetting method*). To this, 1.87 ml of a solution ≈0.14 M of the metal salt was added drop wise to obtain an homogeneous paste. Then, the suspension was dried at 100 °C for 3 hours, added with 2 ml water and dried 24 hours at 100 °C.

Flooding pore synthesis

In a typical run carbon black (Degussa FW200, XPB 334, XPB 390) (≈5 g) was suspended in liquid diethylenetriamine, (DETA 27.5 ml), containing cobalt acetate (5 wt% Co(II) with respect to carbon, ≈0.75g) and added with of 1-propanol (16 g) to decrease the suspension viscosity. The DETA/carbon ratio was calculated to overfill the carbon pore volume from BET (N_2) determinations. The resulting thick slurry was mechanically stirred for 72 h at room temperature and then pyrolyzed in a alumina container placed in a quartz tube still in the presence of DETA excess, in a horizontal oven:

1. Degasing in Ar gas flow at 100 ml min^{-1} for 25 minutes,
2. Ramp at 6 °C min^{-1} until 700 °C or 900 °C depending on the final temperature Ar gas flow (100 ml min^{-1}) or H_2-N_2 1:9 mixture (100 ml min^{-1}),
3. Step at 700-900 °C for 3 hours Ar (100 ml min^{-1}) or H_2-N_2 1:9 mixture (100 ml min^{-1}) gas flow,
4. Quenching in the oven under Ar (100 ml min^{-1}) or H_2-N_2 1:9 mixture (100 ml min^{-1}) gas flow.

Glucose/Histidine synthesis

A glucose (Glu in the following) solution in water (1.68 mol dm^{-3}) was added with histidine (Hist) in variable molar ratios: Glu/Hist = 1:1 is indicated as GluHist in the following; Glu/Hist = 2:1 as GluHist0.5; Glu/Hist = 4:1 as GluHist0.25; Glu/Hist = 10:1 as GluHist0.1. Adding equimolar glacial acetic was found necessary to dissolve histidine. Ten millilitres of this solution were stirred with 4.3 g of silica for 5 min to form a gel, and stirred again 5 min after 15 min standing. The gel was loaded in a quartz reactor, degassed with N_2 (100 cm^3 min^{-1}) for about 5 min and inserted in a preheated vertical oven at T = 600 °C in order to carbonise as fast as possible the precursors, preserving the ordered room temperature gel structure in the final products. Heating was continued for 1 h under continuous N_2 purging (100 cm^3 min^{-1}). Then the tube was rapidly quenched in air. Silica was removed in 3 M boiling NaOH followed by repeated carbon washing/filtering (MilliQ water, 0.45 μm Durapore filters) until water conductivity became lower than 4 μS. Products were dried in nitrogen (100 °C, 24 h) and finally ground in an agate mortar. Metal containing catalysts were prepared by the same procedure but for the addition of acetate metal salts (Fe and Cu ions at 1 wt% total with respect to glucose + histidine, at variable ratios between them). The ratio of iron and copper salts was varied in a range from 0 to 100% iron: GluHistFe0: 0% Fe/100% Cu; Glu-HistFe25: 25% Fe/75% Cu; GluHistFe50: 50% Fe/50% Cu; GluHistFe75: 75% Fe/25% Cu; GluHistFe95: 95% Fe/5% Cu; GluHistFe100:100% Fe/0% Cu.

All materials were heat-activated in a second step at T = 900 °C under constant N_2 flow (100 cm^3 min^{-1}) in the following conditions: 30 min room temperature purging, ramping at 6 °C min^{-1} and 3 h standing at T = 900 °C, fast quenching to room temperature.

MEA (Membrane Electrolyte Assembly)

In a first step, the Membrane Electrode Assemblies procedure was optimized for the used catalyst. Catalysts were anchored at a polymer membrane by spraying catalyst inks onto the membrane. Optimization of the ink composition, finding suitable water and Nafion amounts with respect to unit catalyst amounts (both for anode and cathode sides) are relevant to catalyst activity evaluation. Also the cell assembly is a most important parameter to be checked, with the gasket thickness necessarily comparable (±30%) to the MEA thickness between the gas diffusion layers (GDL). Moreover, operating parameters of the fuel cell (Cell and gas line temperature, anode and cathode humidification) had to be optimized to have a better water management in the operating cell.

A single PEM fuel cell with 25 cm^2 electrode area ($5 \cdot 5$ cm^2) surface was assembled using the spraying methods.

Nafion 112 membrane was boiled in 3% H_2O_2 to remove organic contaminants followed by boiling in water. The membrane was then boiled in 0.5 M H_2SO_4 to replace the Na^+ ions with H^+. This treatment was followed by boiling in water.

MEA preparation: wet membrane was fixed in aluminium framework and dried at 120 °C till constant weight was reached. The catalyst ink was sprayed onto the membrane using an air brush and the catalyst loading was determined by weighting the MEA. The membrane was then put in oven at 135 °C for 30 minutes and then hot pressed at 130 °C, 140 bar for 10 minutes.

The anode was prepared with a commercial Heraeus E-TEK Pt/C 40 wt.%. The ink was prepared with 1.2 g Heraeus 40% Pt/C in 30.0 g H_2O and 8.0 g Nafion 1,100 g mol^{-1} EW, 15 wt.% alcohol solution put under mechanical stirring for 48 hours in a close vessel. About 0.06 g catalyst spray onto the membrane, that is about 3 mgC cm^{-2}.

At the cathode the Pt-free catalyst was used. The ink was prepared with 0.3 g catalyst in 3.0 g H_2O and 2.0 g Nafion 1100 EW 15% alcohol solution, under stirring 48 hours in a close vessel. About 0.10 g was sprayed onto the membrane.

The MEA was assembled in a single graphite test cell with a gas diffusion layer (from SGL Carbon, Sigracet 10 BB, 5% hydrophobized single side coated amorphous layer).

Fuel cell working parameters: the fuel cell temperature was controlled in different points of the apparatus:

- Into the cell (60 °C),
- Into the water tank for gas humidification, (T=50°C),
- Into the gas line (A) from the water tank to other line, (T=70°C),
- Into other line to the cell, (T=70 °C),

The last three points are for anode and cathode side.

Current-voltage curves were determined galvanostatically at 70°C with humidified hydrogen flow at the anode and humidify oxygen at the cathode. Both gases were supplied to the cell at ambient pressure.

Rotating Disk Electrode (RDE)

Pt/C, EC-20 and Pt-free activated carbons

Electrode and catalyst layer preparation

Electrochemical characterization was performed by the thin film rotating disk electrode (TFRDE) immobilizing small catalyst amounts onto the glassy carbon tip (geometric surface area: A = 0.07 cm^2) of a rotating disk electrode (EDI 101, radiometer). Before use, the tip was gently cleaned with soft sandpaper, polished by diamond powder (Aldrich) alumina powder (0.5 μm then 0.03 μm) and finally degreased with ethanol. Catalyst aliquots (8 mg) were dispersed in water added with Nafion EW 1000, solution in water and alcohols 5 wt% (1.5 mL water, 4 μl Nafion) and sonicated for 30 min; 7 μl of this mixture were pipetted onto the electrode tip and dried in a bottom-up position above a tungsten lamp.

For experiments at increasing catalyst layer thickness the suspension concentration was increased keeping constant used volumes.

For experiment in which Nafion is deposited as overlayer the following procedure was adopted: the catalyst suspension (8 mg carbon catalyst) was dispersed in water (1.5 ml) and 7 μl of this suspension pipetted onto the glassy carbon tip. The electrode was dried in a bottom-up position above a tungsten lamp and then 7 μl of a Nafion suspension (5 μl of a commercial Nafion, 1500 solution 5 wt% in alcohol, diluited in 0.67 ml of water) was pipetted above the catalyst layer and dried bottom-up above a tungsten lamp. Prior to use the electrode was washed with Milli-Q water. To increase Nafion overlayer thickness Nafion suspensions were deposited above already deposited layers.

For Pt/free characterization of material based on activated carbon, catalyst aliquots (8 mg) were dispersed in water added with Nafion EW 1000, solution in water and alcohols 5 wt% (1.5 mL water, 4 μL Nafion) and sonicated for 30 min; 7 μL of this mixture were pipetted onto the electrode tip and dried in a bottom-up position above a tungsten lamp.

Electrochemical measurements

A two-compartment cell with a graphite counter electrode (Amel 201/S-016) and a AgCl/Ag external reference electrode (Amel) in 3 M NaCl was used. The reference was connected to the cell by a salt bridge filled with the working electrolyte (0.1 M $HClO_4$). Before each experimental run, all glasswares were washed by concentrated H_2SO_4 and rinsed in MilliQ water. The counter electrode was cleaned with filter paper. The potentiostat was AMEL mod. 7050.

Before measurements the electrode was conditioned cycling 3 cycle in N_2 saturated solution (5 mV s^{-1}, ω = 1,600 rpm) in the potential range E = –0.275–+0.900 V. ORR results were collected in the same conditions at different rotation rate. After measurements in O_2, CVs were again recorded in N_2 to obtain background faradaic currents for O_2 reduction data correction.

Glucose/Histidine

Electrode and catalyst layer preparation

Electrochemical characterisation was performed by the thin film rotating disk electrode (TFRDE) method immobilising small catalyst amounts onto the glassy carbon tip (geometric surface area: A = 0.07 cm^2) of a rotating disk electrode (EDI 101, radiometer). Before use, the tip was gently cleaned with soft sandpaper, polished by diamond powder (Aldrich) alumina powder (0.5 μm then 0.03 μm) and finally degreased with ethanol. Catalyst aliquots (8 mg) were dispersed in water added with Nafion EW 1000, solution in water and alcohols 5 wt% (1.5 mL water, 4 μL Nafion) and sonicated for 30 min; 7 μL of this mixture were pipetted onto the electrode tip and dried in a bottom-up position above a tungsten lamp.

Electrochemical measurements

A two-compartment cell with a graphite counter electrode (Amel 201/S-016) and a AgCl/Ag external reference electrode (Amel) in 3 M NaCl was used. The reference was connected to the cell by a salt bridge filled with the working electrolyte (0.1 M $HClO_4$). Before each experimental run, all glasswares were washed by concentrated H_2SO_4 and rinsed in MilliQ water. The counter electrode was cleaned with filter paper. The potentiostat was AMEL mod. 7050.

Glucose/Histidine compounds: measurements were performed by an accurately reproducible procedure. Before CV recording, the electrode was conditioned cycling 45 min in N_2 in the potential range E = –0.275–+0.800 V, followed by 100 min cycling in O_2 saturated solution (5 mV s^{-1}, ω = 1,600 rpm). Then O_2 reduction results were recorded in the same conditions at different electrode rotation rates. To verify electrode stability and internal reproducibility, several CVs at x = 1,600 rpm were recorded in each run. After measurements in O_2, CVs were again recorded in N_2 to obtain background faradaic currents for O_2 reduction data correction. Background charge values were also obtained by integration of N_2 curves and used as a measure of real electrode surface area, normalising the many investigated materials with respect to Glu (T = 900 °C) that was assumed as an internal, arbitrary reference.

Effect of Nafion composition Pt/C 40 wt%. N/C

Electrode and catalyst layer preparation: before use both Pt/C and Pt-free/C catalyst were hand-grounded in a mortar. Inks with different N/C ratios were obtained by varying the H_2O+Nafion EW 1100 15 wt% solution in water and alcohol total amount with respect to solids in order to keep constant the catalyst amount per unit slurry volume. For instance N/C=1.0 was obtained suspending 0.1 g catalyst in 1.5 g H_2O added with 0.67 g of the Nafion suspension. After mixing components, inks were mechanically stirred 48 hours. In this way the catalyst amount was kept constant permitting to deposit catalyst layers with (calculated) thickness not exceeding 10 μm onto the glassy carbon tip. Ink volumes were typically 10 μl.

Electrochemical measurements: all reactants (Aldrich) were of analytical grade. A commercial platinum catalyst (Heraeus 40 wt % Pt) and a commercial carbon black (Degussa XPB390, a kind gift of the producer) were used and bound to the electrode by means of a Nafion suspension (Aldrich, 1100, 15 wt % in alcohol). A three compartments cell was used with a platinum wire counter electrode and a standard calomel reference connected to the cell by a Luggin salt bridge filled with the cell electrolyte.

Before measurements the cell was washed with hydrochloric acid, MilliQ water, hydrogen peroxide (30 %) and then rinsed several times with MilliQ water. The cell was then filled with 0.1 M $HClO_4$. A Radiometer rotating disk electrode (Model ED 101) with a glassy carbon tip (geometric surface area: A = 0.196 cm^2) and a home-made potentiostat were used. Before ink deposition the electrode tip was polished with 0.05 μm alumina followed by several washings with MilliQ water. Electrochemical characterization was performed using the “thin film rotating disk electrode” geometry immobilizing a small volume of catalyst ink onto the electrode tip.

Before measurements, electrodes were initially conditioned in O_2-saturated solutions by continuously cycling at 1600 rpm, 5 mV/s in the potential range +0.910/-0.300 V (SCE) till completely superimposable I/E curves were obtained. Measurements were performed in the same conditions at various rotation rates. Every three cycles rotation speed was changed to a random value in the range 100-1600 rpm that was kept constant for the next three cycles, the last one being stored for successive elaboration.

After measurements in O_2 the electrolyte was degassed with N_2 for 30 minutes. After obtaining superimposable I/E results, faradic currents were recorded for subtraction-correction from O_2 reduction data. As considered below I/E results for both Pt-based and Pt-free catalysts are normalized on the projected electrode surface area. As also relevant, results at 0 and 1600 rpm in N_2 saturated solutions were indistinguishable.

Boehm titrations

Boehm titrations were carried out according to standard procedures. Independent carbon samples (0.2 g) were placed in 25 mL of NaOH, Na_2CO_3, $NaHCO_3$, and HCl (all 0.05 N). Vials were sealed and equilibrated for 24 h by bottom-up rotation and filtered. To determine the amount of acid groups, aliquots (5 mL) from the basic solutions were added to excess 0.05 N HCl and back-titrated with NaOH. Similarly, basic groups were determined by direct NaOH titration of solutions from HCl equilibration. Titrations were performed in triplicate under flowing N_2 to exclude CO_2 contamination from the used reactants and the atmosphere. Results were calculated assuming that NaOH reacts with all acidic carbon groups (phenols, lactones, carboxyls), that Na_2CO_3 reacts with lactonic and carboxylic groups, to the exclusion of phenols, and finally, that $NaHCO_3$ only reacts with carboxyls.